
The Growth of the First Galaxies

Kenneth James Duncan



Thesis submitted to the University of Nottingham
for the degree of Doctor of Philosophy, March 2015

“My amusing/profound quotation”

– Author

Supervisor: Prof. Christopher J. Conselice

Examiners: Dr. Meghan Grey
Dr. Elizabeth Stanway

Abstract

Text of abstract.

Contents

List of Figures	iii
List of Tables	vii
My Thesis Title	
1 Introduction	2
1.1 The Early Universe	2
1.2 Studying distant galaxies	3
1.3 Estimating galaxy stellar masses	4
1.4 The CANDELS survey	6
1.5 Thesis Outline	8
2 The mass evolution of the first galaxies	9
2.1 Introduction	9
2.2 The Data	13
2.2.1 Imaging Data	13
2.2.2 Source photometry and deconfusion	14
2.3 Photometric Redshifts and Sample Selection	14
2.3.1 Selection Criteria	15
2.3.2 Monte Carlo Samples	18
2.4 Selection method comparison	21
2.5 Mass Fitting	32
2.5.1 Model SEDs	32
2.5.2 Nebular Emission	33
2.5.3 SED Fitting	34
2.5.4 Star Formation Rates	35
2.5.5 Image and Detection Simulations	36

2.6	Results	42
2.6.1	The $1/V_{\max}$ estimator	42
2.6.2	UV Luminosity functions	43
2.6.3	Observed mass-to-light ratios	45
2.6.4	Stellar mass functions at high-redshift	50
2.6.5	Stellar Mass Density	57
2.6.6	Star Formation Rates	58
2.7	Summary	64
2.8	Observed UV continuum slopes	66
3	Powering reionization	69
3.1	Introduction	69
3.2	Linking reionization with observations	72
3.2.1	The ionizing emissivity	72
3.2.2	Mechanisms for Lyman continuum escape	74
3.2.3	Observed UV Continuum Slopes	76
3.3	Modelling β , ξ_{ion} and κ_{ion}	80
3.3.1	Modelling assumptions: current constraints on stellar populations at $z > 3$	82
3.3.2	Observed UV slopes as a function of f_{esc} and dust extinction .	90
3.3.3	ξ_{ion} and κ_{ion} as a function of f_{esc} and dust extinction	93
3.3.4	Effect of different stellar population properties on ξ_{ion} and κ_{ion} vs β	94
3.4	Estimated galaxy emissivity during reionization	97
3.4.1	Observations	97
3.4.2	\dot{N}_{ion} for constant $f_{esc}\xi_{ion}$ and $f_{esc}\kappa_{ion}$	98
3.4.3	\dot{N}_{ion} for evolving $f_{esc}\xi_{ion}$ and $f_{esc}\kappa_{ion}$	102
3.5	Discussion and future prospects	106
3.6	Summary	109
Appendices		
A	Reionization Data Tables	113
B	Short appendix heading	116
Bibliography		117

List of Figures

1.1	Short caption	4
2.1	Short caption	16
2.2	Short caption	20
2.3	Short caption	25
2.4	Short caption	27
2.5	Short caption	29
2.6	Short caption	30
2.7	Short caption	31
2.8	Short caption	38
2.9	Short caption	40
2.10	Short caption	41
2.11	Short caption	42
2.12	Short caption	44
2.13	Short caption	47
2.14	Short caption	51
2.15	Short caption	54
2.16	Short caption	56
2.17	Short caption	57
2.18	Short caption	59
2.19	Short caption	62
2.20	Short caption	63
2.21	Short caption	66
2.22	Short caption	67
2.23	Short caption	68

3.1	Schematic cartoon illustrations of the Lyman continuum escape mechanisms outlined in Section 3.2. For both models, the stars represent a central galaxy surrounded by a HII ionization region, dust is distributed in an outer dust-screen. Left: An ionization bounded nebula with holes (sometimes referred to as the ‘picket fence model’) in which LyC escapes through holes in the ISM. Right: a density bounded nebula where LyC is able to escape due to the incomplete Strömgren sphere formed when the galaxy depletes its supply of neutral hydrogen.	75
3.2	Observed average values of the UV continuum slopes β as a function of rest-frame UV magnitude, M_{UV} , from Wilkins <i>et al.</i> (2011), Dunlop <i>et al.</i> (2011, 2013), Finkelstein <i>et al.</i> (2012b), Bouwens <i>et al.</i> (2014a), Duncan <i>et al.</i> (2014) and Rogers <i>et al.</i> (2014) at redshifts $z \sim 4, 5, 6$ and $7 - 9$. In the bottom panel, filled symbols show the average for $z \sim 7$ samples while the open symbols show the averages for $z \geq 8$ (see respective papers for sample details and redshift ranges).	77
3.3	Luminosity-weighted average β , $\langle \beta \rangle_{\rho_{UV}}$, as a function of redshift for the $M_{UV} - \beta$ observations shown in Fig. 3.2. The grey shaded region covers the range $-2.2 < \beta < -1.8$ and the blue long-dashed line shows our parametrisation of $\langle \beta \rangle_{\rho_{UV}}$ vs z based on the observations of Bouwens <i>et al.</i> (2014a) (blue circles) at $z \lesssim 7$	78
3.4	Power-law (blue continuous: Salmon <i>et al.</i> 2014, red dotted: Papovich <i>et al.</i> 2011) and exponential (green dashed: Papovich <i>et al.</i> 2011) fits to the median observed SFR-densities at $z > 4$ for 3 different star formation histories. For the power-law fits, the shaded red and blue regions correspond to the $1-\sigma$ errors on the slope of the power-law, α , quoted in the respective papers. The grey dot-dashed line shows the best-fit to the median star-formation rates across the the full cosmic history for the functional form outlined in Behroozi, Wechsler & Conroy (2013). All of the models assume an initial onset of star-formation at $z_f = 12$.	83
3.5	Left: UV continuum slope β as a function of total escape fraction, f_{esc} , and dust extinction, A_V , for the <i>ionization bounded nebula with holes</i> continuum escape model (Model A, Fig. 3.1 left) with stellar population properties as outlined in Section 3.3.1. The contours indicate lines of constant β around the observed average β , and the light grey arrow indicates how those contours move for a stellar population with solar metallicity. Middle and right: $\log_{10} f_{esc}\xi_{ion}$ and $\log_{10} f_{esc}\kappa_{ion}$ as a function of escape fraction and dust extinction respectively for the same continuum escape model. Solid contours represent lines of constant $f_{esc}\xi_{ion}$ and $f_{esc}\kappa_{ion}$ whilst the dashed contour shows where $\beta = -2$ is located for reference. The green labelled contour shows the assumed $f_{esc}\xi_{ion} = 24.5$ value of Robertson <i>et al.</i> (2013) and the equivalent in $f_{esc}\kappa_{ion}$ (see text for details). For the colour scales below the centre and right panels, the lower black tick labels correspond to the scale for the fiducial model ($Z = 0.2Z_\odot$) whilst the grey upper tick label indicate how $f_{esc}\xi_{ion}$ and $f_{esc}\kappa_{ion}$ change for stellar populations with solar metallicity.	91

- 3.6 Left: UV continuum slope β as a function of HII region escape fraction, f_{esc} , and dust extinction, A_V , for the *density bounded nebula* continuum escape model (Model B, Fig. 3.1 right) with stellar population properties as outlined in Section 3.3.1. The contours indicate lines of constant β around the observed average β , and the light grey arrow indicates how those contours move for a stellar population with solar metallicity. Centre and right: $\log_{10} f_{esc}\xi_{ion}$ and $\log_{10} f_{esc}\kappa_{ion}$ (where f_{esc} is the total dust attenuated escape fraction) as a function of escape fraction and dust extinction respectively for the same continuum escape model. Solid contours represent lines of constant $f_{esc}\xi_{ion}$ and $f_{esc}\kappa_{ion}$ whilst the dashed contour shows where $\beta = -2$ is located for reference. The green labelled contour shows the assumed $f_{esc}\xi_{ion} = 24.5$ value of Robertson *et al.* (2013) and the equivalent in $f_{esc}\kappa_{ion}$ (see text for details). For the colour scales below the centre and right panels, the lower black tick labels correspond to the scale for the fiducial model ($Z = 0.2Z_\odot$) whilst the grey upper tick label indicate how $f_{esc}\xi_{ion}$ and $f_{esc}\kappa_{ion}$ change for stellar populations with solar metallicity. 92
- 3.7 Evolution of $\log_{10} f_{esc}\xi_{ion}$ (top panels) and $\log_{10} f_{esc}\kappa_{ion}$ (bottom panels) vs β as a function of changes in the stellar population age (green dashed), metallicity (red dotted), dust extinction (yellow dot-dashed) and escape fraction (blue continuous) with the remaining parameters fixed to the fiducial values listed in Table 3.1. Values are plotted for both the ionization bounded nebula with holes (Model A; left panels) and density bounded nebula (Model B; right panels). Some individual points are labelled for both Lyman continuum escape models to illustrate the range and differences in evolution between each model. Note that the small difference in β between Model A and Model B for the case of zero-dust ($0A_V$) is due to the difference in nebular emission contribution for the two models; $f_{esc,neb} = 0.17$ and $f_{esc,neb} = 0.5$ for models A and B respectively. 95

List of Tables

2.1	Short caption	19
2.2	Short caption	23
2.3	Short caption	46
2.4	Short caption	49
2.5	Short caption	52
2.6	Short caption	57
3.1	Summary of the stellar population model assumptions	94
A.1	Calculated values of ρ_{UV} and \dot{N}_{ion} for the different integration limits and efficiency assumptions explored in the paper, based on the luminosity function parametrisations of Bouwens <i>et al.</i> (2014b). For each calculated value, we include statistical errors from the uncertainties in the Schechter (1976) parameters and β observations. Also shown are the effects of some of the assumptions made in Section 3.3.1 and their corresponding systematic changes to the estimated values.	114
A.2	Calculated values of ρ_{UV} and \dot{N}_{ion} for the different integration limits and efficiency assumptions explored in the paper, based on the luminosity function parametrisations of Finkelstein <i>et al.</i> (2014). For each calculated value, we include statistical errors from the uncertainties in the Schechter (1976) parameters and β observations. Also shown are the effects of some of the assumptions made in Section 3.3.1 and their corresponding systematic changes to the estimated values.	115

My Thesis Title

Chapter 1

Introduction

One of the most remarkable achievements in physical sciences over the last few decades is the precision to which cosmologists have been able measure the initial conditions of our Universe. We know very well how it all began 13.8 billion years ago and what the starting ingredients were. From the panoply of stars, planets and galaxies we see around us today, we also have a good grasp on what those ingredients eventually became. The challenge facing Astronomy is to fill in the gaps in that long history and shed light on those ages to which we are still in the dark.

1.1 The Early Universe

What makes the remarkable measurements of the initial conditions in our Universe possible is the detailed observation of the oldest cosmic microwave background (CMB). Famously discovered accidentally by Arno Penzias and Robert Wilson in 1964 (Penzias & Wilson, 1965) but independently postulated several times in the preceding decades, the CMB represents the oldest light in the Universe. For the first $\sim 373,000$ years after the Big Bang all baryonic matter in the Universe – including free electrons, protons and neutrons – was coupled together in a hot, uniform, radiation-filled hydrogen plasma. As the Universe expanded and grew cooler, the electrons and protons eventually cooled enough to form neutral atoms ('recombination') shortly before cooling far enough to allow photons to freely stream through space ('decoupling'). It is those primordial photons which have been propagating through space and slowly

cooling until this date to produce the cosmic microwave background we observe today.

Since the initial measurements of the CMB 50 years ago, a succession of ground-based, balloon-borne and eventually space-based telescopes have measured the CMB with increasing precision. Despite initially appearing uniform in all directions, in 1992 data from the Cosmic Background Explorer (COBE) satellite indicated minute variations in the temperature of the CMB on small scales¹. These anisotropies have since been measured to exquisite precision by the Wilkinson Microwave Anisotropy Probe (WMAP) and Planck experiments, leading to strong support for the favoured model of Λ -Cold Dark Matter cosmology.

Imprinted by primordial quantum fluctuations,

Our current understanding of the Universe is of one consisting of $30.89 \pm 0.62\%$ matter and $69.11 \pm 0.62\%$ (Planck Collaboration *et al.*, 2015)

1.2 Studying distant galaxies

QSOs at cosmological distances: Schmidt (1965)

Star-forming galaxies: (Partridge & Peebles, 1967)

QSOs are $z \gtrsim 4$ (Guhathakurta, Tyson & Majewski, 1990)

(Steidel & Hamilton, 1992)

Normal star-forming galaxies at $z \gtrsim 4$ (?) (?) (Madau *et al.*, 1996)

(Steidel *et al.*, 1999)

(Thompson, Weymann & Storrie Lombardi, 2001), (Thompson, 2003), (Fontana *et al.*, 2003), (Giavalisco *et al.*, 2004a), (Dickinson *et al.*, 2004), (Capak *et al.*, 2004), (Stanway, Bunker & McMahon, 2003), (Stanway *et al.*, 2004a)

Text of chapter.

¹Re-analysis of data from the Soviet RELIKT-1 anisotropy experiment did in fact lead to publication of anisotropy results several months before the COBE announcement (re-published in Strukov *et al.* 1992). However it was the COBE results for which the Nobel prize was later awarded.

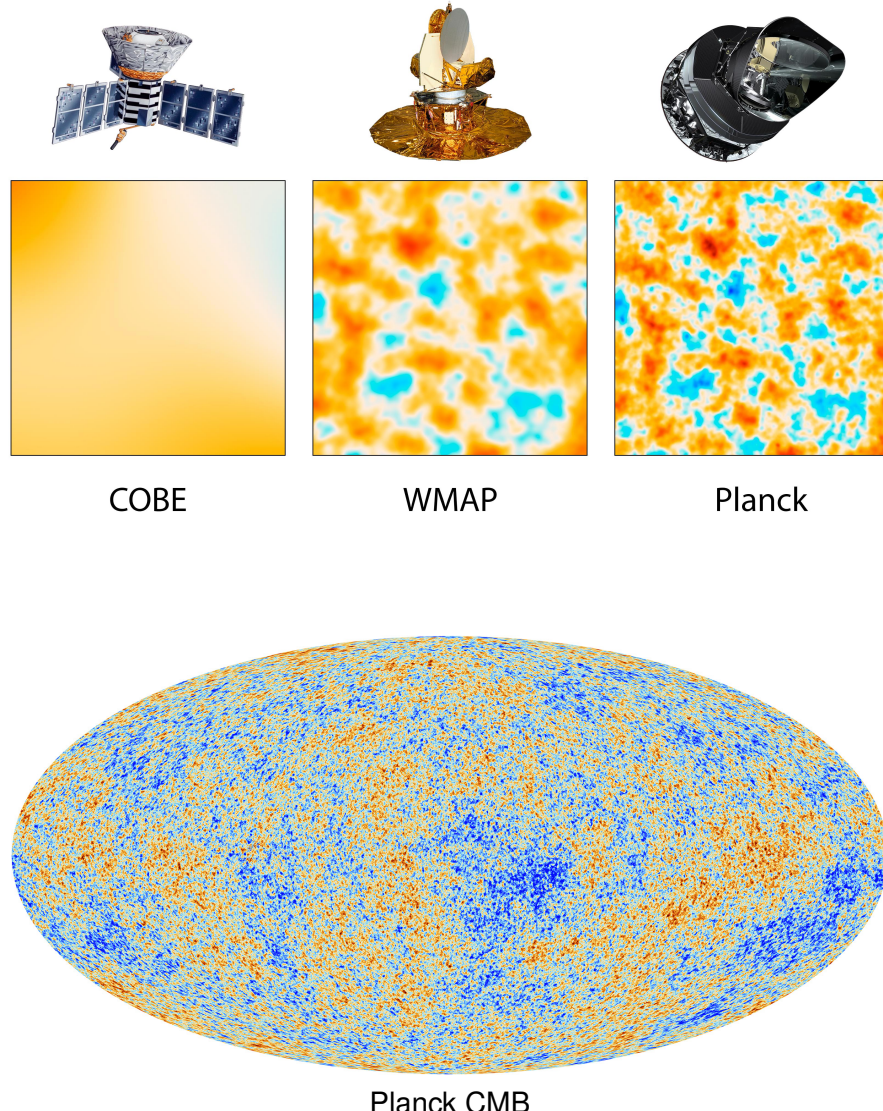


Figure 1.1: Top: Long caption Credit – NASA/JPL-Caltech/ESA Bottom: Credit – ESA and the Planck Collaboration

1.3 Estimating galaxy stellar masses

Using the panchromatic spectral energy distribution (SED) of a galaxy to estimate its stellar mass (or other physical property of interest) has become an increasingly popular and powerful technique. At its simplest, the shape of a galaxy's SED tells us about the mass-to-light ratio, M_*/L , and therefore its overall normalisation can be used to estimate the corresponding total stellar mass. The shape of the SED itself (and hence the M_*/L) itself is a product of almost every underlying physical property of the galaxy which can tell us about both the past and present stellar population.

Firstly, the age of the underlying stellar population (and by association the galaxy's

star-formation history) as well its metallicity and chemical enrichment history are encoded into the stellar emission. Secondly, the initial stellar emission is then processed by the surrounding gas and dust, so the observed SED is also a function of the distribution, mass and grain sizes of the dust within a galaxy.

Just what can be learned from the integrated light of a galaxy is highly dependent both on the quality of the data (including whether it is photometric or spectroscopic) and the model ingredients used to interpret that data.

...

When using SPS to interpret galaxy SEDs, the basic building blocks are simple stellar populations (SSPs) – the SED of a single stellar population formed at the same time with a single metallicity and initial mass function (IMF). The construction of SSPs requires stellar spectral libraries and stellar isochrones for a given metallicity

Crucially, since the outputs of these models is simply the flux as a function of wavelength for a given set of population parameters, they can both be easily compared with each other and used in identical ways. With a suite of SSPs, composite stellar populations (CSPs) can then be constructed to simulate more complicated star-formation and metallicity histories along with the effects of

In theory, $SFR(t)$ and $P(Z, t)$ can be arbitrarily complex. However, in practice this would require huge computational expense and with most data lead to minimal increase in accuracy for estimates of stellar masses over simpler model assumptions. Two such simplifications are commonly made, firstly that for a given composite stellar population the metallicity is fixed a single value. Secondly, the SFH can be parametrised as a simpler time dependent function with one or more parameters.

Most commonly used is a SFH which decays exponentially over some characteristic timescale, τ , such that $SFR(t) \propto \exp(-t/\tau)$. More recently, it has been shown that rising star-formation models (e.g. negative τ 's) are both a better fit to the observed photometry of high-redshift galaxies (Maraston *et al.*, 2010) and a better representation of the theoretical predictions from simulations (Finlator, Oppenheimer & Davé, 2011; Dayal *et al.*, 2013).

OTHER SIMPLE PARAMETRISATIONS USED

Another novel approach to constructing plausible and accurate star-formation and metallicity history is that of Pacifici, whereby a large number of SFR and Z histories from semi-analytic models are used to construct a set of CSPs for fitting.

However the SFR and metallicity histories of models are parametrised, what is most important is that the chosen models can accurately represent the full dynamic range of observed galaxy photometry and give un-biased estimates of the stellar population properties we are interested in measuring. At $z > 3$, when the Universe is less than ~ 2 Gyr old, the limited ages of stars possible means that degeneracies introduced into SED fitting from the SFH alone are somewhat reduced. (Schaerer, deBarros & Sklias, 2013) found...

METALLICITY

Another critical assumption in the use of SPS modelling is the choice of initial mass function. Without direct measurements of the IMF in distant galaxies, we are limited to the assumption of locally measured IMF such as the canonical Salpeter (1955) or Chabrier (2003) and Kroupa (2001) functions.

1.4 The CANDELS survey

Regions of the sky which have been well studied by the *Hubble* Space Telescope, such as the GOODS fields (Giavalisco *et al.*, 2004b), have become increasingly valuable resources for studying the evolution of galaxies and build-up of black holes through cosmic time. This is thanks to the ever-growing wealth of observations across the whole electromagnetic spectrum and the extreme depths reached by these observations. However, the deep fields such as GOODS North and South cover only very small areas of the sky ($\sim 320 \text{ arcmin}^2$ combined for Hubble data). This leads to large uncertainties in galaxy counts due to cosmic variance and also makes them poor for studying rare bright (/massive) objects.

While the deep optical coverage is allowed the Lyman break selection of galaxies out to $z \sim 6$ and provided rest-frame optical morphologies of lower redshift galaxies, in order to extend this analysis to greater redshifts requires near-infrared observations of

comparable depth to those existing at shorter wavelengths. Infrared surveys reaching to depths of $H_{160} \gtrsim 26$ were possible with the NICMOS camera but were severely limited by the survey efficiency of the instrument with respect to its optical counterpart, ACS. The GOODS NICMOS Survey (GNS,) observed parts of the GOODS North and South fields to a depth of $H_{160} \sim 26.5$ (cf. $V_{606} = 27.8$ (Giavalisco *et al.*, 2004b)). Surveying XX arcmin² to this depth in just one single filter required 180 orbits of Hubble observations. Clearly, extending such a survey to more filters and significantly greater areas was not feasible with the existing facilities. Furthermore, using ground-based facilities the required depths are just not possible even with the largest 8m+ telescopes.

Thankfully, the greatly improved capabilities of the Wide Field Camera 3 (WFC3), installed in *Hubble* as part of the final service mission, such a task was made considerably more feasible.

Efficiency plot

The CANDELS project (Cosmic Assembly Near-infrared Deep Extra-galactic Legacy Survey) leverages the new infrared capabilities to make observations which are both deeper and more extensive than previously available for the key legacy fields. ... awarded 900 orbits etc.

In the context of the many outstanding questions in galaxy formation and evolution, the CANDELS survey set out with a wide range of primary scientific goals in four key areas:

1. *Cosmic Dawn*: the formation and early evolution of galaxies ($z > 4$)
2. *Cosmic High Noon*: the peak of star-formation and AGN activity ($1 < z < 3$)
3. Ultraviolet Observations: Host stars at $1 < z < 3.5$
4. Supernovae: Standardizable candels beyond $z \sim 1$

“CD1 Improve constraints on the bright end of the galaxy LF at $z \approx 7$ and 8 and make $z \approx 6$ measurements more robust. Combine with WFC3/IR data on fainter magnitudes to constrain the UV luminosity density of the universe at the end of the reionization era

CD2 Constrain star formation rates, ages, metallicities, stellar masses, and dust contents of galaxies at the end of the reionization era, $z \approx 6 - 10$. Tighten estimates of the evolution of stellar mass, dust, and metallicity at $z = 4 - 8$ by combining WFC3 data with very deep Spitzer IRAC photometry”

The final survey program involved observations of five key extra-galactic survey fields – GOODS South, GOODS North, the extended Groth strip (EGS), the UKIDSS Ultra Deep Survey (UDS) and the COSMOS field – with observations of these fields split into two distinct tiers. The first (and deepest) of these tiers, hereafter CANDELS/Deep, is primarily comprised of observations over parts of the GOODS North and South (totalling XX) to a depth of ~ 13 Hubble orbits. The second shallower tier (CANDELS/Wide) consists of observations over all five fields to a depth of $\sim 2 - 3$ orbits per tile and covering YY.

The first deep field completed was the GOODS South field and was chosen as the basis for the majority of the analysis undertaken throughout this thesis. Full details of this dataset can be found in Guo *et al.* (2013), including the data reduction and homogenisation of the respective space and ground-based ancillary data.

1.5 Thesis Outline

Chapter 2

The mass evolution of the first galaxies: stellar mass functions and star formation rates at $4 < z < 7$ in the CANDELS GOODS-South field

2.1 Introduction

Thanks to the unprecedented sensitivity of the latest extragalactic surveys, the last decade has seen a revolution in the observations of galaxies in the high-redshift universe. It is now possible to study the beginnings of the mechanisms and processes which formed the diverse array of galaxies we find in the local universe today. Since the first successful detections through the Lyman break technique, via the characteristic ‘break’ induced by blanketing hydrogen absorption of the UV continuum (Guhathakurta, Tyson & Majewski, 1990; Steidel & Hamilton, 1992), the study of high-redshift galaxies has progressed rapidly. With the introduction of the Wide-field Camera 3 (WFC3) in 2009 and the unprecedented depth in the near-infrared it provides, the study of galaxies out to redshifts of $z > 6$ has become commonplace.

The numerous measurements of the UV luminosity function of high-redshift galaxies spanning the redshift range $4 \leq z \leq 9$ (Bouwens *et al.*, 2007; McLure *et al.*, 2009;

Oesch *et al.*, 2009; Bouwens *et al.*, 2010; Grazian *et al.*, 2011; Lorenzoni *et al.*, 2011; McLure *et al.*, 2013; Schenker *et al.*, 2013b) are not only giving an insight into the processes of galaxy formation, they are also helping us to understand the role those galaxies played in the ionization of the intergalactic medium during the epoch of reionization (EoR). These surveys have put strong constraints on the contribution of star-forming galaxies to reionization, requiring a significant contribution from faint galaxies below the current detection limits to complete reionization within the observed redshift.

Because they represent the time integral of all past star-formation, the stellar masses of galaxies provide additional independent constraints on their contribution to reionization through the observed stellar mass density (Robertson *et al.*, 2010). Successful models of galaxy evolution and reionization must therefore be able to reconcile both the star-formation observed directly, and the record of past star-formation contained in the observed stellar masses. The galaxy stellar mass function (SMF) and its integral the stellar mass density (SMD), are therefore important tools in the study of galaxy evolution.

However, accurately measuring the stellar masses of galaxies at high-redshift is very difficult for a number of fundamental reasons. These reasons stem from the fact that the rest-frame wavelengths probed by optical/near-infrared surveys extend only to the UV continuum, requiring mid-infrared observations to extend past $\lambda_{rest} = 4000\text{\AA}$. Even when rest-frame optical measurements are available through deep *Spitzer* 3.6 and 4.5 μm observations, e.g. Stark *et al.* (2009); Labb   et al. (2010); Gonz  lez *et al.* (2011); Yan *et al.* (2012), the degeneracies between dust extinction, age and metallicity are large (see Dunlop 2012 for a detailed discussion).

More recently it has also been shown that the spectral energy distributions (SEDs) of high-redshift galaxies, for both photometrically selected (Schaerer & deBarros, 2009, 2010; Ono *et al.*, 2010; McLure *et al.*, 2011; Lorenzoni *et al.*, 2011; Gonz  lez *et al.*, 2012) and smaller spectroscopically confirmed samples (Shim *et al.*, 2011; Curtis-Lake *et al.*, 2013; Stark *et al.*, 2013), can exhibit colours which are best fit by the inclusion of nebular emission lines when measuring galaxy properties such as mass and age. The inclusion of these lines results in fitted ages which are significantly younger compared to fits without nebular emission, as well as being of lower stellar

mass. Another consequence of the degeneracies in SED fitting at high-redshift is the increased importance in the assumed star formation history (SFH) of the models being fit. Observational studies of the mass growth of galaxies at a constant number density (Papovich *et al.* 2011, Salmon *et al.* 2014) and hydrodynamical simulations (Finlator, Oppenheimer & Davé, 2011) imply that the star formation histories for galaxies at $z > 3$ are smoothly rising. This is in contrast to the smoothly falling or constant SFH commonly used at low-redshift (see Conroy 2013 for a review). In Maraston *et al.* (2010), it is also shown that exponentially rising star-formation histories can provide improved fits to both simulated and observed SEDs of high redshift galaxies.

González *et al.* (2011) were amongst the first to make use of the capabilities offered by the WFC3/IR data, using data from the Early Release Science (ERS; Windhorst *et al.* 2011) to measure the stellar mass to UV luminosity ratio for a sample of dropout galaxies and applying it to the observed luminosity functions to measure the stellar mass function out to $z \sim 7$. In contrast to the steep faint-end slope of the UV luminosity function ($\alpha = -2$ to -1.7) at high-redshifts, this work observed a notably shallower mass function ($\alpha = -1.6$ to -1.4). Subsequent work by Lee *et al.* (2012) with much greater sample sizes from ground-based near-infrared found a similarly shallow slope at $z \sim 4$ and 5. In contrast, observations by Caputi *et al.* (2011) and Santini *et al.* (2012) observe a significantly steeper low-mass slope at $z > 3$.

In González *et al.* (2011), the shallow low-mass slope arises due to the observed evolution of the mass-to-light ratio with UV luminosity. Similarly, Lee *et al.* (2012) infer an evolving mass-to-light in order to reconcile the luminosity and mass function slopes observed. The primary physical explanation for this evolving mass-to-light ratio is luminosity dependent dust-extinction. However, observations of the stellar populations of high-redshift galaxies have produced conflicting results on the existence and strength of any luminosity dependence. When measuring the UV continuum slope, β (Calzetti, Kinney & Storchi-Bergmann, 1994), for samples of high-redshift galaxies, Wilkins *et al.* (2011), Bouwens *et al.* (2012a) and Bouwens *et al.* (2014a) find evidence for a strong UV luminosity dependence across all redshifts at $z > 3$. In contrast, similar studies by Dunlop *et al.* (2011), Finkelstein *et al.* (2012b) and Rogers, McLure & Dunlop (2013) find no clear evidence for a luminosity dependence on β . Several of

these studies outline the importance of the selection of high redshift galaxies (through either Lyman break or photometric redshift selection) and the treatment of their biases. To this end, more recent analyses (Bouwens *et al.*, 2014a; Rogers *et al.*, 2014) which increase sample sizes and minimise biases in the sample selection and β measurements are in good agreement, with both studies finding a clear luminosity dependence.

The deep near-infrared observations of the GOODS South field made as part of the Cosmic Assembly Near-infrared Deep Extragalactic Survey (CANDELS; Co-PIs: Faber & Ferguson; Grogin *et al.* 2011; Koekemoer *et al.* 2011), combined with the extensive existing optical observations make it a data set ideally suited to the study of galaxy evolution at the so-called ‘cosmic dawn’. Covering an area approximately 200% larger than the WFC3 ERS observations alone (Windhorst *et al.*, 2011), and incorporating the even deeper UDF observations, the CANDELS data combines the high sensitivity of the WFC3 observations with high-redshift samples large enough to attempt the first direct derivation of the stellar mass function at $z > 5$. In this paper, we make use of this comprehensive data set to study galaxy stellar masses across the redshift range $z \sim 4$ to $z \sim 7$. In particular, we aim to estimate stellar masses for a large and robust sample of high-redshift galaxies, investigating how the inclusion of nebular emission and increasing star-formation histories affect the observed stellar mass - UV luminosity relation and the shape of the stellar mass function. For this same sample, we also aim to measure the dust-corrected star-formation rates which will combine to make a detailed census of the stellar mass growth of high-redshift galaxies.

The structure of this paper is as follows. In Section 2.2, we describe the properties of the optical and near-IR data sets used in this study as well as the methods of photometry extraction used. In Section 2.3, we describe the photometric redshift analysis and the selection criteria used to construct the high-redshift samples used in our analysis. The SED fitting method used to estimate the stellar masses for our sample is outlined in Section 2.5. Section 2.5.5 then describes the simulations undertaken to account for the effects of completeness and sample selection. In Section 3.4 we present the results of this work and our analyses. Finally, Section 3.6 presents our summary and conclusions of the work in this paper. Throughout this paper all magnitudes are quoted in the AB system (Oke & Gunn, 1983) and we assume a Λ CDM cosmology with

$H_0 = 70 \text{ kms}^{-1}\text{Mpc}^{-1}$, $\Omega_m = 0.3$ and $\Omega_\Lambda = 0.7$. Quoted observables are expressed as actual values assuming this cosmology. Note that luminosities and luminosity based properties such as observed stellar masses and star-formation rates scale as h^{-2} , whilst densities scale as h^3 .

2.2 The Data

The photometry used throughout this work is taken from the catalog of Guo *et al.* (2013), a UV to mid-infrared multi-wavelength catalog in the CANDELS GOODS South field based on the CANDELS WFC3/IR observations combined with existing public data.

2.2.1 Imaging Data

The near-infrared WFC3/IR data combines observations from the CANDELS survey (Grogin *et al.*, 2011; Koekemoer *et al.*, 2011) with the WFC3 Early Release Science (ERS; Windhorst *et al.* 2011) and Hubble Ultra Deep Field (HUDF; PI Illingworth; Bouwens *et al.* 2010) surveys. The southern two thirds of the field (incorporating the CANDELS ‘DEEP’ and ‘WIDE’ regions and the UDF) were observed in the F105W, F125W and F160W bands. The northern-most third, comprising the ERS region, was observed in F098M, F125W and F160W. In addition to the initial CANDELS observations, the GOODS South field was also observed in the alternative J band filter, F140W, as part of the 3D-HST survey (Brammer *et al.* 2012).

The optical HST images from the Advanced Camera for Surveys (ACS) images are version v3.0 of the mosaicked images from the GOODS HST/ACS Treasury Program, combining the data of Giavalisco *et al.* (2004b) with the subsequent observations obtained by Beckwith *et al.* (2006) and (Koekemoer *et al.*, 2011). The field was observed in the F435W, F606W, F775W, F814W and F850LP bands. Throughout the paper, we will refer to the HST filters F435W, F606W, F775W, F814W, F850LP, F098M, F105W, F125W, F160W as B_{435} , V_{606} , i_{775} , I_{814} , z_{850} , Y_{098} , Y_{105} , J_{125} , H_{160} respectively.

The *Spitzer*/IRAC (Fazio *et al.*, 2004) 3.6 and $4.5\mu\text{m}$ images were taken from the

Spitzer Extended Deep Survey (PI: G. Fazio, Ashby *et al.* 2013) incorporating the pre-existing cryogenic observations from the GOODS Spitzer Legacy project (PI: M. Dickinson). Complementary to the space based imaging of HST and Spitzer is the ground-based imaging of the CTIO U band, VLT/VIMOS U band (Nonino *et al.*, 2009), VLT/ISAAC K_s (Retzlaff *et al.*, 2010) and VLT/HAWK-I K_s (Fontana *et al.* *in prep.*) bands.

2.2.2 Source photometry and deconfusion

The full details on how the source photometry was obtained are outlined in Guo *et al.* (2013), however we provide a brief summary of the method used for reference here. Photometry for the HST bands was done using SExtractor’s dual image mode, using the WFC3 H band mosaic as the detection image and the respective ACS/WFC3 mosaics as the measurement image after matching of the point-spread function (PSF).

For the ground-based (VIMOS and CTIO U band and ISAAC and Hawk-I K_s) and Spitzer IRAC bands, deconvolution and photometry was done using template fitting photometry (TFIT). We refer the reader to Laidler *et al.* (2007), Lee *et al.* (2012) and the citations within for further details of the TFIT process and the improvements gained on mixed wavelength photometry.

2.3 Photometric Redshifts and Sample Selection

Photometric redshifts for the entire source catalog were calculated using the EAZY photometric redshift software (Brammer, vanDokkum & Coppi, 2008). The fitting was done to all available bands using the default reduced template set based on the PEGASE spectral models of Fioc & Rocca-Volmerange (1997) with an additional template based on the spectrum of Erb *et al.* (2010). The additional template exhibits features expected in young galaxy populations such as strong optical emission lines and a high Lyman- α equivalent width.

For each galaxy we construct the full redshift probability distribution function (PDF), $P(z) \propto \exp(-\chi_z^2/2)$, using the χ^2 -distribution returned by EAZY. Although EAZY

allows the inclusion of a magnitude based prior when calculating redshifts, none was included in the fitting due to the large uncertainties still present in the H-band (our photometry selection band) luminosity function at high-redshifts (?).

2.3.1 Selection Criteria

To investigate how the SMF evolves from $z = 4\text{--}7$, we wish to construct a sample of galaxies in the redshift range $3.5 < z < 7.5$. To select a robust sample suitable for SED fitting, we apply a set of additional criteria based on the full redshift probability distribution for each galaxy to construct the different redshift samples, similar to those used in previous high-redshift sample selections (McLure *et al.*, 2011; Finkelstein *et al.*, 2012a). We then apply the following criteria:

$$\int_{z_{\text{sample}}-0.5}^{z_{\text{sample}}+0.5} P(z) dz > 0.4 \quad (2.1)$$

$$\int_{z_{\text{peak}}-0.5}^{z_{\text{peak}}+0.5} P(z) dz > 0.6 \quad (2.2)$$

$$(\chi^2_{\min}/N_{\text{filters}} - 1) < 3 \quad (2.3)$$

where $z_{\text{sample}} = 4, 5, 6$ and 7 for the respective bins and z_{peak} is the redshift at the peak of the probability distribution (i.e. minimum χ^2).

The first criterion (Equation 2.1) requires that a significant amount of the probability distribution lies within the redshift range we are examining. The second criterion (Equation 2.2) requires that the bulk of the PDF lies close to the peak of the distribution, i.e. that the primary solution is a dominant one. Finally, we require that EAZY provides a reasonable fit to the data (Equation 2.3).

A signal to noise (S/N) cut is placed on the J and H bands, requiring $S/N(J_{125}) > 3.5$ and $S/N(H_{160}) > 5$. Known AGN, stars and sources with photometry flagged as effected by artefacts are removed. We also visually inspect each galaxy across all the HST bands, excluding sources which were caused or strongly affected by artefacts

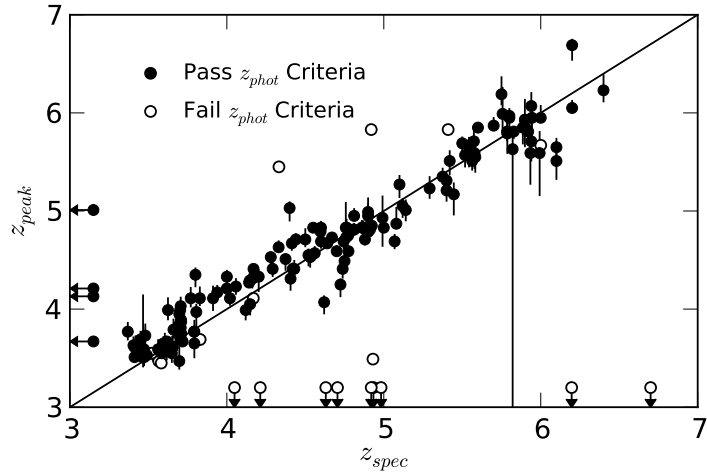


Figure 2.1: Comparison between spectroscopic and photometric redshift for the galaxies in our sample with available spectroscopy and spectroscopic redshift quality of ‘Good’ or better. Filled circles show sources which pass our selection criteria (including interlopers), empty circles show spectroscopically confirmed high-redshift sources which do not pass the selection criteria. The photometric redshift shown is the peak of the probability distribution (χ^2 minimum) with $1-\sigma$ lower and upper limits.

such as diffraction spikes, bright stars and image edges which were not excluded by any of the other criteria.

Of the initial 34930 objects in the CANDELS GOODS South catalog, 3164 objects satisfy our first criterion. Of those objects, 256 are excluded by the second criterion and a further 167 are rejected based on their χ^2 . The signal to noise criteria exclude a further 274 sources and the remaining criteria exclude a further 204 sources. The resulting final sample comprises 2263 galaxies.

Figure 2.1 compares the available spectroscopic redshifts for the galaxies in our sample with the corresponding best-fit photometric redshift (minimum χ^2) as found by EAZY. In total, there are 151 spectroscopic redshift matches for galaxies which pass our selection criteria and are therefore included in our samples. In addition, there are a further 21 galaxies with spectroscopic redshifts of $z > 3.5$ which pass the signal to noise, AGN criteria but do not pass the photometric redshift criteria. Of these 21 galaxies, 12 are correctly identified as high redshift galaxies but are excluded due to poor fits (11) or have a redshift very close to the $z = 3.5$ limit but photometric scatter pushes the photometric redshift to below the criteria (1). The remaining 9 spectroscopically confirmed high-redshift sources have best-fit photometric redshifts of $z_{peak} < 3$. The simulations undertaken to correct for selection completeness are outlined in Section 2.5.5.1.

For the matched galaxies which pass our selection criteria, we find that our redshift accuracy is very good, with a scatter of just $\sigma_{z,O} = rms(\Delta z / 1 + z_{\text{spec}}) = 0.037$ when outliers are excluded, where $\Delta z = (z_{\text{spec}} - z_{\text{phot}})$ (Dahlen *et al.*, 2013). We define outliers as $|\Delta z| / (1 + z_{\text{spec}}) > 0.15$, and find an outlier fraction of 2.65% (4 galaxies). This compares with Finkelstein *et al.* (2012b) who find a scatter of $\sigma_z / (1 + z) = 0.044$ at $z > 3$ after excluding outliers (defined more strictly as $|\Delta z| > 0.5$) in the same CANDELS field. We also find that there is very little bias in our photometric redshifts, with $median(\Delta z) = -0.04$. Of the 4 galaxies classed as outliers, all lie at redshifts of $z < 3$ and are low-redshift interlopers which our selection criteria have not been able to exclude.

Dahlen *et al.* (2013) have recently shown that by combining the results from multiple photometric redshift codes, the scatter and outlier fraction in photometric redshifts can be significantly reduced compared to the results of any single code. For the same set of 151 spectroscopic redshift sources, the photometric redshifts produced through the Bayesian combination outlined in Dahlen *et al.* (2013) have $\sigma_{z,O} = 0.033$ with an outlier fraction of 3.98% and $median(\Delta z) = 0.01$.

Although utilising the photometric redshifts for the CANDELS GOODS-S field produced by this method would result in a small gain in photometric accuracy, we would no longer be able to reproduce the full selection method when running simulations. Given this small improvement, we are confident that the use of photometric redshifts produced by a single code will not adversely affect the overall accuracy of the results.

The matched spectroscopic redshifts are from the following surveys: Le Fèvre *et al.* (2004); Stanway *et al.* (2004b); Vanzella *et al.* (2008); Hathi, Malhotra & Rhoads (2008); Popesso *et al.* (2009); Wuyts *et al.* (2009); Rhoads *et al.* (2009); Vanzella *et al.* (2009); Balestra *et al.* (2010); Kurk *et al.* (2012). The high-redshift spectroscopic sources within these surveys all derive from initial target selections of predominantly bright Lyman Break galaxy candidates. The measured photometric redshift accuracies are therefore likely biased to a better scatter than the full high-redshift galaxy population. However, examining the redshift accuracy of the mock galaxy catalog used for our selection comparisons in Appendix 2.4, we find that the photometric redshift accuracy remains good down to the lowest masses probed in this survey for galaxies

which pass our criteria. For example, for galaxies of $M_* \approx 10^{8.5} M_\odot$, we find a scatter excluding outliers of $\sigma_{z,O} = 0.053$ and $median(\Delta z) = 0.025$ before any $P(z)$ criteria are applied.

To investigate how the SMF evolves from $z = 4\text{--}7$, we then constructed four redshift samples in bins across this redshift range: $z \sim 4$ ($3.5 \leq z < 4.5$), $z \sim 5$ ($4.5 \leq z < 5.5$), $z \sim 6$ ($5.5 \leq z < 6.5$) and $z \sim 7$ ($6.5 \leq z < 7.5$).

2.3.2 Monte Carlo Samples

Although we find that our photometric redshifts do well when compared with the matched spectroscopic redshifts, the group of outliers are indicative of the difficulties that exist in correctly distinguishing between the Lyman break of high-redshift galaxies at $z > 3$ and strong Balmer break galaxies at more moderate redshifts $z \approx 0.5\text{--}2.5$ in low S/N data. Pirzkal *et al.* (2012, 2013) have shown that it is very difficult to categorically classify sources as high-redshift galaxies and not low-redshift interlopers using photo-z's or S/N criteria on the dropout bands.

Previous work using photometric redshifts has dealt with this problem by making use of the full redshift PDF when calculating luminosity functions (Dahlen *et al.*, 2005; McLure *et al.*, 2009, 2013), thereby incorporating the uncertainty in the analysis. Due to the nature of the SED fitting code used for this work (described in Section 2.5), the computational effort required to fit the mass at each redshift in order to integrate over the full PDF becomes impractical. As such, we chose to account for these problems in a different manner whilst still dealing with them in a straight-forward way.

Rather than using only the best-fit redshift from our photometric analysis when selecting our sample, we instead draw the redshift for each galaxy randomly from its full PDF before placing it in the appropriate redshift sample. Where secure spectroscopic redshifts are available, we fix the redshift to that value for all samples (known interlopers are therefore excluded in all samples). This process was repeated 500 times to produce a set of samples to which we then apply the rest of the analysis described in the paper separately. We then average over the results from each sample, using the mean of this full set as our ‘true’ value along with the $1-\sigma$ upper and lower limits around this

Table 2.1: Average sample size and variance for each redshift bin for the 500 Monte Carlo samples generated, see text for details.

Redshift Bin	Mean Sample Size	Variance on sample size
4	1235	180
5	416	63
6	169	25
7	42	9

mean.

The resulting sample sizes for each redshift bin are shown in Table 2.1. The varying samples account for both scattering between redshift bins for objects at the boundaries as well as objects moved out of the sample into secondary low-redshift solutions. The effect of this scattering into and out of the samples can be seen when comparing the combined mean samples sizes (1862) to our full high-redshift sample of 2263.

The strength of using photometric redshifts for sample selection over colour cuts (especially when redshifts would still need to be calculated for a colour-cut sample in order to do SED fitting) is that the method can automatically make use of all available photometry. This is important because although photometric redshifts are still fitting primarily to the characteristic break at Lyman- α targeted by the colour selections, the filters long-ward of the break are useful in excluding low-redshift interlopers (McLure *et al.*, 2011). Additionally, the large errors in colour possible due to low signal to noise and possible non-detections in the filter just short of the Lyman break means that likely high-redshift candidates can be scattered well outside the selection region when using colour cuts.

Figure 2.2 shows the positions of our galaxy samples on the colour-colour planes commonly used to select dropout samples. It is obvious that many of the galaxies selected with photometric redshifts lie outside the selection regions (as taken from Bouwens *et al.* 2007), especially those galaxies where colours must be calculated using an upper limit. The agreement (or lack of) between dropout selections and photometric redshifts has also been investigated for GOODS-S specifically by Dahlen *et al.* (2010).

To test whether the discrepancy between the observed colours and those required for Lyman break selection can be explained solely by photometric scatter, we performed a range of tests on a mock catalog generated from the semi-analytic models described

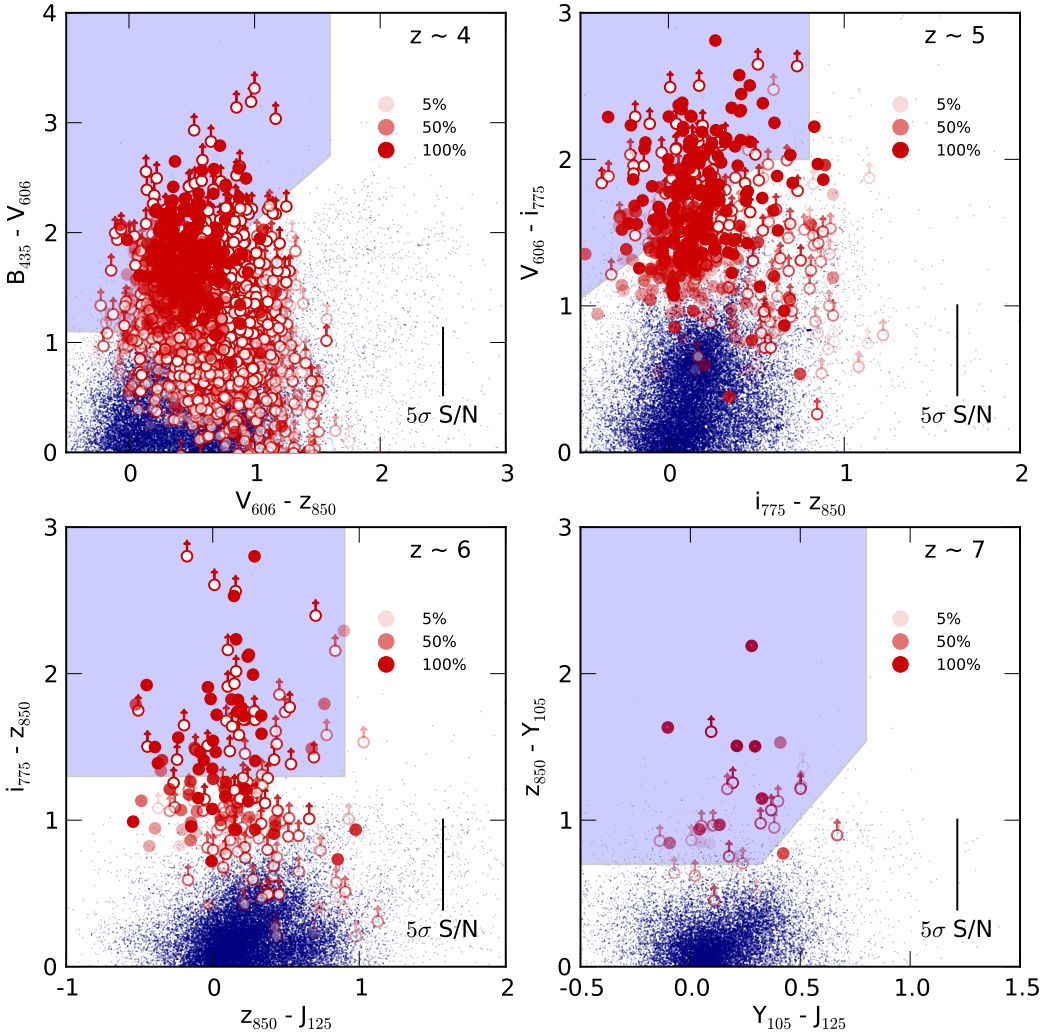


Figure 2.2: The colours of our photometric redshift selected samples in relation to the two-colour cuts typically used to select Lyman break galaxies. Non-detections in a filter are converted to 2σ upper limits when calculating the colours. The shaded blue regions show the region in colour space used to select dropout galaxies in that redshift bin as described in Bouwens *et al.* (2007) and Bouwens *et al.* (2012a). The blue points show the colours for the full GOODS-S photometric catalog from which we select our high redshift samples. Red symbols represent galaxies selected in our sample by our selection criteria, where the transparency of the symbols is determined by the number of Monte Carlo samples in which it is selected i.e. the fainter the symbol, the smaller the fraction of MC samples that galaxy is selected in. The legend in each plot illustrates this transparency for galaxies selected in 5, 50 and 100% of Monte Carlo samples. Colours which make use of 2σ upper limits are plotted with open circles, while objects with 2σ detections or better in all bands are plotted with filled circles. Example error bars corresponding to 5σ detections (for both filters in a given colour) are shown for each of the corresponding drop-out colours.

in Somerville *et al.* (2008) and Somerville *et al.* (2012). Full details of these tests are outlined in Appendix 2.4, however our main finding is that the observed colours can be reproduced from intrinsic Lyman break-like colours and scattering proportional to the observed photometric errors.

2.4 Selection method comparison

Traditionally, (star-forming) galaxies at high-redshift have been selected using the Lyman break technique, whereby galaxies are selected based on the observed colours across the redshifted Lyman break in their spectra.

When the observed colours of our photometric redshift selected galaxies are plotted in the same way, the selected galaxies span a range of colours far wider than those encompassed by the Lyman break galaxy (LBG) selection criteria. Many of the galaxies have colours which would place them in the locus spanned by low-redshift galaxies, according to the Lyman break criteria. This has been observed before by Dahlen *et al.* (2010), who find a similar range of colours for galaxies with photometric redshifts at $z \sim 4$ and 5.

This raises the question as to whether this discrepancy is solely due to photometric scatter in the relevant colours, if they have stellar populations different from those expected for the Lyman break criteria, or if in fact those galaxies outside the selection criteria are low-redshift interlopers or catastrophic failures in the photometric redshift estimation.

To answer these questions, we have taken a sample of mock galaxies from the CANDELS semi-analytic models of Somerville *et al.* (2008) and Somerville *et al.* (2012) across all redshifts. From the full SAM catalog of galaxies from $z = 0$ to $z > 8$, we have included all galaxies at $z > 3$ and a randomly selected sample of a quarter of the galaxies at $z = 3$ and below (subsequent calculations of the interloper fraction fully correct for this reduced number density at $z < 3$). The resulting sample of $\sim 260,000$ galaxies consists of approximately equal numbers of high-redshift galaxies and a fully representative sample of low-redshift galaxies across their corresponding luminosity and colour distributions. For full details of the mock galaxy properties as a function of

redshift we refer the reader to Somerville *et al.* (2008) and Lu *et al.* (2013).

We then assign photometric errors to the intrinsic fluxes in each band based on the observed errors in the original catalog and then perturb the flux by those errors. The resulting colours should then indicate the effects of photometric scattering on the intrinsic colours. We have assumed the errors are gaussian (the fluxes are perturbed by a value drawn from a gaussian where $\sigma = \text{Flux Error}$) and have applied the errors based on the measured flux errors of objects with equivalent fluxes in the UDF, DEEP and WIDE regions.

To further illustrate this process we also select an example galaxy from our mocks which we can follow through the individual steps. The photometric properties of the galaxy and the corresponding photometric errors are outlined in Table ???. The galaxy has a redshift of $z = 5.01$, a stellar mass of $\approx 8 \times 10^8 M_\odot$ and a UV-continuum slope of $\beta = -2.1$.

Table 2.2: Intrinsic magnitudes, fluxes and typical observation errors for the example galaxy and the CANDELS GOODS South region. The first row outlines the true intrinsic fluxes F_{true} in the key filters at $z \sim 5$. In the second row we show the measured 5- σ limiting magnitudes (or fluxes) for the DEEP region estimated in Guo *et al.* (2013) for the photometry used in this paper. The third row shows the average and standard deviation flux error for objects in the photometric catalog (Guo *et al.*, 2013) with fluxes within 0.1 dex of the intrinsic flux for our example galaxy (i.e. the distribution from which our assigned photometric error is drawn). The final row shows the 'observed' fluxes (F_{obs}) for our example galaxy after assigning a flux error σ_F and perturbing the intrinsic flux by a value drawn from a gaussian with width $\sigma = \sigma_F$.

	V_{606}		i_{775}		z_{850}		H_{160}	
	AB	μJy						
Intrinsic Flux - F_{true}	29.35	0.0066	27.14	0.0506	26.83	0.0673	26.91	0.0625
DEEP 5- σ limit	29.35	0.0066	28.55	0.0138	28.55	0.0138	27.36	0.0413
Mean Error ± 1 SD	-	0.0054 ± 0.0028	-	0.0111 ± 0.0057		0.0145 ± 0.0113	-	0.0099 ± 0.0074
'Observed' Flux - F_{obs}	> 27.82	0.009 ± 0.009	27.07	0.054 ± 0.010	26.85	0.066 ± 0.013	27.01	0.057 ± 0.006

The intrinsic colours of the mock galaxies at $z \sim 5$ ($4.5 \leq z < 5.5$) are shown in Figure 2.3. It is clear that the colours spanned by the galaxies lie well within the Lyman break selection criteria of Bouwens *et al.* (2007), with only a small fraction of galaxies redder than the criteria in the colour above the break or bluer across the Lyman break. Our input population therefore closely matches the colours for which the colour-colour criteria have been designed. The same is true across all redshift bins.

The lower panel of Figure 2.3 shows the colours of our mock galaxy catalog after being perturbed by errors drawn from the CANDELS DEEP region. Only galaxies with $S/N(H_{160}) > 5$ are shown, matching the selection criteria for our high-redshift samples, resulting in a sample of 5673 galaxies with $4.5 < z_{\text{true}} < 5.5$. As for our observed objects in Figure 2.2, 2σ upper-limits are used to derive magnitudes for non-detections ($S/N < 2$) and objects with negative fluxes.

It is immediately clear that photometric scatter pushes the colour spanning the Lyman break to values much lower in $V_{606} - i_{775}$ than the range covered by the selection criteria. However, the main locus of galaxies still resides either within or within the typical error of the Lyman break selection region. In addition, the majority of mock galaxies with ‘observed’ $V_{606} - i_{775} < 1$ are those with a non-detection in V_{606} and hence represent a lower limit. The same effect occurs across all regions, with the lower photometric errors in deeper GOODS South region resulting only in a fainter magnitude for an equivalent signal to noise in the optical bands.

The systematic shift towards lower values of $V_{606} - i_{775}$ once photometric scatter is included can be explained by the relative signal-to-noise ratios in the filters above and below the Lyman break. Given the depth of each filter (see Table ??), objects with relatively faint apparent magnitudes above the break and intrinsic colours $> 1 - 2$ will always have a significantly lower signal-to-noise in the filter below the break. In this scenario, V_{606} fluxes which are scattered to higher values will result in a brighter more robust magnitude. Conversely, objects which are scattered to fainter magnitudes are more likely to result in non-detections, requiring the use of upper limits which will push the observed colours down.

These simulations show that high-redshift galaxies can exhibit colours across the Lyman break well outside the traditional selection criteria. However, it is also important

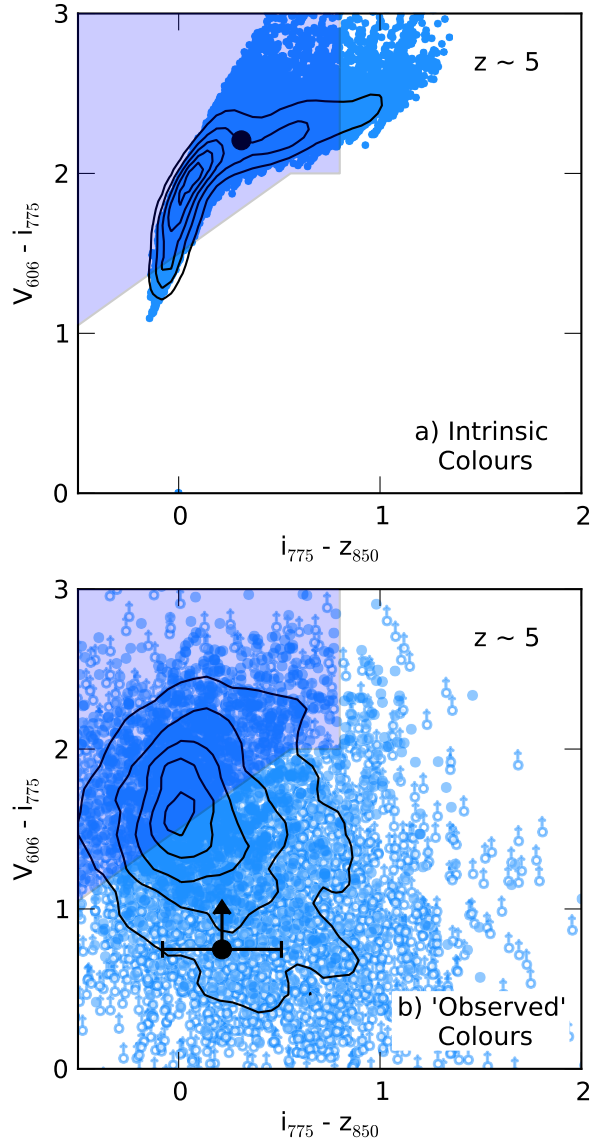


Figure 2.3: a) Intrinsic colours of galaxies at $4.5 < z < 5.5$ from the CANDELS semi-analytic mock catalog. Also shown are contours representing the density of points, with the innermost contour corresponding to five times the density of the outermost contour. The larger black point shows the intrinsic colour of the galaxy from the example outlined in the text. b) Observed colours of galaxies at $4.5 < z < 5.5$ from SAM mock sample after the photometry has been perturbed by flux errors proportional to the observed flux errors in the CANDELS DEEP region of observed photometry. Open circles represent colours constructed from 2σ upper limits. As in a), the innermost contour corresponds to five times the density of points of the outermost contour.

to show that the galaxies selected by photometric redshift with colours outside the colour criteria are indeed these high-redshift galaxies rather than lower redshift galaxies in the same colour space.

To address this, we next calculate photometric redshifts for the SAM mock galaxy sample incorporating the photometric errors using the same method as described in Section 2 and apply our sample selection criteria. By applying additional cuts based on the full $P(z)$ distribution, the number of interlopers can be reduced at the expense of excluding some real sources. How strict the selection criteria are is a balance between minimising the contamination from interlopers and scatter at the bin edges and maximising the number of real high-redshift galaxies in the sample. In Figure 2.4 we show the colours of galaxies which pass our high-redshift selection criteria. The top panel of Figure 2.4 shows those galaxies with $4.5 < z_{\text{true}} < 5.5$, these galaxies span the full range of colours traced by the error perturbed colours of input high-redshift galaxies shown in the previous plots. In the case of the Table ?? example galaxy, the best-fitting photometric redshift is $z = 5.0^{+0.2}_{-0.5}$, 5.2 ± 0.1 and $4.86^{+0.27}_{-0.15}$ for the DEEP, UDF and WIDE errors respectively.

In the bottom panel of Figure 2.4, we show the selected galaxies which have true redshifts outside of the desired redshift range. At $z \sim 5$, the majority of low-redshift ($z < 3$) interlopers which are selected to be $z \sim 5$ by the photometric redshift selection exhibit colours which lie outside of the Lyman break colour criteria. The fraction of low-redshift interlopers is very small compared to the number of ‘real’ high-redshift galaxies in this colour space. However, as redshift increases, the fraction of low-redshift interlopers increases such that at $z \sim 7$ based on the best-fitting z_{peak} alone, the fraction of outliers equals ~ 0.60 , 0.51 and 0.72 for DEEP, UDF and WIDE respectively. Clearly, basing high-redshift samples on the best-fitting photometric redshift alone would produce highly biased samples. Further S/N or photometric criteria such as those used in this work are clearly required to produce a reliable sample.

Applying the selection criteria and generating Monte Carlo samples as outlined in Section 2.3.1, the low-redshift interloper fractions for our mock samples are reduced to an estimated 0.008 , 0.06 , 0.15 and 0.22 for $z \sim 4$, 5 , 6 and 7 respectively. This was estimated by combining the fractions calculated for each field (assuming the ERS

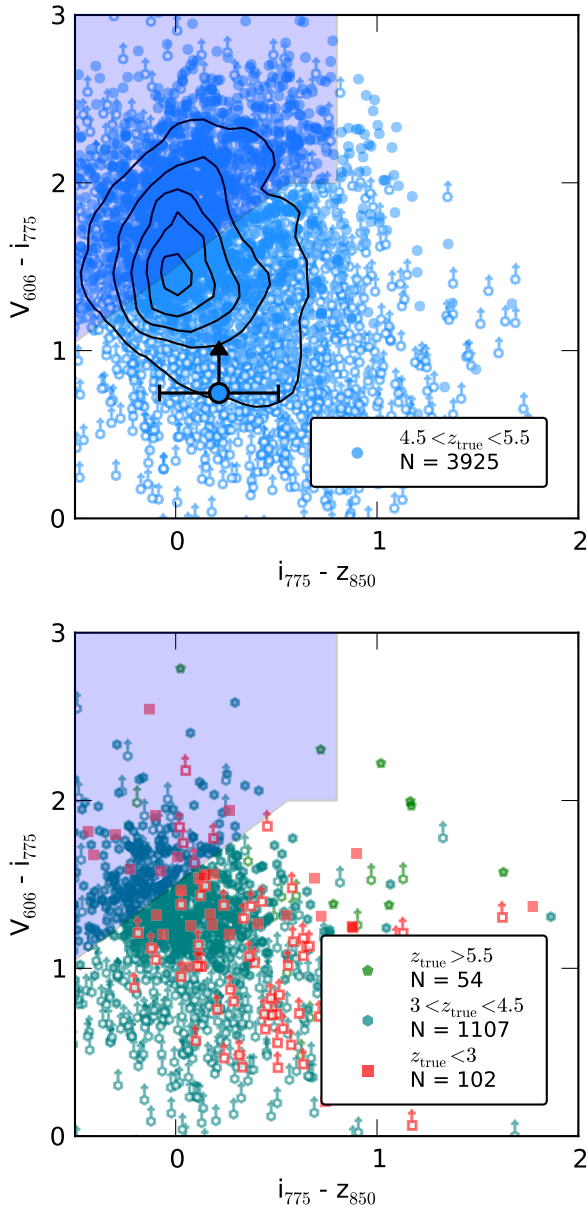


Figure 2.4: *Top:* Observed colours of galaxies from the SAM mock sample which pass our photometric redshift selection criteria, have best-fitting photometric redshifts in the range $4.5 < z_{\text{phot}} < 5.5$ and have true redshifts in the range $4.5 < z_{\text{true}} < 5.5$. As in Figure 2.3, the innermost contour corresponds to five times the density of points of the outermost contour. Open circles with arrows represent colours constructed from 2σ upper-limits. The separately marked large blue circle corresponds to the example galaxy which is correctly estimated to be $z \sim 5$. *Bottom:* Observed colours of galaxies from the SAM mock sample which pass our photometric redshift selection criteria and have best-fitting photometric redshifts in the range $4.5 < z_{\text{phot}} < 5.5$ but have true redshifts outside of the desired redshift bin. As in the top panel, open symbols with arrows represent colours constructed from 2σ upper-limits. In both panels, N is the number of galaxies in the corresponding sample. As outlined in the text, the number of $z_{\text{true}} < 3$ galaxies shown represents a quarter of those expected in a fully representative sample. Using the best-fitting photometric redshift and our selection criteria, the low-redshift interloper fraction for this sample = $(102 \times 4) / (54 + (102 \times 4) + 1107 + 3925) = 0.07$. This low-redshift interloper fraction is reduced to ≈ 0.06 when we generate our Monte Carlo samples.

region to have interloper fractions comparable to the DEEP region) proportional to the number of high-redshift galaxies selected from each region of the field.

The lower panel of Figure 2.4 also highlights the importance of fully incorporating the photometric redshift errors when creating high-redshift galaxy samples. Approximately 20% of the galaxies selected as $z \sim 5$ have true redshifts below the desired range. However upon closer inspection, we find that the median true redshift for the $3 < z_{\text{true}} < 4.5$ points (turquoise hexagons) is 4.4 whilst the median best-fitting photometric redshift for the same sample is 4.6 with average $1-\sigma$ errors of $^{+0.18}_{-0.35}$.

By making use of the full $P(z)$ distribution estimated by the photometric redshift code as we do in this work (see Section 2.3.2), galaxies with $P(z)$ which span the redshift boundaries will be scattered between and contribute to both adjacent redshift bins between different MC samples (or scattered out of the sample e.g. $z < 3.5$ or $z > 7.5$). Throughout this work, the errors resulting from this photometric redshift uncertainty are incorporated in the analysis and errors presented.

To compare the low-redshift interloper fractions and the robustness of our photometric redshift selection, we also run the SAM mock catalog through a Lyman break selection process. Our Lyman break selection criteria are based on the V_{606} -dropout criteria of Bouwens *et al.* (2012a) and we exclude sources with $S/N > 2$ in any of the bands blue-ward of the dropout bands (U_{CTIO} , U_{VIMOS} and B_{435}). We also require $S/N(i_{775}) > 5.5$, comparable with other Lyman break selections at this redshift, e.g. Giavalisco *et al.* (2004a) and Beckwith *et al.* (2006). However we note that by choosing a stricter optical S/N requirement, the purity of the sample can always be improved at the expense of total sample size. For consistency with other LBG selections, when making the colour cuts, we use the observed magnitudes for detections above $1-\sigma$ and the $1-\sigma$ upper limit below this.

We caution that since the mock photometric catalog in this section is designed to replicate the H_{160} selection of the observational data used in this paper, the detection criteria for our Lyman break sample will differ from those in the literature based solely on the optical (e.g. Bouwens *et al.* 2007). Therefore, the selection efficiencies and low-redshift interloper fractions calculated here represent only the Lyman break technique as applied to the CANDELS data in this paper specifically. As such, we do not

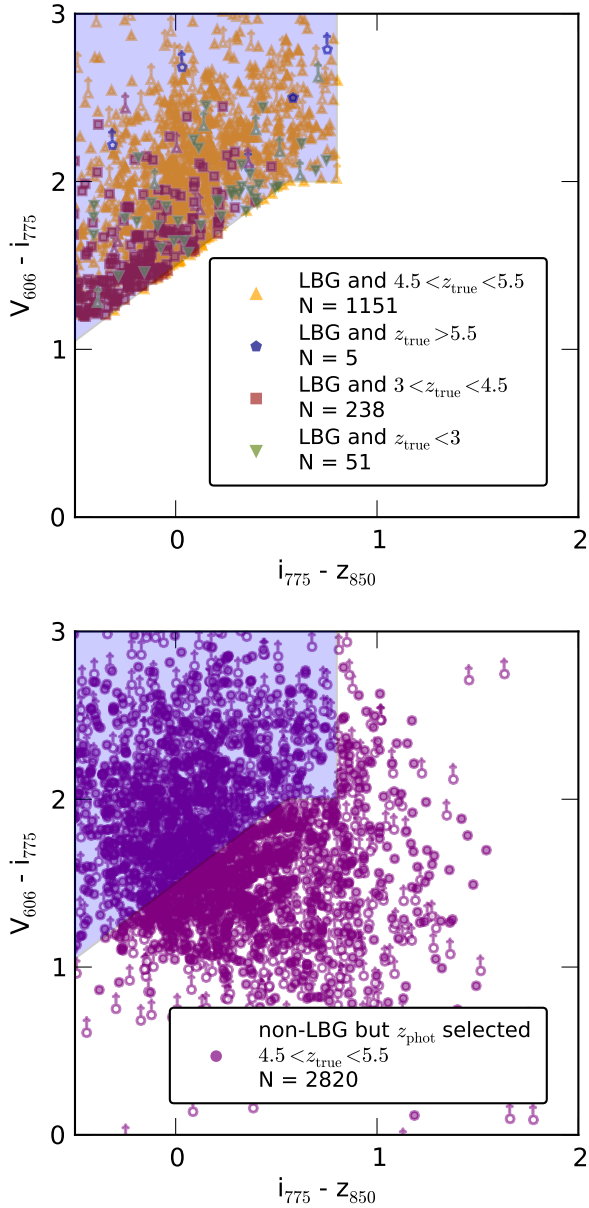


Figure 2.5: *Top:* Observed colours of galaxies from the SAM mock sample which pass the Lyman break selection criteria outlined in the text, separated into bins of intrinsic redshifts. In contrast to previous plots and in keeping with common LBG selection techniques, when calculating colours the measured magnitude is used down to a $S/N = 1$ and the $1-\sigma$ upper limit is used below this. The same is true for colours plotted in the bottom panel. As outlined in the text, the number of $z_{\text{true}} < 3$ galaxies shown represents a quarter of those expected in a fully representative sample. The low-redshift interloper fraction for this sample = $(4*51)/(5 + (51 \times 4) + 238 + 1151) = 0.13$. *Bottom:* Observed colours of galaxies from the SAM mock sample with $4.5 < z_{\text{true}} < 5.5$ which fail the Lyman break selection criteria outlined in the text but are correctly selected as $z \sim 5$ galaxies by the photometric redshift selection used in this work.

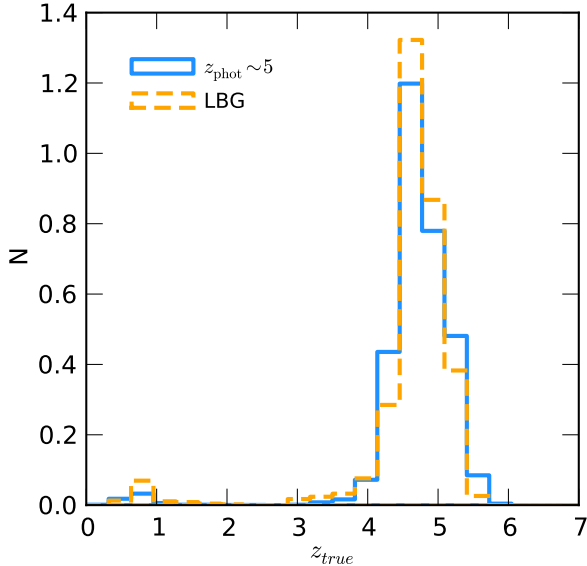


Figure 2.6: Normalised number densities as a function of true redshift for the photometric redshift and Lyman break galaxy samples generated for our SAM mock galaxy catalog.

make any claims regarding the low-redshift interloper fraction of Lyman break selection elsewhere in the literature.

In the upper panel of Figure 2.5, we show the colour distribution and sample sizes for our LBG sample. For this sample, we find a low-redshift interloper fraction comparable to that of the photometric redshift selection. In the lower panel of Figure 2.5, we show galaxies which have true redshifts in the range $4.5 < z_{\text{true}} < 5.5$ and do not satisfy all of the LBG criteria but do pass the photometric redshift selection criteria. Although many of these galaxies have colours outside the LBG colour criteria, photometric redshifts are also able to select galaxies which fail the non-detection or optical S/N criteria. In Figure 2.6, we also compare the intrinsic redshift distribution of the two selection methods. Both the low-redshift contaminants and scatter at bin extremities are clearly visible for both samples.

As a further step to demonstrate the difference in the observed Lyman break colours can be explained solely by photometric scatter, we examine the photometry for a median stack of the 50 candidate $z \sim 5$ galaxies in the CANDELS DEEP region with the lowest $S/N(H_{160})$. Stacking the photometry of a large enough number of sources should cancel out most of the photometric noise, with the resulting images closely reproducing the average intrinsic colours of the input galaxies. In Figure 2.7, we show the initial observed colours (or lower limits) for each of the faint $z \sim 5$ candidates

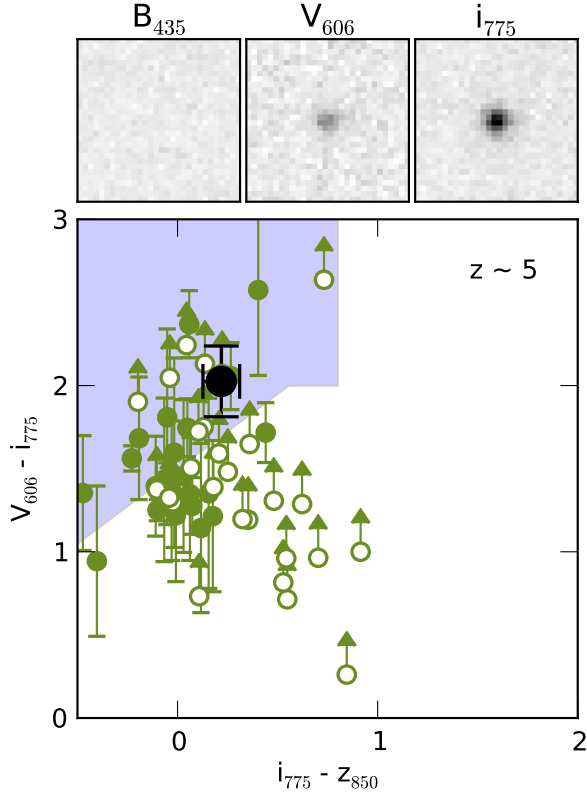


Figure 2.7: Top panels: $1.8 \times 1.8 \text{ arcsec}^2$ postage-stamp images of the median stacked faint sources in the B_{435} , V_{606} and i_{775} filters. Main panel: The observed colours of the individual faint sources are shown by the smaller green circles. Open circles represent sources where the V_{606} has been calculated from the 2σ flux upper limit. The large black circle shows the measured colour for the stacked images.

along with the observed colours of the stacked sources. Although the majority of the input galaxies have colours outside the Lyman break selection, the combined stack has a colour which places it more than $1-\sigma$ inside the desired region and fully consistent with the expected $z \sim 5$ colours.

Also shown in Figure 2.7 are the median stacked images in the 3 filters from below to above the Lyman break. Crucially, for any high-redshift candidate galaxy, the filters at wavelengths lower than the Lyman selection colours should contain zero flux due to the complete absorption by inter-galactic Hydrogen. The median stack in B_{435} for our faint sample contains no trace of flux, with a 2σ upper limit of 29.48 within a $0.6''$ diameter aperture.

While the tests presented in this appendix cannot account for objects with peculiar intrinsic colours (i.e. significantly different from those predicted by semi-analytic or synthetic stellar population models), they demonstrate that the observed colour distribution can be fully accounted for by the photometric scattering of the expected intrinsic

colours. We also conclude that photometric redshift selection can be much less sensitive to photometric scatter than the Lyman break selection criteria for the same redshift range. Furthermore, that it is also able to correctly select high-redshift galaxies which are not identified by the traditional Lyman break selection techniques. In addition, the samples produced by both methods contain similar fractions of low-redshift galaxy contamination when criteria of comparable strictness are applied.

2.5 Mass Fitting

Stellar masses were estimated for our samples using a custom template fitting code with SEDs derived from the synthetic stellar population models of Bruzual & Charlot (2003) (BC03 hereafter). Due to the relatively young ages of the stellar populations (as constrained by the age of the Universe at the redshifts involved), the effects of thermally-pulsating asymptotic giant branch stars (TP-AGB) on resulting SEDs are minimal, e.g. Stark *et al.* (2009). As such, we chose not to use the updated SSP models which incorporate stronger contributions for these effects. The use of Charlot & Bruzual (2007) or Maraston (2005) in place of BC03 should have no result on the conclusions found in this work.

2.5.1 Model SEDs

First, model SEDs are generated from the single stellar populations of Bruzual & Charlot for a range of population ages, metallicities and star-formation histories (SFHs). For our models and throughout this work we use the initial mass function (IMF) of Chabrier (2003). Each template is then normalised such that the total stellar mass equals 1 M_\odot . Nebular emission lines are added to the pure stellar component following the method outlined in Section 2.5.2. Internal dust extinction is applied following the extinction law of Calzetti *et al.* (2000) for the desired range of extinction magnitude A_V .

When applying dust extinction to the nebular emission, we assume the differential dust extinction between stellar and nebular emissions to be fixed as $E(B - V)_{\text{stellar}} = E(B - V)_{\text{nebular}}$, in contrast to the ratio of $E(B - V)_{\text{stellar}} = 0.44E(B - V)_{\text{nebular}}$

derived by Calzetti *et al.* (2000). This choice was motivated by the conflicting evidence for the relative extinction of the two emission sources at $z \sim 2$ (Erb *et al.*, 2006; Förster Schreiber *et al.*, 2009) and that in the context of these models specifically, the assumed differential extinction ratio and escape fraction are degenerate.

The absolute magnitude at 1500 Å (M_{UV}) is measured for each template by integrating the flux within a 100 Å-wide flat bandpass centered on 1500 Å. Similarly, the UV-continuum slope β is calculated by fitting a simple power-law to the integrated template fluxes in the windows described in Calzetti, Kinney & Storchi-Bergmann (1994). The accuracy of this method in calculating β is explored in Finkelstein *et al.* (2012a) and Rogers, McLure & Dunlop (2013).

Next, each model SED is redshifted in the range $0 \leq z < 9$ in steps of $\Delta z = 0.02$, and attenuation by intergalactic neutral hydrogen is applied following the prescription of ?. The resulting grid of SEDs is then integrated through the response filter for each of the observed bands, dimmed by the corresponding distance modulus for each redshift.

2.5.2 Nebular Emission

Nebular emission lines and continuum are added to the templates following a method similar to previous high-redshift fitting methods, e.g. Ono *et al.* (2010); Schaerer & deBarros (2010); McLure *et al.* (2011), Salmon *et al.* (2014). Line strength ratios relative to H β for the major Balmer, Paschen and Brackett recombination lines are taken from ?, with the total H β line luminosity (in erg s $^{-1}$) given by

$$L(\text{H}\beta) = 4.78 \times 10^{-13} (1 - f_{\text{esc}}) N_{\text{LyC}} \quad (2.4)$$

from Krueger, Fritze-vAlvensleben & Loose (1995), where f_{esc} is the continuum escape fraction and the number of Lyman continuum photons N_{LyC} is calculated from each template. The strength of the nebular emission is therefore directly proportional to the number of ionizing photons (Lyman continuum) in the HII region. Since the Lyman continuum emission is dominated by young massive stars, the relative contribution of nebular emission to the total SED is highly dependent on the age of the stellar population and the amount of recent star-formation.

Line ratios for the common metal lines relative to H β were taken from the empirical

measurements of Anders & Alvensleben (2003) for each of the input template metallicities, assuming gas metallicity is equal to the stellar metallicity. Similarly, the nebular continuum emission luminosity is given by

$$L_\nu = \frac{\gamma_\nu^{(total)}}{\alpha_B} (1 - f_{\text{esc}}) N_{\text{LyC}} \quad (2.5)$$

where α_B is the case B recombination coefficient for hydrogen and $\gamma_\nu^{(total)}$ is the continuum emission coefficient given by

$$\gamma_\nu^{(total)} = \gamma_\nu^{(HI)} + \gamma_\nu^{(2q)} + \gamma_\nu^{(HeI)} \frac{n(He^+)}{n(H^+)} + \gamma_\nu^{(HeII)} \frac{n(He^{++})}{n(H^+)}. \quad (2.6)$$

$\gamma_\nu^{(HI)}$, $\gamma_\nu^{(HeI)}$, $\gamma_\nu^{(HeII)}$ and $\gamma_\nu^{(2q)}$ are the continuum emission coefficients for free-free and free-bound emission by Hydrogen, neutral Helium, singly ionized Helium and two-photon emission for Hydrogen respectively, where the values are taken from ?. The coefficients and constants used assume an electron temperature $T = 10^4$ K, electron density $n_e = 10^2$ cm $^{-3}$ and the abundance ratios are set to be $\frac{n(He^+)}{n(H^+)} = 0.1$ and $\frac{n(He^{++})}{n(H^+)} = 0$ (Krueger, Fritze-vAlvensleben & Loose, 1995).

2.5.3 SED Fitting

The fitting of our SEDs to the observed photometry is done using a Bayesian-like approach, whereby the normalised likelihood $\mathcal{L}(M, t)$ for a given stellar mass, M , and template type, t , is given by

$$\mathcal{L}(M, t) = \frac{\exp(-\frac{1}{2}\chi^2(M, t))}{\sum_{t'} \int dM' \exp(-\frac{1}{2}\chi^2(M', t'))}. \quad (2.7)$$

The χ^2 value is given by where $F_j(t)$, F_j^{obs} and σ_j are the template flux, observed flux and the observed flux error in the j th filter respectively. The template types, t , and their associated fluxes correspond to the full range of galaxy parameters (age, star-formation history, dust extinction and metallicity) at the closest matching redshift in the model SED grid.

Because we fit all templates simultaneously, it is therefore straight-forward to calculate the stellar mass probability distribution function (PDF), i.e.

$$P(M) \propto \sum_t \mathcal{L}(M, t), \quad (2.8)$$

marginalised over all other template galaxy properties (assuming a flat prior). Similarly, PDFs for other parameters such as β or M_{UV} ($M_{1500\text{A}}$) can be constructed by summing the likelihoods at a fixed parameter value. Estimating the galaxy parameters in such a way allows us to fully account for errors due to both degeneracies between galaxies properties and errors in the scaling due to the photometric errors.

For our mass fitting, model ages are allowed to vary from 5 Myr to the age of the Universe at a given redshift, dust attenuation is allowed to vary in the range $0 \leq A_V \leq 2$ and metallicities of 0.02, 0.2 and $1 Z_\odot$. Due to the difficulty in obtaining spectroscopy at $z > 3$, the metallicity at high-redshift is not currently well known. Observations of samples at $z \sim 3$ and above (Shapley, Steidel & Pettini, 2003; Maiolino *et al.*, 2008a; Sommariva *et al.*, 2012; Jones, Stark & Ellis, 2012) show that the average metallicity is likely to be mildly sub-solar, however there is a large scatter. Sommariva *et al.* (2012) also find that the gas-phase and stellar metallicities are consistent within errors. As such, we choose to fix the metallicity for the nebular emission equal to stellar metallicity.

The star formation histories follow the exponential form $SFR \propto e^{-t/\tau}$ with characteristic timescales of $\tau = 0.05, 0.25, 0.5, 1, 2.5, 5, 10, -0.25, -0.5, -1, -2.5, -5, -10$ and 1000 (effectively constant SFR) Gyrs. Negative τ values represent exponentially increasing histories. Fitting is done to the templates both with and without the inclusion of nebular emission. When nebular emission is included in the templates, we assume a moderate escape fraction $f_{\text{esc}} = 0.2$, consistent with the observational constraints on reionization and with simulations (Yajima, Choi & Nagamine, 2010; Fernandez & Shull, 2011; Finkelstein *et al.*, 2012a; Robertson *et al.*, 2013).

2.5.4 Star Formation Rates

In order to calculate UV star-formation rates, the rest frame absolute magnitudes (M_{1500}) measured from the SED fitting are first corrected for dust extinction using the Meurer, Heckman & Calzetti (1999) relation

$$A_{1600} = 4.43 + 1.99\beta \quad (2.9)$$

which links the observed UV continuum slope β as measured by the SED fitting code (see Section 2.5.1) and the extinction at 1600Å, A_{1600} . For measured $\beta < -2.23$, where the above relation would imply a negative extinction, the UV extinction was set to 0. UV star-formation rates are calculated using:

$$\text{SFR}(M_\odot \text{yr}^{-1}) = \frac{L_{UV}(\text{erg s}^{-1}\text{Hz}^{-1})}{13.9 \times 10^{27}}, \quad (2.10)$$

where the L_{UV} conversion factor of Madau, Pozzetti & Dickinson (1998) and Kennicutt (1998) corrected to the Chabrier IMF is used (-0.24 dex).

In addition to the the star formation rate obtained by this method ($\text{SFR}_{\text{Madau}}$ hereafter), from our SED fitting code we also obtain the instantaneous star formation rate of the best-fitting template for each galaxy ($\text{SFR}_{\text{Template}}$). We find that the two measures agree well at all SFRs with a median($\log_{10}(\text{SFR}_{\text{Madau}}) - \log_{10}(\text{SFR}_{\text{Template}})$) < 0.1 . With the exception of the few galaxies with the highest $\text{SFR}_{\text{Madau}}$, typically $\text{SFR}_{\text{Madau}} > 100 M_\odot \text{yr}^{-1}$. These galaxies are red, such that the best-fitting template is an older quiescent stellar population. The Meurer relation however assumes an actively star-forming population with high dust extinction.

We also find that the scatter around the 1:1 relation correlates strongly with the age of the best-fitting SED template, such that younger populations have higher $\text{SFR}_{\text{Template}}$. As we will show in the next section however, individual stellar population parameters such as age and dust extinction are very degenerate in SED fits of high-redshift galaxies. Because of these factors, and for consistency with previous works, we primarily use $\text{SFR}_{\text{Madau}}$ throughout this work. The net effect of the differences in the two star-formation rate estimates can be seen in our observed SFR functions in Section 2.5.4.

2.5.5 Image and Detection Simulations

By their nature, high-redshift galaxies are small and extremely faint objects. Lying close to the limiting depth in some (or even all) of the observed filters, noise and systematic effects can have a significant effect on the detection and completeness of high-redshift galaxy samples as well as the accurate estimation of their properties. The completeness of our galaxy sample can be separated into two distinct factors: firstly,

the inclusion of an object in the initial catalog as a function of the detection image depth, and secondly, the selection of an object in a given sample (e.g $z \approx 4$ based on its estimated redshift), which is a function of the overall SED shape and accompanying errors. In this section, we outline a set of detailed simulations undertaken to measure and correct for these effects.

2.5.5.1 Completeness Simulations

The detection completeness across the field was estimated by inserting thousands of mock galaxies into the detection image (H-band) used for the photometry and recovering them with the same SExtractor parameters and method used for the original sample catalog. The synthetic galaxies were first convolved with the CANDELS WFC3 H-band PSF before being placed randomly across the field with appropriate Poisson noise. The resulting image was then run through the same SExtractor procedure as the initial source detection and the process repeated until a total of $\approx 10^5$ input galaxies had been recovered across the entire field.

Galaxy sizes were drawn from a log-normal distribution of mean = $0.15''$ and $\sigma = 0.075$, motivated by existing observations of the size evolution of Lyman break galaxies (Ferguson *et al.*, 2004; Oesch *et al.*, 2010; Grazian *et al.*, 2011; Huang *et al.*, 2013) whilst the galaxies profiles were drawn from a distribution of Sérsic indices centred around $n = 1.5$ in the range $0.5 \leq n \leq 4.0$. Although the precise distribution of morphological profiles for high-redshift galaxies is not well known, studies of lower redshift analogues and stacked samples of LBGs suggests that they are predominantly disk-like ($n < 2$) (Ravindranath *et al.*, 2006; Hathi *et al.*, 2007). Our chosen distribution reflects this, with $\sim 80\%$ of input galaxies with $n \leq 2$.

Figure 2.8 shows the resulting completeness curves for each of the image regions. In Guo *et al.* (2013), the H_{160} 50% completeness limit is estimated using the differential number density to be 25.9, 26.6 and 28.1 for the WIDE, DEEP+ERS and UDF regions respectively. When compared to the results of a set of detection simulations similar to those undertaken in our work, Guo *et al.* (2013) find a good agreement between the two estimates. For the UDF and DEEP+ERS regions, our 50% completeness limits are in good agreement with those of Guo *et al.* (2013). However, in the WIDE region we

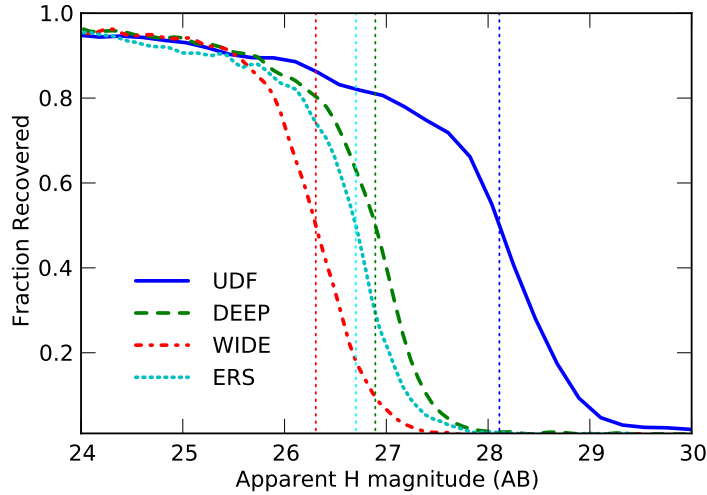


Figure 2.8: Completeness as a function of H_{160} magnitude for each region of the GOODS South field. The vertical dashed lines show the magnitude at which the recovery fraction equals 0.5 for each region of the field.

find a 50% completeness limit ≈ 0.5 mag deeper for our input galaxy population.

Grazian *et al.* (2011) demonstrated the significant effect that sizes and morphologies can have on the completeness simulations of high-redshift galaxies. Differences due to the distribution of sizes and slightly differing galaxy profiles used are to be expected. For all regions, the effects of confusion and blending with nearby sources results in a small fraction of input galaxies which are not recovered by the photometry, even at brighter magnitudes.

2.5.5.2 Sample Selection

To estimate the selection functions for each of the redshift bins, a mock photometry catalog of high-redshift galaxies was created and put through the same photometric redshift and sample selection criteria as our real sample. This catalog was constructed by first creating a sample of SEDs drawn randomly from the template sets used for fitting (both with and without nebular emission) with a distribution of β centred at ≈ -1.8 to -2 , but extending out to $\beta > 1$. Redshifts were allowed to vary in the range $2.5 < z < 9$ and the templates were scaled to H_{160} band magnitudes in the range $22 < H_{160} < 30$, with the corresponding magnitudes in the other filters determined by the shape of each SED.

We produced a catalog in this way, rather than using the mock photometry of semi ana-

lytic models as used in Appendix 2.4 in order to allow the inclusion of nebular emission in subsequent tests on the stellar mass fitting and ensure good number statistics across all input magnitudes.

In order to assign photometric errors to the mock photometry (or non-observations where appropriate), each simulated galaxy was assigned a position in the field drawn from the same set of input coordinates as used in the completeness simulations. Photometric errors were then assigned to each photometric band based on the observed flux errors of objects in the original catalog, specific to the region in which it resides (e.g. CANDELS Deep). The flux values for each SED were then perturbed by a gaussian of width equal to the photometric error.

This process does not precisely mirror the method used to produce the observed photometry as it does not include the source extraction for each band individually. However, the resulting catalog is a very close approximation with a catalog of SEDs that have realistic photometric errors and filter coverage across the field, e.g. Y_{098} observations in the ERS region alone.

To measure the selection efficiency for our high-redshift samples, 100 simulated Monte Carlo samples were created from the template based mock galaxy catalog (as described in this section) using the method outlined in Section 2.3.1. From these samples, we measured the fraction of simulated galaxies which pass the selection criteria for any of the high-redshift samples as a function of input redshift and magnitude.

Figure 2.9 shows the measured selection efficiencies for the deepest region of the field, the UDF. The selection probabilities (as indicated by the colour scale) do not include the effects of completeness as measured in Section 2.5.5.1, therefore the lower probabilities measured at faint magnitude are a result of photometric redshift errors due to poor constraints from faint photometry.

For $z \sim 4$ and 5, where the semi-analytic mock catalog used in Appendix 2.4 has good number statistics across a wide magnitude range, we reproduce the selection function in the same manner as above and find that the shape of the resulting selection functions are unchanged. We are therefore confident that the photometric selection of our samples is robust to variations in the exact shape of the input SEDs and the limiting factor in selection is the photometric noise.

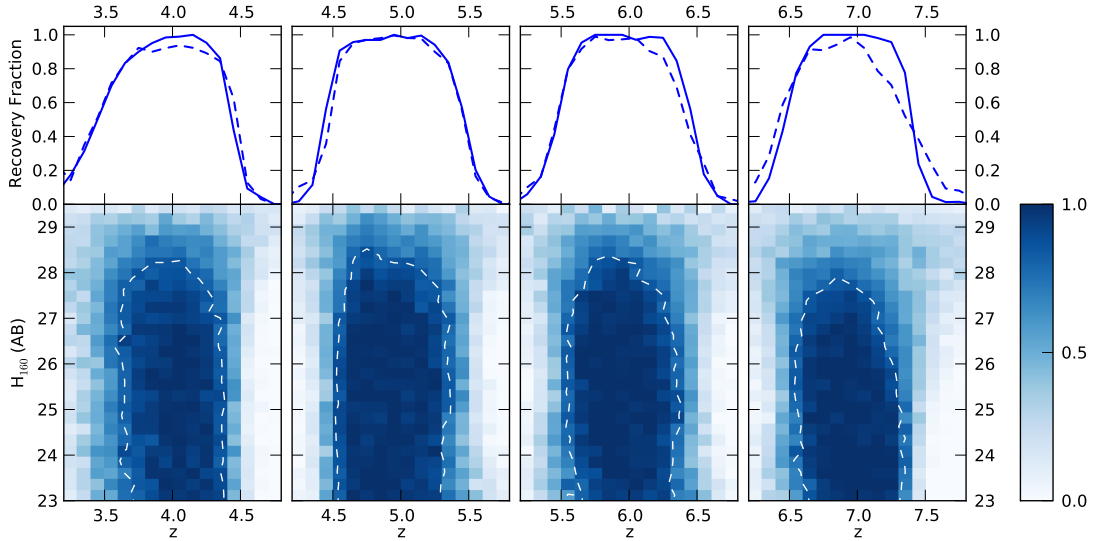


Figure 2.9: Example selection efficiencies for the Ultra Deep Field region of the CANDELS field. The colour scale represents the fraction of input galaxies which pass the $P(z)$ criteria for a given redshift bin as a function of input redshift and apparent magnitude. The dashed white line in the lower sections of the figure shows the 80% contour in the fraction of recovered galaxies. The upper panels show the recovery fraction as a function of redshift at a fixed input magnitude, $H_{160} = 25$ (continuous) and $H_{160} = 27$ (dashed).

2.5.5.3 Uncertainties in measuring galaxy parameters

The ability of SED fitting codes to recover the properties of dropout galaxies was well explored by Lee *et al.* (2010) who found that stellar mass was the most reliably measured parameter (in comparison to star formation rate and age) and the most robust to assumptions in star-formation history. However this analysis was limited to input and fitted SED models which did not include the effects of nebular emission. The degeneracies in measuring age, dust extinction and star-formation histories from SED fitting have also been well examined e.g. Schaerer & deBarros (2010). Despite these degeneracies, it has been shown that one can reliably measure the UV continuum slope, β (Finkelstein *et al.*, 2012b; Rogers, McLure & Dunlop, 2013). Given assumptions about the age and metallicity, i.e. the underlying intrinsic β , it is then possible to estimate the dust extinction using observations of β .

For the $\sim 10^5$ galaxies in our simulated catalog which pass the selection criteria, we ran them through the SED fitting code using the same fitting parameters as for our observed data. From these results we are able to test how well the input stellar masses are recovered for our simulated galaxies. In addition, we can also test the accuracy in recovering the other properties of the input stellar populations.

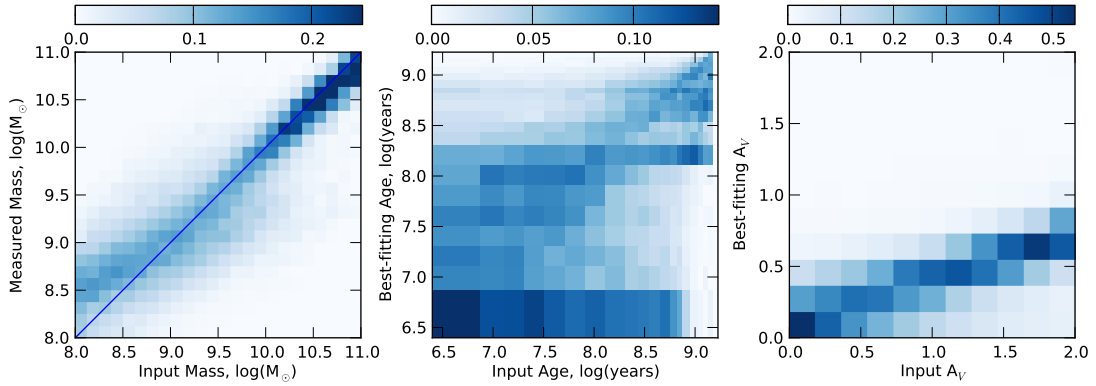


Figure 2.10: 2D histograms showing the recovered SED parameters for a set of input SEDs incorporating nebular emission when fitted with nebular emission. The values for the age (centre) and dust (right) are those corresponding to the single best-fitting model whilst the measured mass (left) is taken as $\int M P(M) dM$ for the mass likelihood distribution marginalised over all other parameters. Each histogram is normalised by the number of input galaxies in each bin and the colour scale corresponds to the fraction of input galaxies at the observed mass (/age/dust extinction).

Figure 2.10 illustrates how well the SED code is able to recover the stellar masses, ages and dust extinction. As expected, stellar mass is the most robust of the parameters with age and dust extinction showing a very large scatter and bias due to the degeneracy in fitting. Despite these degeneracies in the single best-fitting templates, when calculating the marginalised β over all template likelihoods the resulting estimate of β is un-biased and well constrained. We show the estimated accuracy of our β measurements from these simulations in Appendix 2.8.

For input galaxies with masses $\approx 10^9 M_{\odot}$, the $\text{median}(\log_{10}(M_{\text{out}}) - \log_{10}(M_{\text{in}})) = 0.02$, with a standard deviation of 0.4 when input SEDs including nebular emission are fitted with comparable templates. For input masses $\approx 10^{8.5} M_{\odot}$ and below, both the bias (+0.22 dex at $\approx 10^{8.5} M_{\odot}$) and scatter increase. When mock galaxies with pure stellar SEDs are fitted with pure stellar templates, both the scatter and bias are reduced at all mass ranges. The increased bias and scatter for galaxies with nebular emission is a result of confusion between an older stellar population with a 4000Å break and a young star-forming galaxy with strong nebular emission (Schaerer & deBarros, 2009; Curtis-Lake *et al.*, 2013).

Finally, we find that the recovered value for M_{UV} is extremely robust across the full dynamic range of our data, with a scatter of < 0.2 dex and negligible bias across all redshift out to the limits of our completeness as shown in Figure 2.11. From these simulations, we determine that M_{UV} is robust to $M_{UV} \approx -17$ at $z \approx 4$, reducing to -18

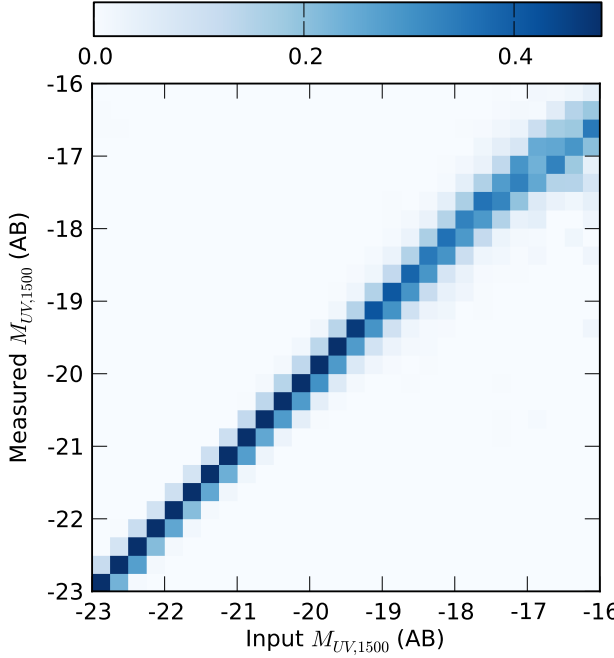


Figure 2.11: Comparison of the recovered versus input M_{UV} for the full mock galaxy sample. As in Figure 2.10, the histogram is normalised by the number of input galaxies in each bin and the colour scale corresponds to the fraction of input galaxies at the observed M_{UV} .

at $z \approx 7$.

2.6 Results

2.6.1 The $1/V_{\max}$ estimator

To compute our luminosity and mass functions we use an extension of the $1/V_{\max}$ method of Schmidt (1968), treating each of our high-redshift samples as a ‘‘coherent’’ sample comprised of the individual GOODS South regions with corresponding depths as outlined by Avni & Bahcall (1980); Eales (1993); Ilbert *et al.* (2005). The maximum comoving volume in which a galaxy can be observed and remain in the sample is given by

$$V_{\max,i} = \sum_k^{N_{\text{regions}}} \int_{z_{1,k}}^{z_{2,k}} \frac{dV}{dz} dz d\Omega_k \quad (2.11)$$

where the sum, k , is over each of the sub-regions in the field with their corresponding solid angle, $d\Omega_k$, integration limits $z_{1,k}$, $z_{2,k}$ and dV/dz is the comoving volume element in Mpc^3 at redshift z . The integration limits are given by $z_{1,k} = z_{\min}$ and $z_{2,k} = \min \{z_{\max}, z(z_j, m_j, m_{\max,k})\}$ where z_{\min} and z_{\max} are the lower and upper

boundaries respectively for the given redshift bin, e.g. $z_{min} = 4.5$ and $z_{max} = 5.5$ for the $z \approx 5$ sample. The function, $z(z_j, m_j, m_{max,k})$, returns the maximum redshift at which an object of apparent magnitude m_j , observed redshift z_j , could still be observed given the magnitude limit $m_{max,k}$ of the region.

The mass (or luminosity) function ϕ_k for discrete bins of mass (/magnitude) k is then:

$$\phi_k dM = \sum_i^{N_{gal}} \frac{w_i}{V_{\max,i}} W(M_k - M_i), \quad (2.12)$$

where the weighting term, w_i , incorporates corrections for incompleteness and the selection function of the redshift bin as calculated in Section 2.5.5. The window function W is defined as

$$W(x) = \begin{cases} 1 & \text{if } -dM/2 \leq x < dM/2 \\ 0 & \text{otherwise} \end{cases} \quad (2.13)$$

and N_{gal} is the number of galaxies in the sample.

To incorporate the large error in the stellar masses, where the mass likelihood function for an individual galaxy can span a range much larger than the desired bin widths, we make amendments to Equation 2.12, such that the mass function evaluated for the mass bin $M_1 < M_k < M_2$ is given by

$$\phi(M) dM = \sum_i^{N_{gal}} \frac{w_i}{V_{\max,i}} \int_{M_1}^{M_2} P_i(M) dM \quad (2.14)$$

where $P_i(M)$ is the probability of galaxy i having stellar mass, M , as calculated from the SED fitting at the fixed redshift for that specific Monte Carlo sample.

2.6.2 UV Luminosity functions

As a more robust observable (relative to the stellar mass, Section 2.5.5) with many previous observations, the rest-frame UV luminosity function provides a useful comparison for the method and completeness corrections used in this paper. To ensure that the shapes of our observed mass functions are not affected by biases in our $1/V_{\max}$ or completeness correction methods we reproduce the luminosity function (LF) for each

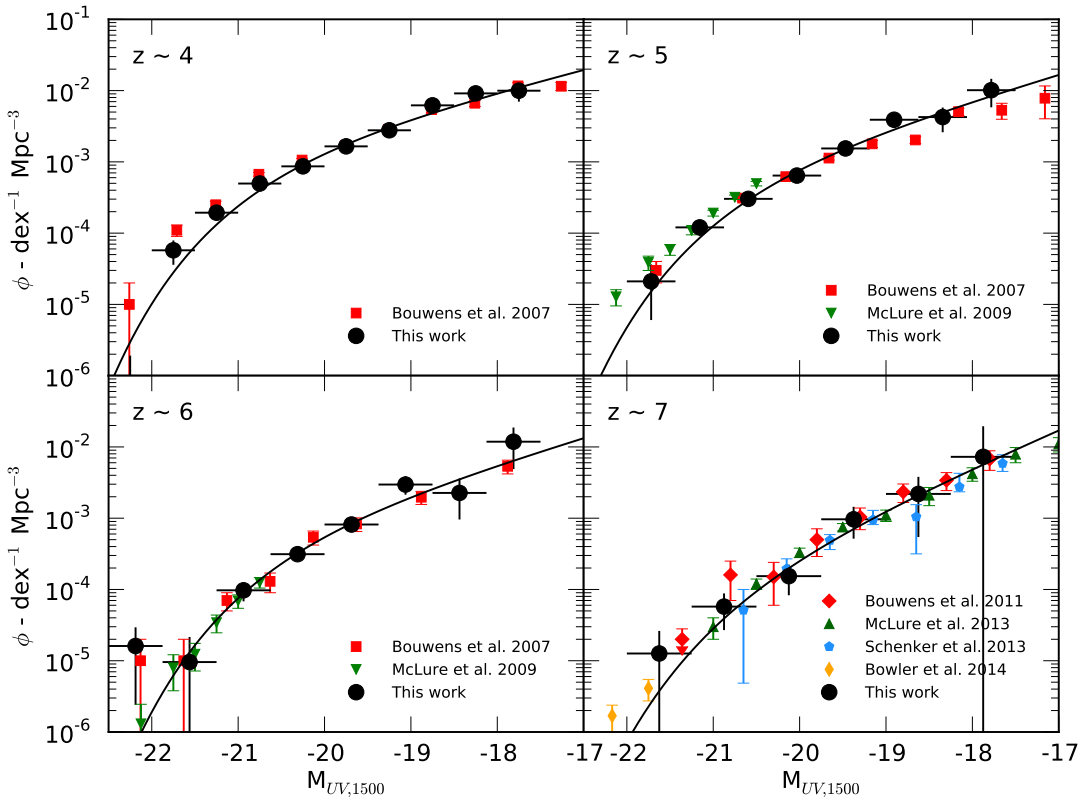


Figure 2.12: A comparison of our $1/V_{\max}$ luminosity function estimates with those in the literature. We show the results of Bouwens *et al.* (2007) at $z \approx 4, 5 \& 6$ (red squares) derived from deep HST observations as well as the ground-based estimates of the bright end of the $z \approx 5$ and 6 luminosity functions by McLure *et al.* (2009)(green downward triangles). For the $z \approx 7$ LF, we show the estimate of Bouwens *et al.* (2011b) as well as the recent results of McLure *et al.* (2013) and Schenker *et al.* (2013b) which make use of the deeper UDF12 observations (Koekemoer *et al.*, 2013) to probe fainter M_{UV} than we are able to.

of our redshift bins, which we can compare to previous work. Figure 2.12 shows the discretized luminosity functions calculated using the method outlined in Equation 2.12. In comparison with previous measurements of the luminosity function at high-redshift we find overall a very good agreement in the general shape of the luminosity functions for our $1/V_{\max}$ data points.

The data points for this work were also fit through χ^2 -minimisation with the Schechter (1976) parameterization

$$\phi(M) = \phi^* \frac{\log(10)}{2.5} 10^{-0.4(M-M^*)(\alpha+1)} \exp(-10^{-0.4(M-M^*)}), \quad (2.15)$$

where M is the rest-frame UV magnitude and ϕ^* , α and M^* are the normalisation, faint-end slope and characteristic UV magnitude as standard. The resulting best-fitting parameters shown in Table 2.3 along with the corresponding parameters from the se-

lected literature observations shown in Figure 2.12. At all redshifts, the faint end slope is steep ($\alpha < -1.6$) and shows a tentative steepening towards $z \sim 7$. However, the poor constraints on the faint end slope towards the highest redshifts make it difficult to comment on any evolution of the slope that might occur over this redshift range. At all redshifts, the slope is consistent with a fixed slope of $\alpha = -1.7$ (Bouwens *et al.*, 2011b).

At $z \sim 4$, our measured M_{UV}^* of -20.47 ± 0.21 is significantly fainter than that observed by Bouwens *et al.* (2007), who find $M_{UV}^* = -21.06 \pm 0.1$. We find a closer agreement with the fainter M_{UV}^* observed by Huang *et al.* (2013) of $-20.60^{+0.13}_{-0.17}$. At the bright end of the $z \sim 4$ luminosity function, our fit is strongly affected by the very low number density at $M_{UV} \approx -22.25$. Given the relatively small area of our survey field, the numbers of galaxies contributing to the brightest bins is very small ($\approx 1 - 3$). Differences in the measured (or assumed) redshift when calculating the rest-frame magnitude can therefore have a large effect, e.g. the difference in the distance modulus between $z = 3.5$ and $z = 4$ is ≈ 0.35 . As such, the characteristic cut-off in our Schechter function parameterisation is not well constrained, and the discrepancy is not significant.

2.6.3 Observed mass-to-light ratios

In the past, the relationship between a galaxy's stellar mass and its UV luminosity (or $\log_{10}(M_*)$ and M_{UV}) has been used as both a diagnostic of galaxy formation histories (Stark *et al.*, 2009) and as a tool for estimating the galaxy stellar mass function at high-redshift (González *et al.*, 2011). In a scenario where galaxies form their stars continuously, a strong $\log_{10}(M_*)$ - M_{UV} relation should form, whereas more stochastic bursty star formation modes could result in a relation with wider scatter and a weaker trend.

Using the stellar mass and M_{UV} probability distributions produced by our SED fitting code, we plot the observed mass-to-light ratios for each of our redshift bins in Figure 2.13. For a given Monte Carlo sample (see Section 2.3.1), the 2D $\log_{10}(M_*)$ - M_{UV} probability distributions of each galaxy in the redshift bin are summed. The resulting PDFs of each sample are then summed to create a combined PDF in each redshift bin

Table 2.3: Schechter (1976) function parameters for χ^2 fits to the $1/V_{\max}$ luminosity functions. The quoted errors represent the $1-\sigma$ limits, but do not account for systematic error due to cosmic variance.

Redshift	M_{UV}^*	α	$\phi^* (10^{-3} \text{ Mpc}^{-3})$
$z \sim 4$			
This work	-20.47 ± 0.21	-1.77 ± 0.18	$1.90^{+0.79}_{-0.65}$
Bouwens et al. 2007	-21.06 ± 0.1	-1.76 ± 0.05	1.1 ± 0.2
$z \sim 5$			
This work	$-20.47^{+0.26}$	$-1.90^{+0.21}_{-0.16}$	$1.07^{+0.59}_{-0.14}$
Bouwens et al. 2007	-20.69 ± 0.13	-1.66 ± 0.09	$0.9^{+0.3}_{-0.2}$
McLure et al. 2009	-20.73 ± 0.11	-1.66 ± 0.06	0.94 ± 0.19
Bouwens et al. 2012	-20.60 ± 0.23	-1.79 ± 0.12	$1.4^{+0.7}_{-0.5}$
$z \sim 6$			
This work	$-20.31^{+0.84}_{-1.59}$	$-1.91^{+0.91}_{-0.59}$	$0.95^{+2.21}_{-0.91}$
Bouwens et al. 2007	-20.29 ± 0.19	-1.77 ± 0.16	$1.2^{+0.6}_{-0.4}$
McLure et al. 2009	-20.04 ± 0.12	-1.71 ± 0.11	1.8 ± 0.5
Bouwens et al. 2012	-20.37 ± 0.3	-1.73 ± 0.20	$1.4^{+1.1}_{-0.6}$
$z \sim 7$			
This work	$-20.47^{+1.43}$	$-2.31^{+1.31}_{-0.19}$	$0.29^{+2.87}_{-0.13}$
Bouwens et al. 2011	-20.14 ± 0.26	$-2.01^{+0.14}_{-0.15}$	$0.86^{+0.70}_{-0.39}$
McLure et al. 2013	$-19.90^{+0.23}_{-0.28}$	$-1.9^{+0.14}_{-0.15}$	$1.10^{+0.56}_{-0.45}$
Schenker et al. 2013	$-20.14^{+0.36}_{-0.48}$	$-1.87^{+0.18}_{-0.17}$	$0.64^{+0.56}_{-0.27}$

across all Monte Carlo samples. Finally, we normalise such that the probability at each value of M_{UV} integrates to unity. By plotting the observed $\log_{10}(M_*) - M_{UV}$ in this way, we take into account the full redshift and fitting errors. However, this representation is still subject to the effects of small number statistics for the brightest and faintest galaxies.

As such, we also show the biweight mean $\log_{10}(M_*)$ for bins of M_{UV} within the range of reliably measurable M_{UV} . For $z \geq 5$, each bin contains a minimum of 5 galaxies by design, whilst for the $z \sim 4$ sample each bin contains a minimum of 10 galaxies. To these means, we fit linear functions with intercept $\log_{10} M_{*(M_{UV} = -19.5)}$ and slope $d \log_{10} M_*/dM_{UV}$. The best-fit values for each redshift sample are shown in Table 2.4 for stellar mass estimates both with and without the inclusion of nebular emission.

As has been seen in many previous studies, we observe a clear ‘main-sequence’ trend of increasing mass with increasing UV luminosity, and a large scatter about this trend. For the bright galaxies ($M_{UV} < -21$), our results agree well with those of Stark *et al.* (2009), González *et al.* (2011) and Lee *et al.* (2012). Over the full range of UV luminosity, we find a shallower trend with M_{UV} than González *et al.* (2011). We also find

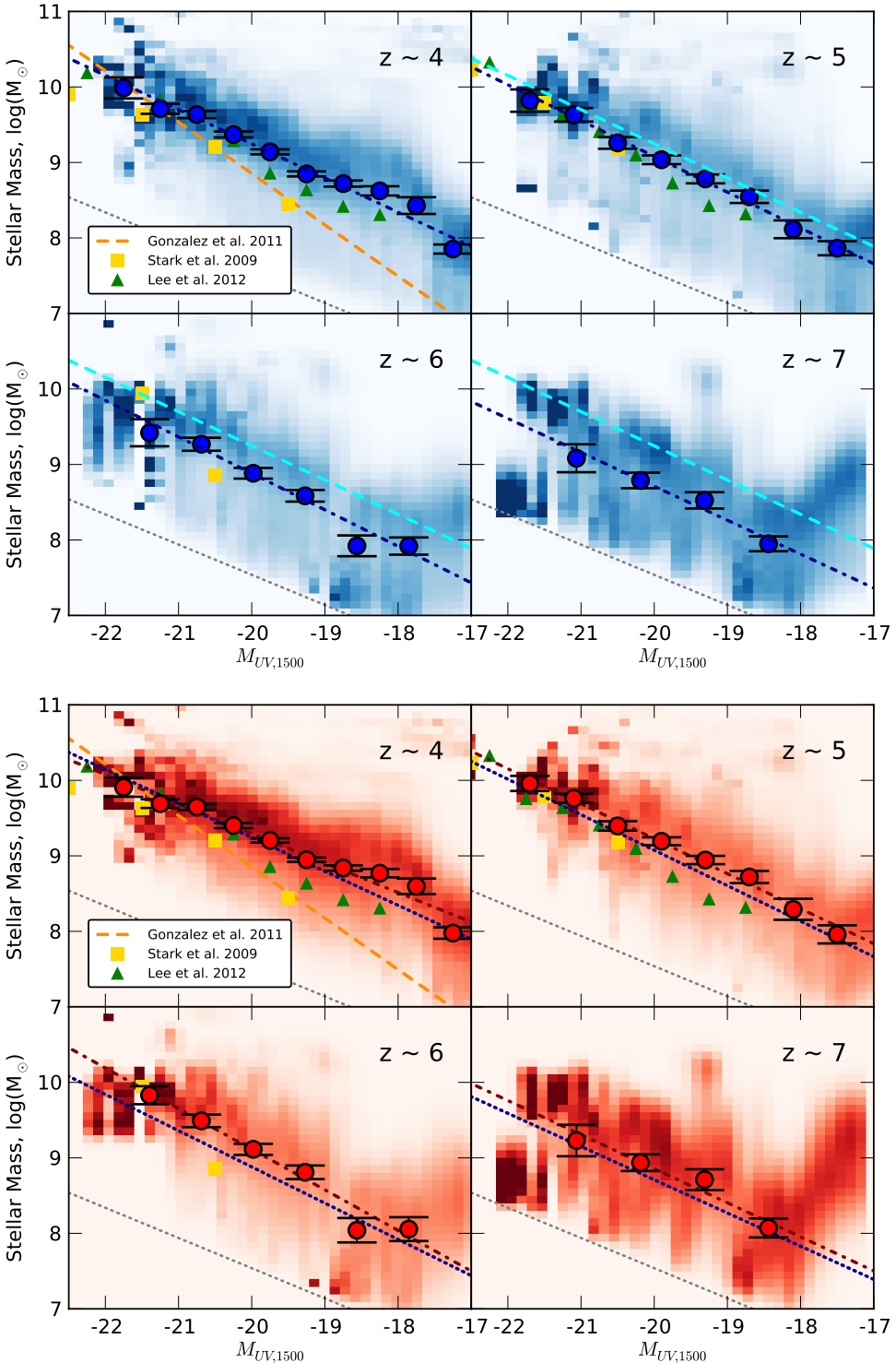


Figure 2.13: Top: Probability distribution of the mass-to-light ratios observed when nebular emission is included in the fitting, stacked across all of the Monte Carlo samples. The values are normalised such that the probability at each value of M_{UV} integrates to unity. The blue dot-dashed line represents the average of the best-fitting line to robust means in each of the Monte Carlo samples, with the corresponding average means and their errors shown by the blue circles. The $z \sim 4$ relation is shown for reference at high-redshifts (cyan dotted line). Bottom: The corresponding probability distributions, bi-weight means and best-fitting relation (red dot-dashed line) when nebular emission is excluded from the SED fitting. The blue dotted line shows the best-fitting relation from the top panel (including nebular emission) for each sample. In both panels, the orange dashed line shows the mass-to-light ratio observed by González *et al.* (2011), measured for their $z \approx 4$ sample and applied across all bins. The green triangles and yellow squares show the average stellar mass in M_{UV} bins as calculated by Lee *et al.* (2012) and Stark *et al.* (2009) respectively, all stellar masses have been converted to the same Chabrier IMF. The grey dotted line represents the template in our SED fitting parameters with the lowest mass to light ratio.

that this trend evolves in normalisation between redshift $z \sim 4$ and 7.

The change in the observed normalisation of the $\log_{10}(M_*)$ - M_{UV} relation with redshift as a consequence of the inclusion of nebular emission has been examined before (Shim *et al.*, 2011; deBarros, Schaefer & Stark, 2012; Schenker *et al.*, 2013a; Stark *et al.*, 2013). However, we find that although this trend for decreasing normalisation with redshift is enhanced when nebular emission is included in the mass fitting, the trend still exists when fitting with pure stellar templates (see Table 2.4).

In Figure 2.13, the effect of including nebular emission in the stellar mass estimate can be seen clearly in the bottom panel. At all redshifts, the average stellar mass for a given M_{UV} is lower when nebular emission is included. Salmon *et al.* (2014) also consider the effects of adding nebular emission lines to the SED models for galaxies in the same redshift range, and they find similar changes to the derived masses as we do here. In addition, the median stellar masses they observe for UV faint galaxies are higher than those of González *et al.* (2011) and Lee *et al.* (2012), consistent with our observations.

Because in our SED fitting on the mass, we restrict the age of the templates to be less than the age of the universe at that redshift, the range of $\log_{10}(M_*)$ - M_{UV} ratios available in the fitting does vary with redshift, i.e. a galaxy at $z = 7$ can never have as old as a stellar population as a galaxy at $z = 4$. If the fits to galaxies at $z \sim 6$ and 7 were being restricted by this upper limit, the limits set by the template set could create an artificial evolution in the scaling of the $\log_{10}(M_*)$ - M_{UV} relation with redshift. However, examining the best-fitting SED parameters across all of the Monte Carlo samples, we find that at all redshifts and M_{UV} values the highest best-fitting mass lies well below the maximum mass allowed by the template set. From this, we conclude that the observed scaling is therefore physical and not a result of systematics in our analysis.

The slopes of our fitted $\log_{10}(M_*)$ - M_{UV} relations are all close to that of a constant mass to light ratio ($M_* \propto -0.4 M_{UV}$) across the full range in luminosity. This implies there is no strong evolution of the mass to light ratio with luminosity. Lee *et al.* (2012) suggested the source of the change in their observed $\log_{10}(M_*)$ - M_{UV} ratio could be due to a luminosity dependent extinction, a result which had also been implied by the

Table 2.4: The best-fitting slope and intercepts of the $\log_{10}(M_*) - M_{UV}$ mass-to-light relation, averaged across all Monte Carlo samples. At $z \sim 4$ and 5, we also show in parentheses the best-fitting values when the fits are restricted to only the brightest galaxies ($M_{UV} < -19.5$).

z	$\log_{10} M_*(M_{UV} = -19.5)$	$d\log_{10} M_*/dM_{UV}$
<i>With Nebular Em.</i>		
4	9.02 ± 0.02 (9.06 ± 0.05)	-0.45 ± 0.02 (-0.42 ± 0.06)
5	8.84 ± 0.04 (8.85 ± 0.12)	-0.47 ± 0.04 (-0.46 ± 0.11)
6	8.64 ± 0.06	-0.48 ± 0.07
7	8.49 ± 0.09	-0.44 ± 0.12
<i>Without Nebular Em.</i>		
4	9.10 ± 0.02 (9.12 ± 0.05)	-0.39 ± 0.02 (-0.37 ± 0.05)
5	9.00 ± 0.04 (9.00 ± 0.09)	-0.46 ± 0.04 (-0.45 ± 0.08)
6	8.84 ± 0.07	-0.54 ± 0.07
7	8.63 ± 0.11	-0.45 ± 0.13

evolution of β with M_{UV} seen by Bouwens *et al.* (2012a). Subsequent observations by Dunlop *et al.* (2011) and Finkelstein *et al.* (2012b) have found no obvious luminosity dependence. However, recent studies by Bouwens *et al.* (2014a) and (Rogers *et al.*, 2014) with greatly increased sample sizes and greater dynamic range confirm an unambiguous colour-magnitude relation. While measurements of β for our sample do not exhibit strong evidence for such a strong luminosity dependent extinction at any redshift (see Appendix 2.8), our sample does not contain a statistically significant number of the brightest and faintest galaxies to rule out such evolution given the large scatter and error on β .

Due to the increasing uncertainty in stellar mass measurements for galaxies below $10^9 M_\odot$, the average mass-to-light ratios for the faintest galaxies could become increasingly biased towards fainter UV luminosities. As such, we cannot rule out a change in the $\log_{10}(M_*) - M_{UV}$ slope at faint luminosities like that inferred by Lee *et al.* (2012). To better constrain the average mass-to-light ratio for faint galaxies, detailed stacking across the full SEDs as a function of M_{UV} would be required. Restricting our analysis to the brightest galaxies ($M_{UV} < -19.5$) at $z \sim 4$ and 5 where the potential biases are minimised, we find no significant change in the fitted $\log_{10}(M_*) - M_{UV}$ slopes.

In hydrodynamical simulations of galaxies at $z > 5$, Wilkins *et al.* (2013) found a re-

lationship between the intrinsic L_{1500} (excluding dust absorption) and M/L_{1500} which is roughly constant. This relationship is also seen to evolve, with the normalisation decreasing with increasing redshift. When dust extinction was applied to the intrinsic model luminosities based on the β observations of Bouwens *et al.* (2012a), the observed $\log_{10}(M_*) - M_{UV}$ exhibited a much stronger correlation comparable to that observed by González *et al.* (2011).

2.6.4 Stellar mass functions at high-redshift

Following the method outlined in Section 2.6.1, specifically using the $1/V_{\max}$ method in Equation 2.14, we construct the stellar mass function for each of our high-redshift samples. The resulting stellar mass functions are shown in Figure 2.14. Our data points and errors take into account the stellar mass errors, Poisson errors and the errors due to the photometric redshift uncertainty.

The black lines in Figure 2.14 show the best-fitting Schechter (1976) functions from χ^2 minimisation to the the $1/V_{\max}$ data above our chosen mass completeness limits (black points). We perform two sets of fits to our data. Firstly, we allow all 3 parameters to vary (solid line, $z \sim 4, 5$ and 6) and secondly, we fix the characteristic mass such that $M^* = M_{z \sim 4}^*$ (dashed line, $z \sim 5, 6$ and 7). The parameters for these fits are shown in Table ??.

Because there exists such a large scatter in the observed mass-to-light ratios for the high-redshift galaxies, accurately estimating the mass completeness limit is non-trivial. For a given mass near the completeness limit, there could exist a significant contribution from galaxies below the luminosity limit proportional to how large the actual intrinsic scatter is. However, it is not known how much of the observed scatter is due to photometric error (and therefore photometric redshift estimates and parameters from SED fitting) and how much is intrinsic. Rather than trying to correct for galaxies lost through incompleteness down to the lowest observed masses, we instead restrict our analysis to masses unaffected by this scatter. We calculate this mass limit by taking the 95% mass percentile of the observed galaxies within 0.5 dex of our H_{160} magnitude limit, finding it to be $\approx 10^{8.5} M_\odot$. Under the reasonable assumption that the intrinsic scatter in the mass-to-light ratio does not rapidly increase below our detection limit, the

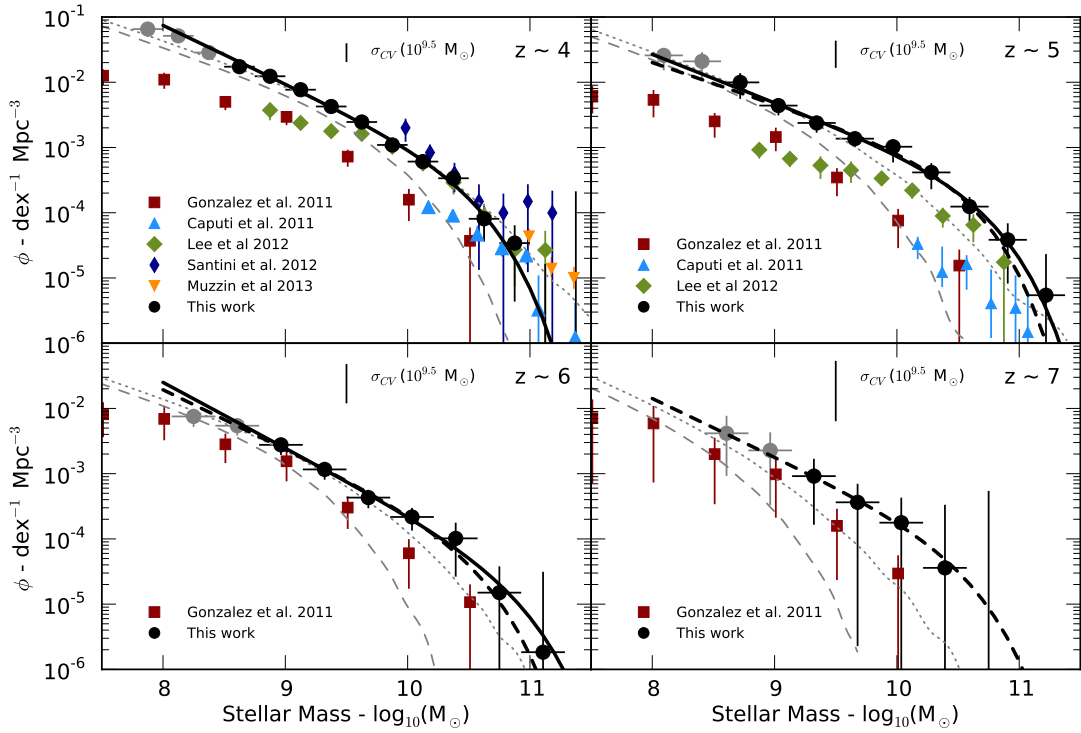


Figure 2.14: The $1/V_{\max}$ stellar mass functions for the high-redshift samples. Error bars take into account random Poisson noise as well as the scatter between the Monte Carlo samples due to photometric redshift uncertainty. The black circles show the mass bins included in the χ^2 fitting to the Schechter (1976) functions based on the stellar mass limits described in the text. The dashed and dotted lines show the stellar mass functions calculated by applying the best-fitting mass-to-light ratio (including nebular emission, see Table 2.4) to the literature luminosity functions at each redshift with a scatter of 0.2 (dashed) and 0.5 (dotted) dex. For the $z \sim 4$ bin, the Schechter fit of Bouwens *et al.* (2007) was used, whilst at $z \sim 5$ & 6 and $z \sim 7$ the fits of Bouwens *et al.* (2012b) and McLure *et al.* (2013) respectively were used to generate the luminosity distribution. We also show using the error bars at the top of each panel the cosmic variance expected for galaxies of stellar mass $\approx 10^{9.5} M_\odot$, as predicted by the method outlined in Moster *et al.* (2011).

contribution to masses above $\approx 10^{8.5}$ from galaxies below the limit will be negligible.

Additionally, as shown in Section 2.5.5, the accuracy of stellar mass estimates begins to deteriorate at lower masses with an increasing bias which could lead to biased slopes. Taking these factors into account, the limits chosen when fitting the stellar mass functions were $\log_{10}(M_\odot) = 8.55, 8.85, 8.85$ and 9.15 for $z \sim 4, 5, 6$ and 7 respectively.

Inspecting the observed mass functions in Figure 2.14, it can be seen that the exact limit should have little effect on the measured slope within reasonable bounds at $z \sim 4 - 6$. Choosing limits ± 0.5 dex would not affect our conclusion that the mass function is steep.

Due to the small sample size at $z \sim 7$ and the large errors in estimating the stellar mass

Table 2.5: Schechter (1976) function parameters for χ^2 fits to the $1/V_{\max}$ mass functions. For the $z \sim 5, 6$ and 7 samples, we do two fits, one in which $\log_{10}(M^*)$ is allowed to vary, and one in which it is fixed to the best-fitting value for the $z \sim 4$ sample. The quoted errors represent the $1-\sigma$ errors from fitting marginalised over the remaining parameters but do not account for any systematic errors due to cosmic variance.

z	$\log_{10}(M^*)$	α	$\phi^* (10^{-4} \text{ Mpc}^{-3})$
4	$10.51^{+0.36}_{-0.32}$	$-1.89^{+0.15}_{-0.13}$	$1.89^{+3.46}_{-1.32}$
5	$10.68^{+0.98}_{-0.46}$	$-1.74^{+0.41}_{-0.29}$	$1.24^{+4.77}_{-1.19}$
	10.51	$-1.64^{+0.15}_{-0.17}$	$2.21^{+0.80}_{-0.76}$
6	$10.87^{+1.13}_{-1.06}$	$-2.00^{+0.57}_{-0.40}$	$0.14^{+4.11}_{-0.14}$
	10.51	$-1.90^{+0.27}_{-0.31}$	$0.46^{+0.36}_{-0.26}$
7	10.51	$-1.89^{+1.39}_{-0.61}$	$0.36^{+3.01}_{-0.35}$

(from both the photometric redshift and fitting errors), the mass function is very poorly constrained. The range of acceptable values for α cover an extremely wide range but are consistent with the slope of $\alpha \approx -1.9$ found for the lower redshift bins and the slope of the corresponding luminosity function. Over the redshift range examined by this work, the errors in α are too large to infer any evolution in slope with redshift.

As we are observing only a single field, we are unable to estimate the cosmic variance in the number densities by comparing the field to field variation. We use the updated QuickCV code of Moster *et al.* (2011) (see also Newman & Davis 2002) to estimate the cosmic variance as a function of mass in each of our redshift bins for a survey field with the dimensions of CANDELS GOODS South. In Figure 2.14 we show the estimated error on the counts for galaxies of mass $\approx 10^{9.5} M_\odot$. For stellar mass $\approx 10^{10} M_\odot$ and above, the cosmic variance predicted by this method exceeds $> 100\%$ at $z \sim 6$ and 7. However, due to the lack of constraints on the galaxy bias at high-redshift, there is a large uncertainty on these estimates. When compared to the field-to-field variation observed by Lee *et al.* (2012), our estimates represent a conservative assessment of the likely cosmic variance. With the full CANDELS imaging now complete, future analysis incorporating all five of the separate survey fields should allow much more robust measures on the true cosmic variance at high-redshift.

In addition to the $1/V_{\max}$ estimates, we also estimate the stellar mass function using a method analogous to that of González *et al.* (2011). For each sample, 10^6 UV magni-

tudes in the range $-23 < M_{UV,1500} < -13$ are drawn from the observed luminosity functions from the literature at each redshift (Bouwens *et al.*, 2007, 2012b; McLure *et al.*, 2013). The $M_{UV,1500}$ are then converted to stellar masses using the best-fitting relations from Table 2.4 for each redshift sample and a scatter of 0.2 (dashed lines) or 0.5 dex (dotted lines).

At $z \sim 4$, the $1/V_{\max}$ data shows a good agreement with the mass functions generated by this method. At higher redshifts however, luminosity based mass functions increasingly underpredict the number density at high masses for the same fixed scatter in the $\log_{10}(M_*)$ - M_{UV} relation. To increase the number densities at high mass to match those observed, either a more strongly evolving $\log_{10}(M_*)$ - M_{UV} relation (in direct disagreement with that observed) or a significantly greater scatter in the intrinsic $\log_{10}(M_*)$ - M_{UV} ratios is required.

2.6.4.1 Comparison with the literature

Caputi *et al.* (2011) studied the massive end of the stellar mass function at $3 \leq z \leq 5$ over a wide area in the UKIDSS Ultra Deep Survey (UDS), using photometric redshifts for a sample of $4.5\mu m$ selected galaxies. Our observed number densities show a broad agreement at $z \sim 4$ ($3.5 \leq z < 4.25$ for Caputi *et al.*) for $\log_{10} M_* > 10.5$ but are significantly higher at lower masses. The same is also true across all masses at $z > 4$ ($4.25 \leq z < 5.0$). However for both redshift samples, Caputi *et al.* (2011) find a very steep low-mass slope when parameterised with a Schechter (1976) fit, in agreement with our results. At the massive end of the $z \sim 4$ galaxy SMF, our results agree with those of Muzzin *et al.* (2013) over the limited mass range covered by both works.

Covering a significantly smaller area than those observations but probing to lower masses are the $1/V_{\max}$ observations of Santini *et al.* (2012). We find a good agreement with these results, however due to the small number statistics at the high mass end of the SMF, the errors on both sets of observations are large.

Another measurement of the stellar mass function at $z \sim 4 - 5$ is that of Lee *et al.* (2012), who study the SMF for a Lyman break selected sample in the GOODS North and South fields (Giavalisco *et al.*, 2004b). At $z \sim 4$, for stellar masses $\log_{10} M_* > 9.5$

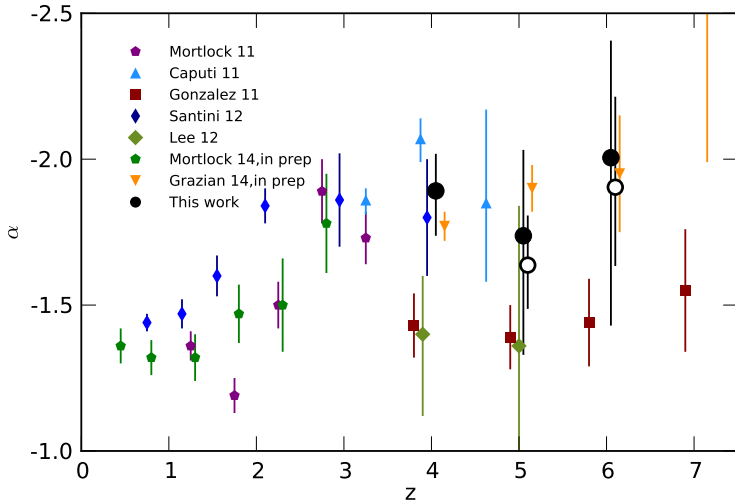


Figure 2.15: Evolution of the low-mass slope from $z = 0$ to $z \sim 7$. We show the best-fitting α for both the freely varying (filled circles) and fixed M_* (empty circles) fits. The fits for $z \sim 7$ were excluded due to the poor constraints. We show results from the recent literature for the stellar mass function at lower redshifts and at $z > 3$. Shown are the α quoted for single Schechter (1976) fits to the observed data where α has been left as a free parameter in the fitting or has been estimated analytically (González *et al.*, 2011).

the two results are in excellent agreement. Below this mass range, the significantly steeper low-mass slope measured in this work results in a higher number densities than those found by Lee *et al.* (2012). At $z \sim 5$, we again find higher number densities although there is some agreement at the highest masses.

González *et al.* (2011) provides the only previous observation that covers the full redshift range and is also the only work which does not construct the galaxy stellar mass function from the galaxy masses directly. Instead, González *et al.* (2011) measure the $\log_{10}(M_*)-M_{UV}$ relation at $z \sim 4$ (testing for consistency with the smaller samples at $z \sim 5$ and 6). The mass-to-light ratio is then applied to the observed UV luminosity function for each redshift bin, allowing the estimation of the SMF to lower masses and higher redshift than would otherwise have been possible. Because their $\log_{10}(M_*)-M_{UV}$ ratio is fixed at all redshifts, there is less evolution in the SMF than we observe. The slope of the $\log_{10}(M_*)-M_{UV}$ relation observed by González *et al.* (2011) also results in a low-mass slope which is shallow across all redshift bins.

When placed in the context of low-redshift observations of the stellar mass function, our results at $z \sim 4$ are a continuation of the trend of increasing α with redshift. In Figure 2.15, we show recent observations of the low-mass slope of the SMF from $z = 0$ out to $z \sim 7$. We include only results where α has been fitted as a free parameter and

the values of α quoted are from the single Schechter function parameterisations of the SMF.

At $z \sim 3$, there is a broad agreement in the estimations of the low-mass slope at $\alpha \approx -1.8$. By $z \sim 4$, there is a much larger disagreement between observed value spread across $\alpha \sim -2$ to -1.4 . It is important to note that the observations with a shallower low-mass slope, González *et al.* (2011); Lee *et al.* (2012), are those with galaxies selected using the Lyman break technique colour cuts and source detection using optical bands (typically z_{850}). In contrast, those with steep slopes, Caputi *et al.* (2011), Santini *et al.* (2012) and this work, use photometric redshift selection as well as near- or mid-infrared band for source detection. The best-fitting α of this work are also in good agreement with the maximum-likelihood estimates of Grazian et al. *in prep*, an independent analysis of the combined CANDELS GOODS and UDS (UKIDSS Ultra Deep Survey) fields.

2.6.4.2 Comparison with theory

In Figure 2.16, we compare our measurements of the observed stellar mass function with the predictions of both smoothed particle hydrodynamic (SPH) and semi-analytic models. The SPH predictions are taken from the hybrid energy/momentum-driven wind (ezw) model of Davé *et al.* (2013). We also show the predictions of three semi-analytic models (SAM), from Croton *et al.* (2006), Lu *et al.* (2011) and Somerville *et al.* (2008) (see also Somerville *et al.* 2012). Details of the three models and an in-depth comparison between the model predictions across all redshifts can be found in Lu *et al.* (2013). The number densities have been renormalised to the comoving volume of the cosmology used throughout our paper ($H_0 = 70 \text{ kms}^{-1}\text{Mpc}^{-1}$, $\Omega_0 = 0.3$ and $\Omega_\Lambda = 0.7$). Analysis is restricted to $z \leq 6$ due to limits on the robustness of simulations at higher redshifts from the numerical resolution of the simulations.

Inspecting the mass functions at $z \sim 4$, there is excellent agreement between the observations and the models of Davé *et al.* (2013), Croton *et al.* (2006) and to a lesser extent Lu *et al.* (2011). Of the three SAM predictions, Somerville *et al.* (2008) shows the least agreement at $z \sim 4$ due to the over-abundance of higher mass galaxies. However, at higher redshifts the reverse is true, with the Somerville *et al.* (2008) models

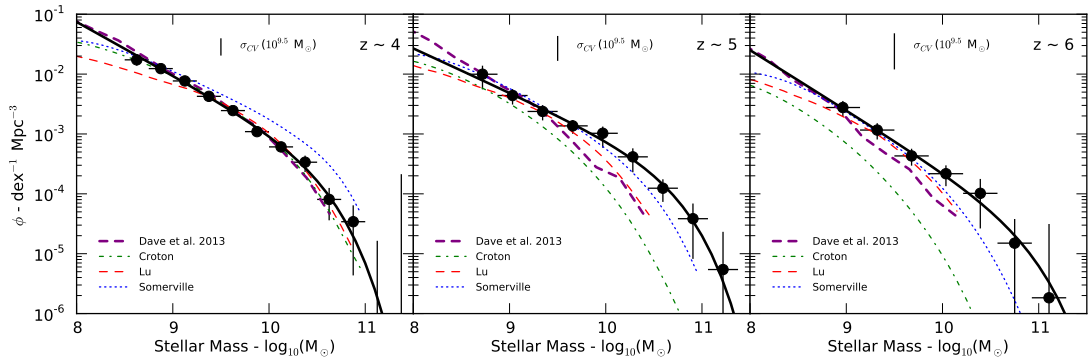


Figure 2.16: Comparison of the observed galaxy stellar mass functions in this work with theoretical model predictions at $z \sim 4, 5$ and 6 . We show the semi-analytic models of Croton *et al.* (2006), Somerville *et al.* (2008) and Lu *et al.* (2011), using the error convolved stellar mass functions as outlined in Lu *et al.* (2013). The dashed purple line shows the results from the hydrodynamical simulations of Davé *et al.* (2013).

providing the best match to the observed $z \sim 5$ and 6 mass functions.

Of the four model predictions presented here, the SPH simulations of Davé *et al.* (2013) exhibit the steepest low-mass slopes and the closest agreement with our observations. The steepening of the low-mass slope in this model (from $z \sim 0$ to $z > 3$) is a result of decreasing contribution from wind recycling at high-redshifts. The resulting feedback at high-redshift has a smaller mass dependence than other models. This can be seen when compared to the SAM model of Lu *et al.* (2011) which has feedback with a much stronger mass dependence owing to increasingly strong (or efficient) feedback in low-mass haloes.

The SPH predictions, along with those of the Lu *et al.* (2011) SAM, most closely match the evolution in the overall normalisation of the number densities across the observed redshift range. The other semi-analytic models undergo a much stronger evolution in the number density of the most massive galaxies. It is important to take into account the fact that all 3 of the semi-analytic models are tuned to match only the $z = 0$ stellar mass function. The range of acceptable parameters at $z = 0$ found by Lu *et al.* (2011) results in a broad distribution of predicted stellar mass functions at high-redshift. Nevertheless, it is clear that our new observations of the high-redshift SMF can be used to further constrain our best models of galaxy evolution.

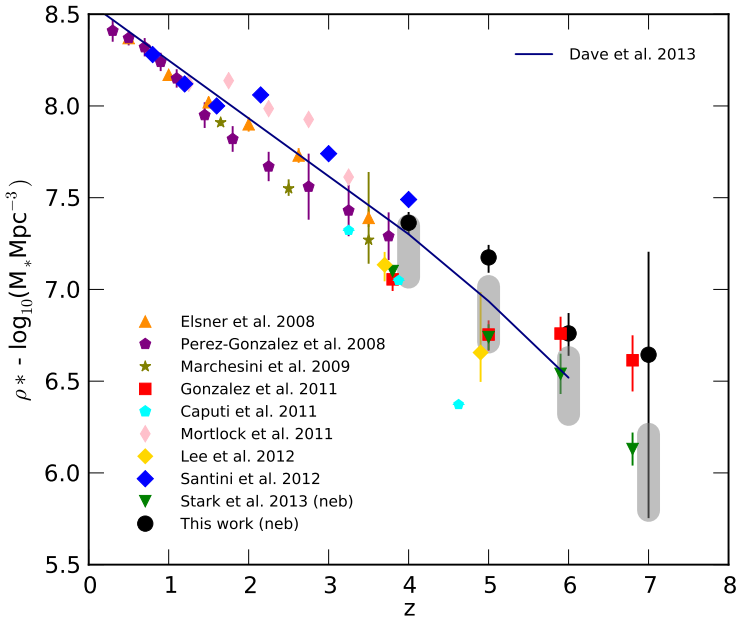


Figure 2.17: Observed stellar mass densities (for $M > 10^8 M_\odot$). All literature values have been converted to a Chabrier/Kroupa IMF as appropriate. The grey regions at $z \sim 4, 5, 6$ and 7 show the range in stellar mass density traced by the luminosity function-based mass functions described in Section 2.6.4, the lower and upper limits correspond to 0.2 and 0.5 dex of scatter in the applied mass-to-light ratios respectively.

Table 2.6: Stellar mass densities integrated from the Schechter parameters in Table ?? for $M > 10^8 M_\odot$. Error bars correspond to the minimum and maximum stellar mass densities within the 1σ contours of the mass function fits.

z	$\rho_*(\log_{10} M_\odot \text{ Mpc}^{-3})$
4	7.36 ± 0.06
5	$7.17^{+0.07}_{-0.08}$
6	$6.76^{+0.11}_{-0.12}$
7	$6.64^{+0.56}_{-0.89}$

2.6.5 Stellar Mass Density

We compute the total stellar mass density (SMD) by integrating the fitted Schechter (1976) function from $M_* = 10^8$ to $10^{13} M_\odot$, with 1σ errors estimated from the minimum and maximum SMD within the 1σ contours for the fit parameters (see Table ??).

For the $z \sim 5, 6$ and 7 samples, we use the best-fitting parameters with $M^* = M_{z \sim 4}^*$. The results are shown in Figure 2.17 as the solid black points. We also show results from the literature across all redshift ranges, converted to the same cosmology and IMF (Chabrier/Kroupa).

Our observations show the continuation of the rapid decline in global stellar mass density towards high-redshifts, falling by a factor of between ~ 4 and 40 in the ~ 1

Gyr between $z \sim 4$ and 7. This rate of stellar mass growth observed is higher than observed by González *et al.* (2011) over the same time period but comparable to that found by Stark *et al.* (2013) when the large uncertainty in the $z \sim 7$ SMD is taken into account.

At $z \sim 4$, our results lie within the range of past stellar mass density measurements at this redshift. Although larger than the results of the Lyman break selected samples (González *et al.*, 2011; Lee *et al.*, 2012; Stark *et al.*, 2013), we find a SMD less than that of Santini *et al.* (2012) and comparable to that of some of the other photometric redshift selected samples (Pérez González *et al.*, 2008; Marchesini *et al.*, 2009). As could be inferred from the stellar mass functions, the stellar mass densities of Davé *et al.* (2013) underpredict observed SMD at $z \sim 5$ and $z \sim 6$ but shows a good agreement at $z \sim 4$. Similarly, the range of densities covered by our luminosity based mass functions (grey regions) are significantly lower than the directly observed SMD in all redshift bins apart from $z \sim 4$.

2.6.6 Star Formation Rates

2.6.6.1 Specific star formation rates

Earlier observations of the sSFR evolution at $z > 3$, with mass estimates excluding the effects of nebular emission, showed the sSFR at a fixed mass remained roughly constant at ~ 2 Gyr $^{-1}$ with increasing redshift (Stark *et al.*, 2009; González *et al.*, 2010; Bouwens *et al.*, 2012a). Such a plateau in the sSFR evolution was at odds with most plausible models of galaxy evolution (as explored by Weinmann, Neistein & Dekel 2011).

However, it has since been shown that the inclusion of nebular emission in stellar mass estimates at high-redshift has a significant effect on the redshift evolution of the specific star formation rate (sSFR) (Schaerer & deBarros, 2009, 2010; Stark *et al.*, 2013; González *et al.*, 2014). By lowering the measured mass for a fixed star formation rate, the inclusion of nebular emission results in a higher sSFR proportional to the strength (or effect on the estimated stellar mass) of the emission lines.

In Figure 2.18, we show our results for the sSFR (when using $\text{SFR}_{\text{Madau}}$) in a stellar

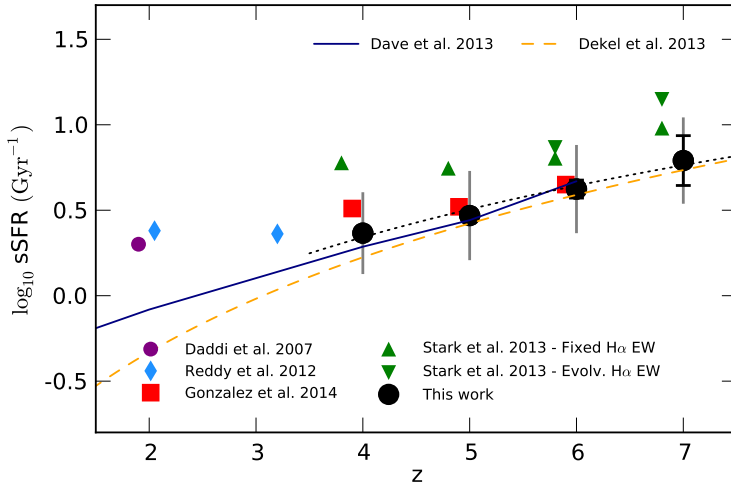


Figure 2.18: Biweight mean specific star-formation rates (sSFR) and error on the mean for galaxies of mass $M_* = 5 \times 10^9 M_\odot$ as a function of redshift for this work (black circles). We find the scatter in sSFR, taken as the biweight scale of the distributions (grey error bars), to be ≈ 0.25 dex across all redshifts. The dashed yellow line shows the evolution of the specific accretion rate, $\propto (1+z)^{2.5}$, as outlined in Dekel *et al.* (2013). The blue line shows the sSFR predicted by Davé *et al.* (2013), the model which most closely matches the observed stellar mass function (see Section 2.6.4.2). The black dotted line shows the best-fitting power law to the results in this paper from $z \sim 4$ to 7 ($\propto (1+z)^{2.06 \pm 0.25}$).

mass bin at $\log_{10}(M/M_\odot) = 9.7 \pm 0.3$ alongside previous observations at $z > 2$. We find an average sSFR of 2.32 ± 0.08 , 2.94 ± 0.20 , 4.21 ± 0.54 and 6.2 ± 2.5 Gyr $^{-1}$ for $z \sim 4, 5, 6$ and 7 respectively. Our observations show a clear trend in increasing sSFR with redshift in the redshift range $4 \leq z \leq 7$. The observed sSFR are in very good agreement with those of González *et al.* (2014) but are systematically lower than those of Stark *et al.* (2013) over the same redshift range. However, as noted in Stark *et al.* (2013), the introduction of 0.5 dex of intrinsic scatter to the $\log_{10}M_* - M_{UV}$ used when estimating their sSFR would result in a reduction of $2.8 \times$ at $z \sim 4$. Such a large intrinsic scatter would be fully consistent with the $\log_{10}M_* - M_{UV}$ relations and stellar mass functions observed in this paper. Taking this offset into account, the increasing consensus in the observed sSFR at high redshift is encouraging.

Performing a simple best fit to our observed sSFR across all four redshift bins, weighted to the measured scatter, gives $sSFR \propto (1+z)^{2.06 \pm 0.25}$ (black dotted line). This trend is much more consistent with theoretical expectations of the sSFR evolution than a plateau at ~ 2 Gyr $^{-1}$, whereby the increased accretion of cold gas onto haloes results in higher specific star formation rates in the early universe. This can be seen in the evolution of the specific accretion rate (Neistein & Dekel, 2007; Dekel *et al.*, 2013), $\propto (1+z)^{2.5}$, shown as the orange dashed line in Figure 2.18. Also shown in Figure 2.18

are the simulation predictions of Davé *et al.* (2013) which are in good agreement with both our observations and the the specific accretion rate model at $z > 3$.

Although we find a strong agreement with the zero-th order specific accretion rate model over the redshift range covered in this work, such a comparison should not be made in isolation from the previous observations of the sSFR at lower redshift. By $z \sim 4$ and below, the observed sSFR begins to diverge strongly from that predicted by the specific accretion rate and the SPH models of Davé *et al.* (2013). If we include the additional observations of Daddi *et al.* (2007) and Reddy *et al.* (2012) we find a best-fit of $\text{sSFR} \propto (1+z)^{0.9 \pm 0.2}$, consistent with that found by González *et al.* (2014). However, restricting the power law fit previously calculated to only $z \sim 5, 6$ and 7 , we find $\text{sSFR} \propto (1+z)^{2.6 \pm 0.4}$.

Given the large degeneracies and assumptions inherent to the stellar mass and star formation estimates (deBarros, Schaefer & Stark, 2012; Schaefer, deBarros & Sklias, 2013), there may still be significant systematic errors in the observed sSFR at high redshift. For example, Salmon *et al.* (2014) find that the use of an SMC-like extinction curve instead of Calzetti *et al.* (2000) results in systematically lower sSFR for their sample at $z \sim 4$ to $z \sim 6$ using the same CANDELS data as our work. Similarly, the poor constraints on the properties of nebular emission and the escape fraction at high redshift allows for a wide range of plausible scenarios which could affect the measured stellar mass and SFR significantly. This is especially important at $z \sim 6$ and 7 where the impact of nebular emission is strongest (Stark *et al.*, 2013; Smit *et al.*, 2013; González *et al.*, 2014). Although the previous tension between theory and observations at $z > 4$ has been largely resolved, improved constraints on the stellar populations and star formation rates of high-redshift galaxies are still required before robust comparisons can be made.

2.6.6.2 Star formation rate functions and the cosmic star formation rate density

To measure the evolution of the star-formation rate (SFR) density for across our observed redshift bins, we use the previously calculated $1/V_{\max}$ values for each galaxy to construct a SFR function analogous to the mass or luminosity function for the same

data, such that

$$\phi_{SFR,k} d\epsilon = \sum_i^{N_{gal}} \frac{w_i}{V_{max,i}} W(\epsilon_k - \epsilon_i), \quad (2.16)$$

where $\epsilon = \log_{10}(\text{SFR}_{UV})$. The SFR functions for our high-redshift samples are shown in Figure 2.19 for both the dust corrected UV star-formation rates ($\text{SFR}_{\text{Madau}}$) and the SED star-formation rates as outlined in Section 2.5. At low to moderate star-formation rates ($\log_{10}(SFR_{UV}) \leq 1.5$), the two SFR estimates are in good agreement across all redshifts as was seen when the two estimates for individual galaxies were compared.

The SFR function estimates of Smit *et al.* (2012) (converted to the same IMF used in this work) exhibit lower star-formation rates than we observe at all redshifts, with the exception of the $\text{SFR}_{\text{template}}$ based estimate at $z \sim 4$ which shows excellent agreement across the full SFR range. Smit *et al.* (2012) correct the observed UV luminosity functions (Bouwens *et al.*, 2007, 2012b) to intrinsic magnitudes using the same Meurer, Heckman & Calzetti (1999) relation as outlined in Section 2.5. Since the underlying UV luminosity functions for both observations show a good agreement, this discrepancy can be attributed solely to the β values and methodology when correcting extinction. The Bouwens *et al.* (2012a) $M_{UV} - \beta$ relations used to correct for dust extinction in Smit *et al.* (2012) exhibit a stronger UV luminosity dependence as well as a bluer average colour than that observed in our work (see Appendix 2.8).

Integrating the SFR function across a suitable range gives the global SFR density. For consistency with other UV SFR density measurements, the lower bound in the integration of the SFR function was chosen to be $\log_{10}(SFR_{UV}) = -0.47$, equivalent to $0.03L_{z=3}^*$, and the data points were integrated directly in steps. The evolution of the cosmic star formation rate density is shown in Figure 2.20. Alongside our new estimates of the SFR density at high-redshift we show the compilation of observed cosmic SFR from $z = 0$ to $z = 8$ from Behroozi, Wechsler & Conroy (2013) and their fitted functional form to the same data. Our observations show a clear rise in the cosmic SFR over the ~ 1 Gyr between $z \sim 7$ and $z \sim 4$ with an increase of ≈ 0.5 dex over this period.

As expected from the inspection of the SFR functions, the integrated SFR densities predicted by Smit *et al.* (2012) are lower than those observed in this work. The same is true for the cosmic SFR observed by Bouwens *et al.* (2012a) which makes use of the

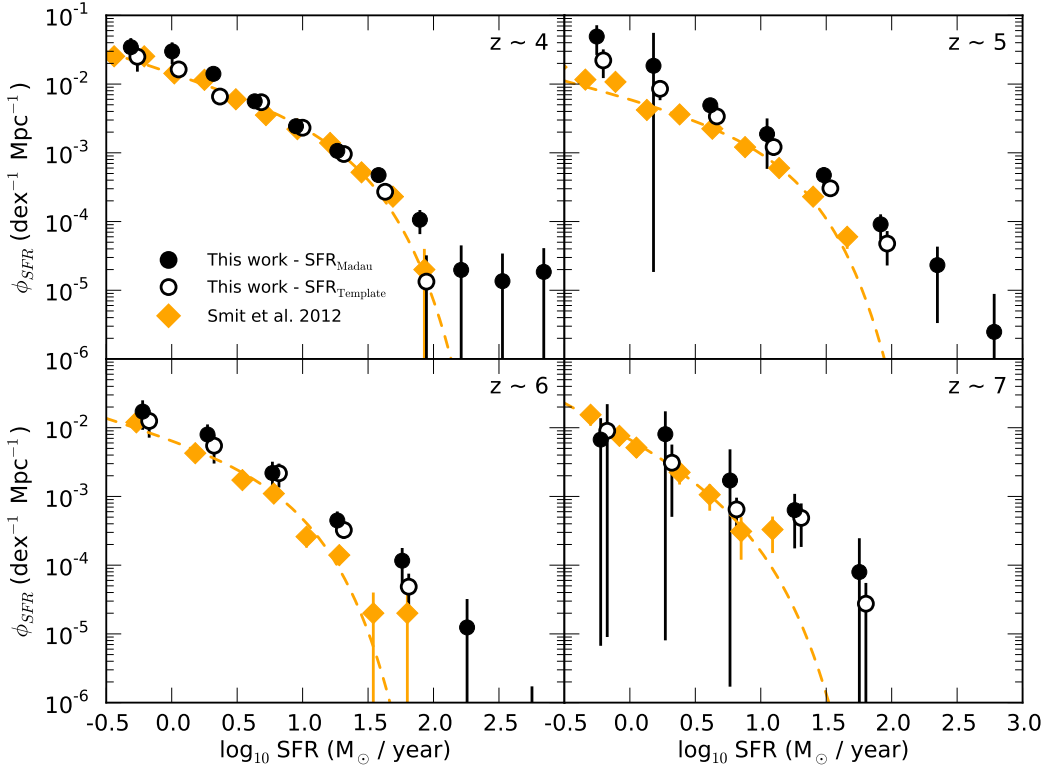


Figure 2.19: Star-formation rate functions calculated using the $1/V_{\max}$ estimator as outlined in Equation 2.16. The filled black circles correspond to star-formation rates estimated from the dust corrected UV luminosity whilst the open black circles correspond to the best-fitting star-formation rate from the SED fitting, see Section 2.5.4. The SFR-functions of Smit *et al.* (2012) converted to a Chabrier IMF are shown by the yellow diamonds.

same $M_{UV} - \beta$ relations. Due to the steep UV luminosity functions, the cosmic SFR is dominated by the faint galaxy population. The difference in dust correction resulting from the redder observed UV continua in this work therefore has a large effect on the observed dust corrected SFR density.

In the recent β observations of Bouwens *et al.* (2014a), the authors find systematically redder β 's than for Bouwens *et al.* (2012a). They find that for a fixed redshift and rest-frame UV luminosity, $\Delta\beta \sim 0.13 - 0.19$ for $z = 4 - 6$ and $\Delta\beta \sim 0.22$ at $z \sim 7$. Following the Meurer, Heckman & Calzetti (1999) relation, we estimate that the corresponding difference in dust corrections would be $\Delta A_{1500} \sim 0.26 - 0.38$ for $z = 4 - 6$ and $\Delta A_{1500} \sim 0.44$ at $z \sim 7$. An increase in the Smit *et al.* (2012) star-formation rates of this magnitude would bring the two dust-corrected UV SFR-function estimates into greater agreement (and hence the corresponding SFR densities). However, such a correction is a simplification, and does not take into account the different $M_{UV} - \beta$ slopes observed and the effects of scatter. We can therefore not make

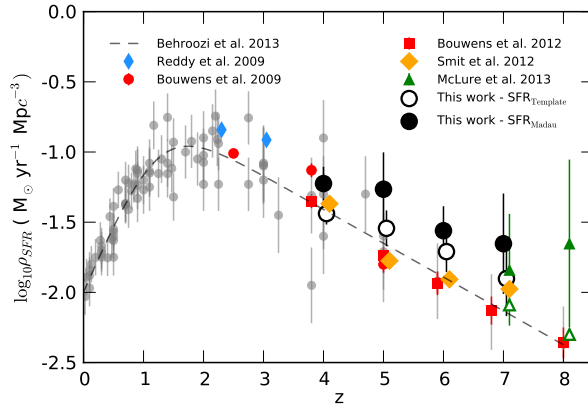


Figure 2.20: Evolution of the SFR density as estimated from the SFR functions in Figure 2.19. The black filled circles show the SFR density calculated by integrating under the observed data directly using SFR_{Madau} . The empty black circles show the corresponding estimates using SFR_{Template} , these points have been offset by $+0.05z$ for clarity. We show the recent compilation of SFR density observations (grey circles) and the fitted functional form from Behroozi, Wechsler & Conroy (2013). Shown separately are the dust-corrected UV SFR estimates of Reddy & Steidel (2009), Bouwens *et al.* (2009), Bouwens *et al.* (2012a), Smit *et al.* (2012) and McLure *et al.* (2013). The Smit *et al.* (2012) values were calculated by integrating the analytic SFR functions presented in their work from $\log_{10}(SFR_{UV}) = -0.47$ and above, in line with the limits used in other observations (see text). For the UV SFR density observations of McLure *et al.* (2013) (open triangles), we apply a dust correction based on the observed β slopes of the same survey as measured by Dunlop *et al.* (2013) (filled triangles). We assume a fixed average extinction (with respect to M_{UV}) consistent with their observations, using $\langle \beta \rangle = -2.1 \pm 0.2$ for $z \sim 7$ and $\langle \beta \rangle = -1.9 \pm 0.3$ for $z \sim 8$.

a fully quantitative comparison of how SFR functions based on the β observations of Bouwens *et al.* (2014a) would compare with those in this work.

Applying a dust correction based on the observations by Dunlop *et al.* (2013) to the uncorrected SFR density observed by McLure *et al.* (2013) (for the same sample and photometry), we find the results are in good agreement with our observations at $z \sim 7$. In Bouwens *et al.* (2014a), the authors claim that the β observations of Dunlop *et al.* (2013) are biased red-ward by $\Delta\beta \sim 0.13$, our estimated dust-corrected SFR-density for McLure *et al.* (2013) could therefore be a factor of $0.26dex$ too high. We note that if we apply a correction to the β 's observed in this work in order to match the observed $M_{UV} - \beta$ relations of Bouwens *et al.* (2014a), our SFR density estimates would be reduced by $\Delta\rho_{SFR} \sim 0.05 - 0.1dex$.

As with our observations of the specific star formation rate, the possible systematic errors resulting from the treatment of dust could have a significant effect on the observed SFR density. The importance of this can be seen in the difference between the UV and SED-fitting SFR functions and their corresponding SFR density estimates. The

rarer red objects selected by our photometric redshift samples can contribute a significant fraction of cosmic SFR density if assumed to be dusty star-forming objects, i.e. β corrected UV star-formation rates. Although the growing availability of spectroscopic data for high redshift galaxies will help reduce the uncertainty in some of these assumptions, the independent SFR observations at $z > 3$ promised by ALMA and LOFAR will be essential for obtaining robust measures of the cosmic SFR in the early universe.

2.7 Summary

In this paper, we make use of the deep data provided by the CANDELS survey of the GOODS South to study the stellar mass growth of galaxies in the first 2 billion years of galaxy evolution. For a photometric redshift selected sample, we present new measurements of the galaxy stellar mass function across the redshift range $z \sim 4$ to 7 along with observations of the UV star formation rate of this sample. Stellar masses for the sample are measured from SED template fitting incorporating the effects of nebular emission, previously shown to have a significant effect on the observed stellar masses at high-redshift.

Using the rest-frame UV magnitudes and UV continuum slopes measured by our SED fitting code, we also calculate dust-corrected star formation rates for our sample. From these we derive specific star formation rates and a measure of the cosmic SFR density as a function of redshift. Our primary conclusions are as follows:

- Our new observations of the stellar mass functions at $z \sim 4$ to $z \sim 7$ exhibit steep low-mass slopes across the whole redshift range. These slopes are significantly steeper than previous observations in this redshift regime and are much closer to those observed in the UV luminosity functions of these same objects and recent observations at lower redshifts.
- The observed stellar mass to UV luminosity ratio of our sample exhibits minimal evolution with luminosity, with close to a constant M/L_{UV} in all redshift bins. The overall normalisation of the $\log_{10}(M_*) - M_{UV}$ undergoes a significant

increase in the scaling of this relation over time.

- From our observations of the stellar mass function, we calculate the stellar mass density at $z \sim 7$ is $6.64_{-0.89}^{+0.58} \log_{10} M_{\odot} \text{Mpc}^{-3}$ rising to 7.36 ± 0.06 at $z \sim 4$ for galaxies $M > 10^8 M_{\odot}$ and a Chabrier IMF.
- At a fixed stellar mass ($M = 5 \times 10^9 M_{\odot}$), the mean specific star formation rate rises with redshift. We find $\text{sSFR} = 2.32 \pm 0.08 \text{ Gyr}^{-1}$ at $z \sim 4$, rising to $6.2 \pm 2.5 \text{ Gyr}^{-1}$ at $z \sim 7$. These results are in good agreement with other estimates of sSFR which incorporate nebular emission in the stellar mass estimates.
- We observe a rapid decline in the cosmic star formation rate at $z > 4$, but find star formation rate densities up to ≈ 0.5 dex higher than those of Bouwens *et al.* (2012a) and Smit *et al.* (2012) at the same redshifts. We conclude that much of this difference can be attributed to the rarest objects with large amounts of inferred dust extinction. Future spectroscopic and long-wavelength observations will be vital in better understanding star-formation rates in this epoch.

Acknowledgements

We thank the anonymous referee for their thorough review and help in greatly improving the paper. This work is based on observations taken by the CANDELS Multi-Cycle Treasury Program with the NASA/ESA HST, which is operated by the Association of Universities for Research in Astronomy, Inc., under NASA contract NAS5-26555. This work is based in part on observations made with the Spitzer Space Telescope, which is operated by the Jet Propulsion Laboratory, California Institute of Technology under a contract with NASA. Support for this work was provided by NASA. AM acknowledges funding via an ERC consolidator grant (PI: McLure). We would also like to acknowledge funding from the Science and Technology Facilities Council (STFC) and the Leverhulme Trust.

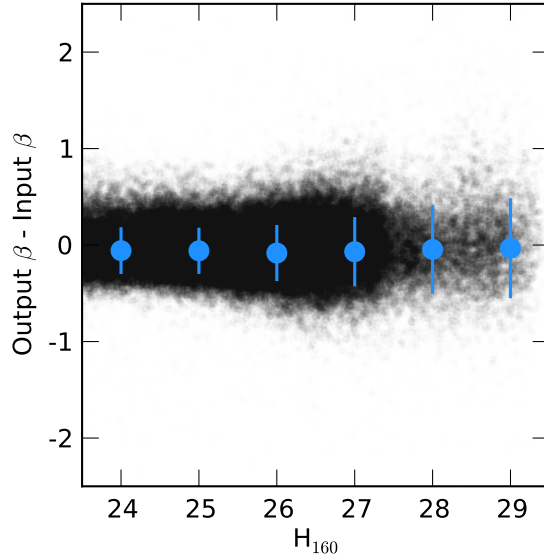


Figure 2.21: Recovered β - input β as a function of apparent H_{160} magnitude. The blue circles show the mean $\beta_{out} - \beta_{in}$ in bins with width = 1 magnitude. The bias ($|\text{median}(\beta_{out} - \beta_{in})|$) is less than 0.1 for all magnitudes, whilst the standard deviation increases from = 0.24 at $H_{160} = 24$ to = 0.44 at $H_{160} = 28$

2.8 Observed UV continuum slopes

As one of the key observables that it is possible to accurately measure for high-redshift galaxies using photometry, the UV continuum slope (β) has been well studied but with initially conflicting results (Dunlop *et al.*, 2011; Wilkins *et al.*, 2011; Bouwens *et al.*, 2012a; Finkelstein *et al.*, 2012a; Rogers, McLure & Dunlop, 2013; Bouwens *et al.*, 2014a). The method used in this work to measure β follows a similar procedure to that outlined in Finkelstein *et al.* (2012a). The relative accuracy of the different methods and the effects of differing sample criteria are explored in depth by Rogers, McLure & Dunlop (2013), however from our simulations (Section 2.5.5) we can test the accuracy of our fitting directly. Figure 2.21 shows the difference between the input and measured β as a function of H_{160} magnitude for all regions of the GOODS-S field combined.

In Rogers, McLure & Dunlop (2013), it was shown that the SED fitting method for measuring β suffers from a red bias when measuring the average slope. This is a result of limits placed on the measured β by the bluest template available in the fitting, artificially clipping the measurement to values above that limit. The problem is most severe for the faintest galaxies or those which have the least secure photometric redshifts. In Figure 2.22, we show the measured β as a function of UV magnitude for one of our Monte Carlo samples alongside the M_{UV} binned bi-weight means and other

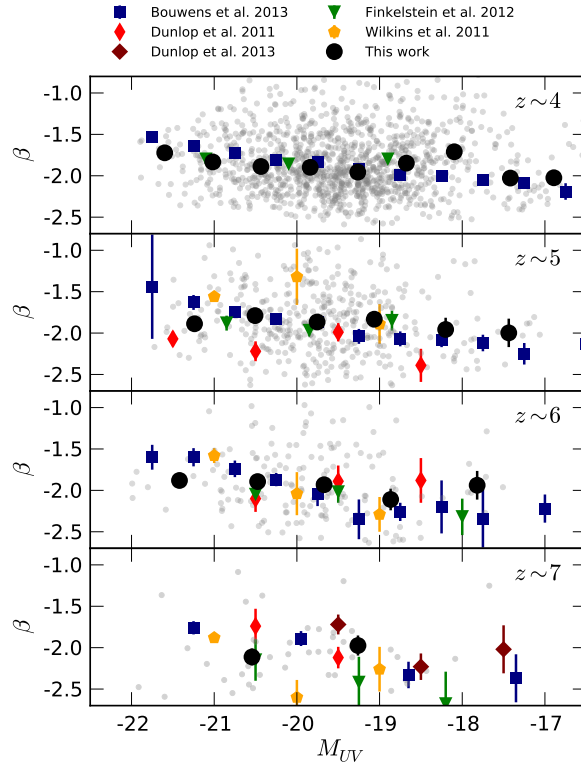


Figure 2.22: Measured UV continuum slope as a function of UV magnitude for this work and previous studies. The background grey circles show the individual points for one of the Monte Carlo samples used in our work. The black circles show the biweight mean β and corresponding standard error on the mean as a function of M_{UV} averaged over 100 of our Monte Carlo samples. Also shown are the equivalent M_{UV} binned means available from the literature.

values from the literature. We do not see a strong piling up of sources at the bluest templates (≈ -2.69 when nebular emission is included) suggesting our observations are not strongly affected by this. However, it may have a small effect on the average β for a fixed M_{UV} (see Figure 3.2).

Because we apply the dust correction to each galaxy based on its own measured β , rather than an observed average, our dust corrections will be unaffected by any such bias if it does exist. For any galaxy bluer than $\beta = -2.23$, the applied extinction based on the relation of Meurer, Heckman & Calzetti (1999) is 0.

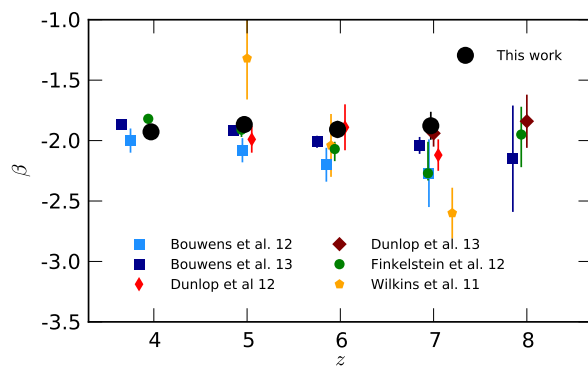


Figure 2.23: UV continuum slope as a function of redshift for a fixed UV magnitude. The points from (Finkelstein *et al.*, 2012b) are for a fixed $M_{UV} \sim 20$, all other data points are for $M_{UV} \sim 19.5$.

Chapter 3

Powering reionization

3.1 Introduction

At the present day, the intergalactic and interstellar medium (IGM,ISM) are known to be predominantly ionized. However, following recombination at $z \approx 1100$, the baryon content of the Universe was mostly neutral. At some point in the history of the Universe, the IGM underwent a transition from this neutral phase to the ionized medium we see today, a period known as the epoch of reionization (EoR hereafter). The strongest constraints on when reionization occurred are set by observations of the Gunn-Peterson trough of distant quasars (Fan, Carilli & Keating, 2006), which indicate that by $z \approx 5.5$, the Universe was mostly ionized (with neutral fractions $\sim 10^{-4}$). Additionally, measurements of the total optical depth of electrons to the surface of last scattering implies that reionization should be occurring at higher redshift, towards $z \approx 10$, for models of instantaneous reionization (Hinshaw *et al.*, 2013; Bennett *et al.*, 2013). However, critical outstanding questions still remain. Firstly, when did the intergalactic hydrogen and helium complete reionization? And secondly, what were the sources of ionizing photons which powered the reionization process? Was it predominantly powered by star-forming galaxies or by active galactic nuclei/quasars?

For hydrogen reionization with its earlier completion, the rapid decline in the quasar luminosity function at high redshift (Willott *et al.*, 2010; Fontanot, Cristiani & Vanzella, 2012; Fontanot *et al.*, 2014) does suggest that star-forming galaxies are the most likely

candidates for completing the bulk of reionization by $z \sim 6$. The contribution from faint AGN could still however make a significant contribution to the ionizing emissivity at $z > 4$ (Giallongo *et al.*, 2015). Based on the optical depth constraints set by WMAP (Hinshaw *et al.*, 2013) and either observed IGM emissivities at lower redshift (Kuhlen & Faucher-Giguère, 2012; Robertson *et al.*, 2013; Becker & Bolton, 2013), or emissivities predicted by simulations (Ciardi *et al.*, 2012), several studies have drawn the same conclusion that faint galaxies from below the current detection limits and/or an increasing ionizing ‘efficiency’ at higher redshift is required. Even with the lower optical depth measurement now favoured by the recent Planck analysis (Planck Collaboration *et al.*, 2015), such assumptions are essentially still required to satisfy these criteria (Robertson *et al.*, 2015).

One of the possible mechanisms for this increasing ionizing efficiency is an evolution in the fraction of the ionizing photons able to escape their host galaxy and ionize the surrounding IGM, known as the escape fraction (f_{esc}). There have been several studies designed to understand this issue, but there are still large uncertainties in what the escape fraction for galaxies is and how it evolves with redshift and other galaxy properties. In a study of $z \sim 1.3$ galaxies, Siana *et al.* (2010) searched for Lyman-continuum photons from star forming galaxies, although no systems were detected. After correcting for the Lyman-break and IGM attenuation the limit placed on the escape fraction is $f_{\text{esc}} < 0.02$ after stacking all sources. Bridge *et al.* (2010) find an even lower limit of $f_{\text{esc}} < 0.01$ using slitless spectroscopy at $z \sim 0.7$, although one AGN in their sample is detected. However, higher escape fractions of $\sim 5\%$ to $\sim 20 - 30\%$ have been measured for galaxies at $z \sim 3$ (Shapley *et al.*, 2006; Iwata *et al.*, 2009; Vanzella *et al.*, 2010; Nestor *et al.*, 2013), consistent with the relatively high $f_{\text{esc}} \sim 0.2$ expected from IGM recombination rates determined from Ly α forests (Bolton & Haehnelt, 2007). Furthermore, the average f_{esc} for galaxies at $z \sim 3$ may be significantly higher than the existing measurements due to the selection biases introduced by the Lyman-break technique (Cooke *et al.*, 2014).

It is important to bear in mind that the property which is fundamental to studies of reionization is the total number of ionizing photons which are available to ionize the intergalactic medium surrounding galaxies. Hence, while the escape fraction is a criti-

cal parameter for reionization, it must be measured or constrained in conjunction with the underlying continuum emission to which it applies. For example, an increase in f_{esc} may not have an effect on reionization if it is accompanied by a reduction in the intrinsic number of ionizing photons being produced.

As shown in Robertson *et al.* (2013) (see also Leitherer *et al.* 1999), the number of ionizing photons produced per unit UV luminosity emitted (e.g. $L_{1500\text{\AA}}$) can vary significantly as a function of the stellar population parameters such as age, metallicity and dust extinction. Thankfully, evolution or variation among the galaxy population in these parameters will not only influence the production of ionizing photons but will have an effect on other observable properties such as the UV continuum slope (β , Calzetti, Kinney & Storchi-Bergmann 1994). With the advent of ultra-deep near-infrared imaging surveys such as the UDF12 (Koekemoer *et al.*, 2013) and CANDELS (Grogin *et al.*, 2011; Koekemoer *et al.*, 2011) surveys, observations of the UV continuum slope extending deep into the epoch of reionization are now available. Furthermore, there is now strong evidence for an evolution in β as a function of both galaxy luminosity and redshift out to $z \sim 8$ (Bouwens *et al.*, 2014a; Rogers *et al.*, 2014).

In this paper we use the latest observations of β spanning the EoR combined with SED modelling, incorporating the physically motivated escape mechanisms to explore what constraints on the key emissivity coefficients are currently available. We also explore the consequences these constraints may have on the EoR for current observations of the star-formation rates in this epoch. In addition to the observations of in-situ star-formation through the UV luminosity functions, we also investigate whether recent measurements of the galaxy stellar mass function and stellar mass density at high redshift (Duncan *et al.*, 2014; Grazian *et al.*, 2014) can provide additional useful constraints on the star-formation rates during EoR (Stark *et al.*, 2007; González *et al.*, 2010).

In Section 3.2, we outline the physics and critical parameters required to link the evolution of the neutral hydrogen fraction to the production of ionizing photons. We also explore plausible physical mechanisms for the escape of Lyman continuum photons from galaxies, outlining the models explored throughout the paper. We then review the current literature constraints on the UV continuum slope, β , both as a function of

redshift and galaxy luminosity. Next, in Section 3.3, we explore how the escape fraction, dust extinction and other stellar population parameters affect the observed β and the coefficients relating ionizing photon production rates to observed star-formation rates and UV luminosities. In Section 3.4, we apply these coefficients to a range of existing observations, exploring the predicted ionizing emissivity throughout the epoch of reionization for both constant and redshift dependent conversions. We then discuss how the varying assumptions and proposed relations would impact the ionizing photon budget consistent with current observations before outlining the future prospects for improving these constraints in Section 3.5. Finally, we summarise our findings and conclusions in Section 3.6.

Throughout this paper, all magnitudes are quoted in the AB system (Oke & Gunn, 1983). We also assume a Λ -CDM cosmology with $H_0 = 70 \text{ kms}^{-1}\text{Mpc}^{-1}$, $\Omega_m = 0.3$ and $\Omega_\Lambda = 0.7$. Quoted observables (e.g. luminosity density) are expressed as actual values assuming this cosmology. We note that luminosity and luminosity based properties such as stellar masses and star-formation rates scales as h^{-2} , whilst densities scale as h^3 .

3.2 Linking reionization with observations

3.2.1 The ionizing emissivity

The currently accepted theoretical picture of the epoch of reionization, as initially described by Madau, Haardt & Rees (1999), outlines the competing physical processes of ionization of neutral hydrogen by Lyman continuum photons and recombination of free electrons and protons. The transition from a neutral Universe to a fully ionized one can be described by the differential equation:

$$\dot{Q}_{\text{HII}} = \frac{\dot{N}_{\text{ion}}}{\langle n_{\text{H}} \rangle} - \frac{Q_{\text{HII}}}{\langle t_{\text{rec}} \rangle} \quad (3.1)$$

where Q_{HII} is the dimensionless filling factor of ionized hydrogen (such that $Q_{\text{HII}} = 1$ for a completely ionized Universe) and \dot{N}_{ion} is the comoving ionizing photon production rate ($\text{s}^{-1} \text{ Mpc}^{-3}$) or ionizing emissivity. The comoving density of hydrogen atoms, $\langle n_{\text{H}} \rangle$, and average recombination time $\langle t_{\text{rec}} \rangle$ are redshift dependent and is dependent

on the primordial Helium abundance, IGM temperature and crucially the inhomogeneity of the IGM, parametrised as the so-called clumping factor $C_{\text{HII}} \equiv \langle n_{\text{H}}^2 \rangle / \langle n_{\text{H}} \rangle^2$ (Pawlik, Schaye & vanScherpenzeel, 2009). We refer the reader to Madau, Haardt & Rees (1999), Kuhlen & Faucher-Giguère (2012) and Robertson *et al.* (2010, 2013) for full details on these parameters and the assumptions associated.

In this paper we will concentrate on \dot{N}_{ion} and the production of Lyman continuum photons by star-forming galaxies. The link between the observable properties of galaxies and the ionizing photon rate, \dot{N}_{ion} can be parametrised as

$$\dot{N}_{\text{ion}} = f_{\text{esc}} \xi_{\text{ion}} \rho_{\text{UV}} \quad (3.2)$$

following the notation of Robertson *et al.* (2013), where ρ_{UV} is the observed UV (1500Å) luminosity density (in $\text{erg s}^{-1} \text{Hz}^{-1} \text{Mpc}^{-3}$), ξ_{ion} the number of ionizing photons produced per unit UV luminosity ($\text{erg}^{-1} \text{Hz}$) and f_{esc} the fraction of those photons which escape a host galaxy into the surrounding IGM. Alternatively, \dot{N}_{ion} can be considered in terms of the star-formation rate density, ρ_{SFR} ($\text{M}_{\odot} \text{yr}^{-1} \text{Mpc}^{-3}$),

$$\dot{N}_{\text{ion}} = f_{\text{esc}} \kappa_{\text{ion}} \rho_{\text{SFR}} \quad (3.3)$$

where κ_{ion} ($\text{s}^{-1} \text{M}_{\odot}^{-1} \text{yr}$) is the ionizing photon production-rate per unit star-formation (ζ_Q in the notation used in Robertson *et al.* (2010)). In addition to observing ρ_{UV} or ρ_{SFR} during the EoR, accurately knowing f_{esc} , ξ_{ion} and κ_{ion} is therefore critical to estimating the total ionizing emissivity independent of how well we are able to measure the UV luminosity or star-formation rate densities.

As the production of LyC photons is dominated by young UV-bright stars, the rate of ionizing photons is therefore highly dependent on the age of the underlying stellar population and the recent star-formation within the galaxy population. Physically motivated values of ξ_{ion} (or its equivalent coefficient in other notation) can be estimated from stellar population models based on plausible assumptions on the properties of high-redshift galaxies (Bolton & Haehnelt, 2007; Ouchi *et al.*, 2009; Kuhlen & Faucher-Giguère, 2012).

However, with observations of the UV continuum slope, β (Calzetti, Kinney & Storchi-Bergmann, 1994), now extending deep into the epoch of reionization, limited spectral

information is now available for a large sample of galaxies. Despite the many degeneracies in β (see later discussion in Section 3.3), it is now possible to place some constraints on whether the assumptions made are plausible. In Robertson *et al.* (2013), values of ξ_{ion} are explored for a range of stellar population parameters relative to the β observations of Dunlop *et al.* (2013). Based on the range of values consistent with the observed values of $\beta \approx -2$, Robertson *et al.* choose a physically motivated value of $\log_{10} \xi_{ion} = 25.2$.

Typically, a constant f_{esc} is applied to all galaxies in addition to the estimated or assumed values of ξ_{ion}/κ_{ion} (Ouchi *et al.*, 2009; Finkelstein *et al.*, 2012a; Robertson *et al.*, 2013), motivated in part by our lack of understanding of the redshift or halo mass dependence of f_{esc} . However, applying a constant f_{esc} does not take into account exactly how the Lyman continuum photons escape the galaxy, what effect the different escape mechanism might have on the observed galaxy colours, and how that might alter the assumed ξ_{ion}/κ_{ion} based on β .

3.2.2 Mechanisms for Lyman continuum escape

In Zackrisson, Inoue & Jensen (2013), detailed SSP and photo-dissociation models were used to explore how future observations of β and H α equivalent-width with the James Webb Space Telescope (JWST) could be used to constrain the escape fraction for two different Lyman continuum escape mechanisms (see Fig. 8 of Zackrisson, Inoue & Jensen (2013)). However, it may already be possible to rule out significant parts of the f_{esc} and dust extinction parameter space using current constraints on β and other galaxy properties. To estimate the existing constraints on f_{esc} , ξ_{ion} , κ_{ion} and their respective products, we combine the approaches of Zackrisson, Inoue & Jensen (2013) and Robertson *et al.* (2010, 2013). To do this, we model β , ξ_{ion} and κ_{ion} as a function of f_{esc} for the two models of Zackrisson, Inoue & Jensen (2013). The components and geometry of these two models are illustrated in Fig. 3.1.

In the first model, model A hereafter (Fig. 3.1 left) and dubbed ‘ionization bounded nebula with holes’ by Zackrisson, Inoue & Jensen, Lyman continuum photons along with unattenuated starlight are able to escape through low-density holes in the neutral ISM. In this model, the escape fraction is determined by the total covering fraction

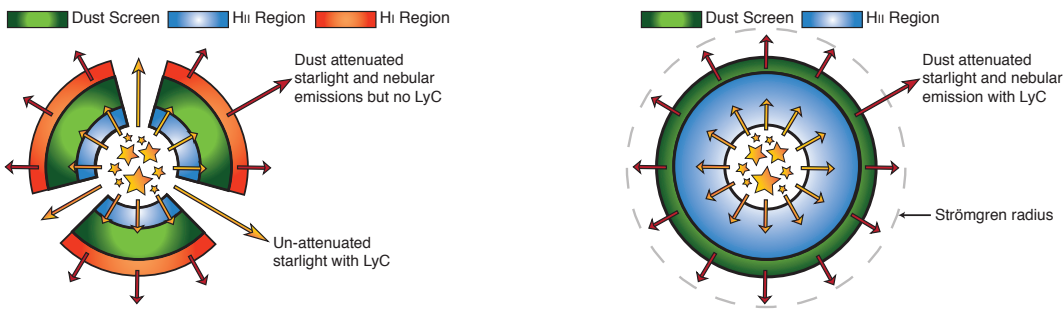


Figure 3.1: Schematic cartoon illustrations of the Lyman continuum escape mechanisms outlined in Section 3.2. For both models, the stars represent a central galaxy surrounded by a HII ionization region, dust is distributed in an outer dust-screen. Left: An ionization bounded nebula with holes (sometimes referred to as the ‘picket fence model’) in which LyC escapes through holes in the ISM. Right: a density bounded nebula where LyC is able to escape due to the incomplete Strömgren sphere formed when the galaxy depletes its supply of neutral hydrogen.

of the neutral ISM. Under the assumption that these holes are small and evenly distributed, the observed galaxy SED (averaged across the galaxy as in the case of photometry) would then be a combination of the unattenuated starlight from holes and the dust reddened starlight and nebular emission from the HI enshrouded regions.

A second model, model B hereafter (Fig. 3.1 right) corresponds to the ‘density bounded nebula’ of Zackrisson, Inoue & Jensen (2013). This model could occur when the local supply of HI is exhausted before a complete Strömgren sphere can form, allowing Lyman continuum photons to escape into the surrounding ISM. The fraction of LyC photons which can escape the nebular region is determined by the fraction of the full Strömgren radius at which the nebular region is truncated. The total escape fraction is then also dependent on the optical depth of the surrounding dust screen.

Of these two mechanisms, the former (Model A: ionization bounded nebula with holes) is the model which most closely represents the physics predicted by full radiation hydrodynamical models of dwarf galaxies. In Wise & Cen (2009), it was found that Lyman continuum radiation preferentially escaped through channels with low column densities, produced by radiative feedback from massive stars. The resulting distribution of LyC escape fraction within a galaxy is highly anisotropic and varies significantly between different orientations. Evidence for such an anisotropic escape mechanism has also been found recently by Zastrow *et al.* (2013), who find optically thin ionization cones through which LyC can escape in nearby dwarf starbursts. Similarly, Borthakur *et al.* (2014) find a potential high-redshift galaxy analog at $z \sim 0.2$ with evidence for LyC leakage through holes in the surrounding neutral gas with an escape

fraction as high as $f_{esc} \approx 0.2$ (21%).

However, this value represents the optimum case in which there is no dust in or around the low-density channels (corresponding to Model A). For the same system, when Borthakur *et al.* (2014) include dust in the low-density channels, the corresponding total LyC escape fraction is reduced to $\approx 1\%$. The two models explored in this work represent the two extremes of how dust extinction will effect the escaping Lyman continuum for toy models such as these, the dust-included estimates of Borthakur *et al.* (2014) therefore represent a system which lies somewhere between Models A and B.

A potential third mechanism for Lyman continuum escape was posited by Conroy & Kratter (2012), whereby ‘runaway’ OB stars which have traveled outside the galaxy centre can contribute a significant amount to the LyC emitted into the surrounding IGM. For high-redshift galaxies with significantly smaller radii than local galaxies, massive stars with large velocities could venture up to 1 kpc away from their initial origin into regions with low column density. Conroy & Kratter (2012) estimate that these stars could in fact contribute 50 – 90% of the escaping ionizing radiation. In contrast, recent work by Kimm & Cen (2014) finds that when runaway stars are included into their models of Lyman continuum escape, the time average escape fraction only increases by $\sim 20\%$. Given the additional complications in modelling the relevant observational properties and their relatively small effect, we neglect the contribution of runaway stars in the subsequent analysis.

In Section 3.3, we describe how we model both the observable (β) and unobservable (ξ_{ion}, κ_{ion}) properties for both model A and model B. But first, we examine the existing observations on the evolution of β into the epoch of reionization.

3.2.3 Observed UV Continuum Slopes

In Fig. 3.2, we show a compilation of recent results in the literature on the observed UV slope, β , as a function of both redshift and rest-frame UV magnitude, M_{UV} (Dunlop *et al.*, 2011, 2013; Wilkins *et al.*, 2011; Finkelstein *et al.*, 2012b; Bouwens *et al.*, 2014a; Duncan *et al.*, 2014; Rogers *et al.*, 2014). Disagreement between past observations on the existence or steepness of a color-magnitude relation (cf. Dunlop *et al.*

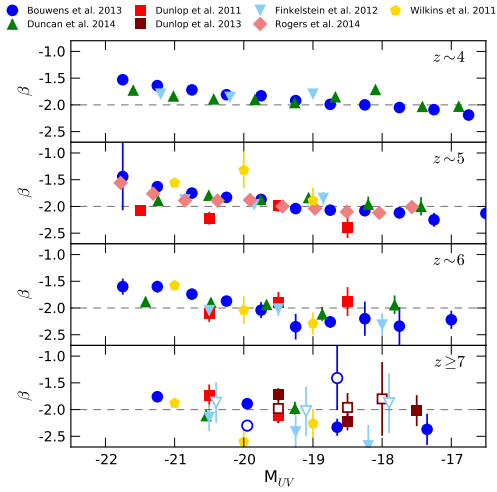


Figure 3.2: Observed average values of the UV continuum slopes β as a function of rest-frame UV magnitude, M_{UV} , from Wilkins *et al.* (2011), Dunlop *et al.* (2011, 2013), Finkelstein *et al.* (2012b), Bouwens *et al.* (2014a), Duncan *et al.* (2014) and Rogers *et al.* (2014) at redshifts $z \sim 4, 5, 6$ and $7 - 9$. In the bottom panel, filled symbols show the average for $z \sim 7$ samples while the open symbols show the averages for $z \geq 8$ (see respective papers for sample details and redshift ranges).

(2011) and Bouwens *et al.* (2011a)) have recently been reconciled by Bouwens *et al.* (2014a) after addressing systematics in the selection and photometry between different studies. Bouwens *et al.* (2014a) find a clear colour-magnitude relation (CMR) with bluer UV-slopes at lower luminosities, the relation is also found to evolve with bluer β 's at high redshift (blue circles in Fig. 3.2). The existence of a strong colour-magnitude relation has also been confirmed by Rogers *et al.* (2014) at $z \sim 5$ for a sample of even greater dynamic range (pink diamonds in Fig. 3.2), measuring a CMR slope and intercept within error of the measured $z \sim 5$ values of Bouwens *et al.* (2014a).

Past studies have often used a fixed average $\beta = -2$ to motivate or constrain ξ_{ion} , e.g. Bolton & Haehnelt (2007), Ouchi *et al.* (2009), Robertson *et al.* (2010, 2013) and Kuhlen & Faucher-Giguère (2012). However, given the confirmed observations of a $M_{UV} - \beta$ relation and apparent redshift evolution, such an assumption may no longer be valid. In order to estimate an average β which takes into account the corresponding number densities and luminosities of galaxies with different β s, we calculate $\langle \beta \rangle_{\rho_{UV}}$, the average β weighted by the contribution to the total UV luminosity density:

$$\langle \beta \rangle_{\rho_{UV}} = \frac{\int_{L_{min}}^{\infty} L_{UV}(m) \times \phi(m) \times \langle \beta \rangle(m)}{\int_{L_{min}}^{\infty} L_{UV}(m) \times \phi(m)} \quad (3.4)$$

where $L_{UV}(m)$, $\phi(m)$ and $\langle \beta \rangle(m)$ are the luminosity, number density and average β at the rest-frame UV magnitude, m , respectively. We choose a lower limit of $L_{UV} \equiv$

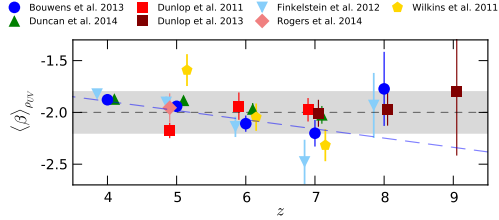


Figure 3.3: Luminosity-weighted average β , $\langle \beta \rangle_{\rho_{UV}}$, as a function of redshift for the $M_{UV} - \beta$ observations shown in Fig. 3.2. The grey shaded region covers the range $-2.2 < \beta < -1.8$ and the blue long-dashed line shows our parametrisation of $\langle \beta \rangle_{\rho_{UV}}$ vs z based on the observations of Bouwens *et al.* (2014a) (blue circles) at $z \lesssim 7$.

$M_{UV} = -17$, corresponding to the approximate limiting magnitude of the deepest surveys at $z \geq 6$. For the discrete bins in which $\langle \beta \rangle(m)$ is calculated, $\langle \beta \rangle_m$, this becomes a sum over the bins of absolute magnitude, k , brighter than our lower limit $M_{UV} = -17$:

$$\langle \beta \rangle_{\rho_{UV}} = \frac{\sum_k L_{UV,k} \times \phi_k \times \langle \beta \rangle_k}{\sum_k L_{UV,k} \times \phi_k}. \quad (3.5)$$

The number density for a given rest-frame magnitude bin, ϕ_k , is calculated from the best-fitting UV luminosity functions of Bouwens *et al.* (2014b) at the corresponding redshift. We use the same luminosity function at each redshift for all of the observations for consistency. We note that given the relatively good agreement between estimates given their errors, the use of differing luminosity function estimates would have minimal effect on the calculated values. We estimate errors on $\langle \beta \rangle_{\rho_{UV}}$ through a simple Monte Carlo simulation, whereby $\langle \beta \rangle_m$ and the best-fitting Schechter (1976) parameters used to calculate ϕ_m are perturbed by the quoted errors (making use of the full covariance measured by Bouwens *et al.* 2014b), this is repeated 10^4 times. $\langle \beta \rangle_{\rho_{UV}}$ and error are then taken as the median and 1σ range of the resulting distribution.

Fig. 3.3 shows the calculated $\langle \beta \rangle_{\rho_{UV}}$ and corresponding errors for each of the samples shown in Fig. 3.2. Overall, across all redshifts we can see that $\beta \approx -2$ is still a valid choice for a fiducial value of β during the epoch of reionization ($z > 6$) based on all of the existing observations. However, focusing only on the least-biased observations with the greatest dynamic range from Bouwens *et al.* (2014a), there is evidence for evolution at $z < 7$. Specifically, from $z \sim 4$ to $z \sim 7$, $\langle \beta \rangle_{UV}$ steepens considerably from -1.9 ± 0.02 to -2.21 ± 0.14 .

We note that at $z \approx 8$, the $\langle \beta \rangle_{\rho_{UV}}$ changes significantly depending on the choice of average due to the significantly smaller samples observable and large scatter in

the faintest bin. For example, using the bi-weight means recommended by Bouwens *et al.* (2014a), $\langle \beta \rangle_{\rho_{UV}} = -1.74$ based on their observations. Re-calculating using the inverse-weighted means of this same sample gives $\langle \beta \rangle_{\rho_{UV}} = -2.1$, in better agreement with the observed trend at $z < 8$. Due to this large uncertainty at $z \gtrsim 8$, we parametrise the evolution of $\langle \beta \rangle_{\rho_{UV}}$ as a function of redshift based on the Bouwens *et al.* (2014a) measurements at $z \lesssim 7$. Assuming a simple linear relation with redshift, we find:

$$\langle \beta \rangle_{\rho_{UV}}(z) = -(1.54 \pm 0.07) - (0.09 \pm 0.02) \times z. \quad (3.6)$$

Based on this fit we predict a $\langle \beta \rangle_{\rho_{UV}} = -2.26$ for $z \sim 8$. Whilst this is significantly bluer than that based on the existing observations at $z \sim 8$, it is comparable to the average β measured for fainter galaxies in the lower redshift samples and represents a reasonable extrapolation.

While there is now good agreement on the existence and slope of the colour-magnitude relation between independent studies (Bouwens *et al.* 2014a and Rogers *et al.* 2014), what is less well understood is the intrinsic scatter in the CMR and whether it is luminosity dependent. Currently, the most extensive study of the intrinsic scatter is that of Rogers *et al.* (2014), who found that the intrinsic scatter in β is significantly larger for bright galaxies. They also find an apparent lower limit (25th percentile) of $\beta = -2.1$ which varies little with galaxy luminosity whilst the corresponding 75th percentiles increase significantly from fainter to brighter galaxies. Such a scenario implies that galaxies with $\beta \leq -2.5$ should be extremely rare at high-redshift, even though such galaxies are observed locally and at intermediate redshifts (Stark *et al.*, 2014a). Without a better understanding of the causes of the intrinsic scatter in β and the underlying stellar populations it is difficult to predict the expected numbers of such galaxies during this epoch.

Rogers *et al.* interpret the intrinsic scatter as consistent with two simple scenarios: 1) the scatter is due to galaxy orientation, or 2) that brighter galaxies have more stochastic star-formation histories and the β variation is a result of observing galaxies at different points in the duty cycle of star-formation. However, this second scenario is contrary to the theoretical predictions of Dayal *et al.* (2013), whereby fainter low-mass galaxies have more stochastic star-formation histories due to the greater effect of feedback shutting down star-formation in low-mass haloes.

After the discovery that high-redshift galaxies exhibit significant UV emission lines by Stark *et al.* (2014b) (specifically CIII] at 1909Å), it is worth asking if the presence of such far-UV emission lines can systematically affect measurements of the UV slope to the same degree which optical emission lines can affect age estimates and stellar masses. In Stark *et al.* (2014a), the authors find that the fitting of β is not affected by the presence of UV emission lines in a sample of young low-mass galaxies at $z \sim 2$. The same is true for galaxies out to $z \lesssim 6$, where β is typically measured by fitting a power-law to three or more filters (Bouwens *et al.*, 2014a). However, at $z \geq 7$ where β must be measured using a single colour, the effect of UV emission line contamination in one of the filters is more significant. For a CIII] equivalent width of 13.5Å (the highest observed in the Stark *et al.* (2014a) sample at $z \sim 2$) could result in a measured β which is too red by $\Delta\beta \approx 0.18$ relative to the intrinsic slope based on the method outlined in Section 3.3.

Given the limited samples of $z \gtrsim 6$ galaxies with UV emission line detections, fully quantifying the effects of the emission line contamination on β observations is not possible at this time. As such, in this work we do not include UV emission lines in our simulated SEDs or attempt to correct for their effects on the observed β s in Fig. 3.3. We do caution that despite the significant improvement on β measurements at high redshift, there may still be unquantified systematics when interpreting the UV slope during the EoR.

3.3 Modelling β , ξ_{ion} and κ_{ion}

To model the apparent β 's and corresponding emissivity coefficients for our two Lyman continuum escape models, we make use of composite stellar population models from Bruzual & Charlot (2003) (BC03). Using a stellar population synthesis code, we are able to calculate the full spectral energy distribution for a stellar population of the desired age, star-formation history, metallicity and dust extinction. Our code allows for any single-parameter star-formation history (e.g. exponential decline, power-law, truncated or ‘delayed’ star-formation models), and a range of dust extinction models. The models also allow for the inclusion of nebular emission (both line and continuum

emission) proportional to the LyC photon rate, full details of which can be found in Duncan *et al.* (2014).

For each resulting SED with known star-formation rate (SFR), we calculate the UV luminosity by convolving the SED with a top-hat filter of width 100Å centred around 1500Å, as is standard practice for such studies (e.g. Finkelstein *et al.* 2012a, McLure *et al.* 2013). To measure β , each SED is redshifted to $z \sim 7$ and convolved with the WFC3 F125W and F160W filter responses (hereafter J_{125} and H_{160} respectively). We then calculate β as:

$$\beta = 4.43(J_{125} - H_{160}) - 2. \quad (3.7)$$

as in Dunlop *et al.* (2013). This method is directly comparable to how the majority of the high redshift observations were made and should allow for direct comparison when interpreting the observations with these models. Using comparable colours at $z \sim 5$ and $z \sim 6$ or different combinations of filters has minimal systematic effect on the calculated values of β (see Dunlop *et al.* 2011 and Appendix of Bouwens *et al.* 2012a).

The LyC flux from these models is calculated before and after the applied absorption by gas (for nebular emission) and dust. We are therefore able to calculate the total escape fraction of LyC photons for a given stellar population. Using these values, it is therefore relatively straight-forward to link the observed β distribution of high-redshift galaxies with the distribution of predicted κ_{ion} or L_{UV} per unit SFR and the corresponding $f_{esc,tot}$.

For the ionization-bounded nebula with holes model (Model A), the ‘observed’ SED is a weighted (proportional to f_{esc}) sum of the un-attenuated starlight escaping through holes and the attenuated starlight and nebular emission from the H II and dust enclosed region. The two SED components are weighted proportional to the covering fraction ($\equiv 1 - f_{esc}$) of the H II and dust region. The resulting observable quantities are effectively the average over all possible viewing angles, as would be expected for a large sample of randomly aligned galaxies.

In the case of Model B, the density bounded nebula, Lyman continuum emission from the underlying stellar spectrum is partially absorbed by the surrounding truncated Strömgren sphere with an escape fraction $f_{esc,neb}$. The remaining Lyman continuum photons along with the UV-optical starlight and nebular emission are then attenuated

by the surrounding dust shell according to the chosen dust attenuation law. The total escape fraction for this model is therefore

$$f_{esc} = 10^{0.4 \times A(LyC)} f_{esc,neb} \quad (3.8)$$

where $A(LyC)$ is the magnitude of dust extinction for Lyman continuum photons and is highly dependent on the choice of attenuation curve (see Section 3.3.1.6).

3.3.1 Modelling assumptions: current constraints on stellar populations at $z > 3$

Although there are now good constraints on both the UV luminosity function and UV continuum slope at high redshift, both of these values suffer strong degeneracies with respect to many stellar population parameters. As such, constraints on f_{esc} , ξ_{ion} and κ_{ion} still requires some assumptions or plausible limits set on the range of some parameters. In this section we outline the existing constraints on the relevant stellar population properties at high-redshift, discuss what assumptions we make in our subsequent analysis, and explore the systematic effects of variations in these assumptions.

3.3.1.1 Star-formation history

Typically, star formation histories are parameterised as exponential models,

$$\rho_{SFR}(t) \propto \exp\left(-\frac{t - t_f}{\tau}\right), \quad (3.9)$$

where τ is the characteristic timescale and can be negative or positive (for increasing or decreasing SFH respectively). Or, alternatively as a power-law, following

$$\rho_{SFR}(t) \propto (t - t_f)^\alpha. \quad (3.10)$$

The star-formation history (SFH) of high-redshift galaxies, $SFR(t)$, is still very poorly constrained due to the limited rest-frame wavelengths available for SED fitting or spectroscopy. For large samples of both intermediate and high redshift galaxies, it has been found that rising SFHs produce better SED fits to the observed photometry (Maraston *et al.*, 2010; Lee *et al.*, 2014). However, reliably constraining the characteristic

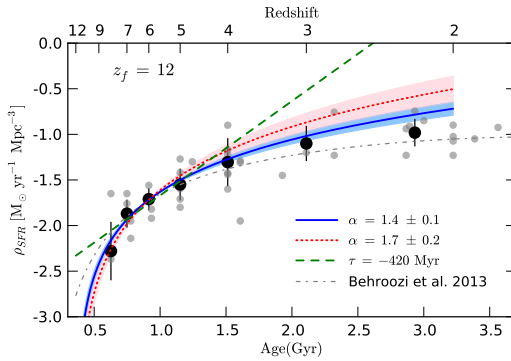


Figure 3.4: Power-law (blue continuous: Salmon *et al.* 2014, red dotted: Papovich *et al.* 2011) and exponential (green dashed: Papovich *et al.* 2011) fits to the median observed SFR-densities at $z > 4$ for 3 different star formation histories. For the power-law fits, the shaded red and blue regions correspond to the $1-\sigma$ errors on the slope of the power-law, α , quoted in the respective papers. The grey dot-dashed line shows the best-fit to the median star-formation rates across the full cosmic history for the functional form outlined in Behroozi, Wechsler & Conroy (2013). All of the models assume an initial onset of star-formation at $z_f = 12$.

timescales, τ or α , for individual galaxies at $z > 2$ is not possible for all but the brightest sources.

Using a comoving number density selected sample of galaxies at high redshift, Papovich *et al.* (2011) found the average star formation history between $3 < z < 8$ to be best-fitted by a power-law with $\alpha = 1.7 \pm 0.2$ or an exponentially rising history with $\tau = 420$ Myr. Recently, for the deep observations of the CANDELS GOODS South field, Salmon *et al.* (2014) applied an improved version of this method (incorporating the predicted effects of merger rates on the comoving sample) and found a shallower power-law with $\alpha = 1.4 \pm 0.1$ produced the closest match.

In Fig. 3.4, we show that all three of these models ($\alpha = 1.4/1.7$ and $\tau = -450$ Myr) can provide a good fit to the observed evolution in the cosmic star-formation rate density at $z > 3$ (Age of the Universe $\lesssim 2$ Gyr) through a simple scaling alone. However, the power-law fit with $\alpha = 1.4$ provides the best fit to not only to the evolution of the SFR-density at ages < 2 Gyr, but also to the SFR density at later epochs. A smoothly rising star-formation is also favoured by hydrodynamic models such as Finlator, Oppenheimer & Davé (2011) and Dayal *et al.* (2013), although the star-formation histories of individual galaxies are likely to be more varied or stochastic (Dayal *et al.*, 2013; Kimm & Cen, 2014). Furthermore, there is also growing evidence of galaxy populations with older populations and possibly quiescent populations (Nayyeri *et al.*, 2014; Spitler *et al.*, 2014) suggesting some galaxies form very rapidly at high-redshift before

becoming quenched. The assumption of a single parametrised SFH is clearly not ideal, however our choice of a rising power-law SFH with $\alpha = 1.4$ is at least well motivated by observations and a more physical choice than a constant or exponentially declining SFH.

3.3.1.2 Initial mass function

Interpretation of extragalactic observations through modelling and SED fitting is typically done assuming a universal bi-modal Milky Way-like initial mass function (IMF) such as Kroupa (2001)/Chabrier (2003) or the unimodal Salpeter (1955) IMF. However, there is now growing evidence for systematic variation in the IMF of both nearby (vanDokkum & Conroy, 2010; Treu *et al.*, 2010; Cappellari *et al.*, 2012; Conroy & vanDokkum, 2012; Ferreras *et al.*, 2013) and distant (Martín-Navarro *et al.*, 2014) early-type galaxies.

Under a hierarchical model of galaxy evolution with downsizing, the bright galaxies in overdense regions observed at $z > 3$ are likely to eventually form into the massive early-type galaxies in which these variations can be found. Variation in the slope of the IMF would have a significant effect on many of the critical observable properties at high redshift such as stellar masses and mass to UV light ratio's. However, given the lack of theoretical understanding as to how the IMF should vary with physical conditions, incorporating the effects of a varying IMF at high-redshift is beyond the scope of this work. Throughout the following analysis we use the Chabrier (2003) IMF as our primary assumption, but also consider the systematic effect of a steeper IMF such as Salpeter (1955) on the inferred values or observables in Appendix ??.

3.3.1.3 Metallicity

Current spectroscopic constrains on galaxy metallicities at $z \geq 3$ indicate moderately sub-solar stellar and gas-phase metallicities (Shapley, Steidel & Pettini, 2003; Maiolino *et al.*, 2008b; Laskar, Berger & Chary, 2011; Jones, Stark & Ellis, 2012; Sommariva *et al.*, 2012). In addition, Troncoso *et al.* (2014), present measurements for 40 galaxies at $3 < z < 5$ for which the observed metallicities are consistent with a

downward evolution in the mass-metallicity relation (with increasing redshift).

Measurements of galaxy metallicities at higher redshift ($z > 6$) are even fewer due to the lack of high-resolution rest-frame optical spectroscopy normally required to constrain metallicity. However, thanks to a clear detection of the CIII] emission line (1909Å) and strong photometric constraints, Stark *et al.* (2014b) are able to measure a metallicity of $\approx 1/20$ th solar metallicity for a lensed galaxy at $z = 6.029$. Given these observations and the metallicities available in the Bruzual & Charlot (2003) models, we assume a fiducial metallicity of $\approx 1/5$ th solar metallicity ($Z = 0.004 = 0.2Z_{\odot}$).

3.3.1.4 Age

For the rising star-formation history used throughout this work, there is a weak evolution of β as a function of age ($\Delta\beta \approx 0.13$ between $t \approx 100$ Myr and ≈ 1 Gyr) whereby older stellar populations have redder UV continuum slopes. However, at very young ages, the contribution of nebular continuum emission in the UV continuum can also significantly redden the apparent β compared to the much steeper underlying intrinsic UV slope (Robertson *et al.*, 2010). This results in a degeneracy with respect to β between young and old populations. For example, for identical observed (stellar + nebular continuum) UV-slopes, ξ_{ion} (and κ_{ion}) for a young stellar population can be a factor of up ~ 0.5 (0.2) dex higher. Given this degeneracy, additional constraints from other parts of the electromagnetic spectrum are required in order to make a well informed choice of stellar population age.

Due to the observational restrictions on high-resolution rest-frame optical spectroscopy, measurement of stellar population ages for high-z galaxies is limited to photometric fitting and colour analysis. At $z \sim 4$, where the Balmer break can be constrained through deep *Spitzer* IRAC photometry, estimates of the average stellar population ages vary significantly from $\sim 200 - 400$ Myr (Lee *et al.*, 2011) to ~ 1 Gyr (Oesch *et al.*, 2013) (dependent on assumptions of star-formation history).

For galaxies closer to the epoch of reionization, constraints on the Balmer/D(4000) breaks become poorer due to the fewer bands available to measure the continuum above the break, a problem which is exacerbated by the additional degeneracy of strong neb-

ular emission lines redshifted into those filters (Schaerer & deBarros, 2009, 2010). The effect of incorporating the effects of emission lines on SED fits at $z \geq 5$ is that on average the best-fitting ages and stellar masses are lowered. This is because the rest-frame optical colours can often be well fit by either a strong Balmer break or by a significantly younger stellar population with very high equivalent width H α or OIII emission.

Recent observations of galaxies at high-redshift with constraints on the UV emission-line strengths (Ly α or otherwise) have found that single-component star-formation histories are unable to adequately fit both the strong line emission and the photometry at longer wavelengths (Rodriguez Espinosa *et al.*, 2014; Stark *et al.*, 2014b). For example, in order to match both the observed photometry at rest-frame optical wavelengths and the high-equivalent width UV emission lines of a lensed galaxy at $z = 6.02$, Stark *et al.* (2014b) require two stellar populations. In combination with a ‘young’ 10 Myr old starburst component, the older stellar component is best fitted with an age since the onset of star-formation of ≈ 500 Myr.

Based on the observational constraints discussed above and the median best-fit ages found by Curtis-Lake *et al.* (2013), we choose a stellar population age (since the onset of star-formation) of 200 Myr, consistent with an onset of star-formation of $z \approx 9$ for a galaxy observed at $z = 7$.

3.3.1.5 Nebular continuum and line emission

If nebular line emission is “ubiquitous” at high-redshift as an increasing number of studies claim (e.g. Shim *et al.* (2011); Stark *et al.* (2013); Smit *et al.* (2013)), the accompanying nebular continuum emission should also have a strong effect on the observed SEDs of high-redshift galaxies (Reines *et al.*, 2009). In this work, we include both nebular continuum and optical line emission using the prescription outlined in Duncan *et al.* (2014) (and equivalent to the methods described in Ono *et al.* (2010); Schaerer & deBarros (2010); McLure *et al.* (2011)).

Whilst the strength of nebular emission in this model is directly proportional to the number of ionizing photons produced by the underlying stellar population, addition-

ally both the strength and spectral shape of the nebular continuum emission are also dependent on the continuum emission coefficient, $\gamma_\nu^{(total)}$, given by

$$\gamma_\nu^{(total)} = \gamma_\nu^{(HI)} + \gamma_\nu^{(2q)} + \gamma_\nu^{(HeI)} \frac{n(He^+)}{n(H^+)} + \gamma_\nu^{(HeII)} \frac{n(He^{++})}{n(H^+)} \quad (3.11)$$

where $\gamma_\nu^{(HI)}$, $\gamma_\nu^{(HeI)}$, $\gamma_\nu^{(HeII)}$ and $\gamma_\nu^{(2q)}$ are the continuum emission coefficients for free-free and free-bound emission by Hydrogen, neutral Helium, singly ionized Helium and two-photon emission for Hydrogen respectively (Krueger, Fritze-vAlvensleben & Loose, 1995). As in Duncan *et al.* (2014), the assumed continuum coefficients are taken from ?, assuming an electron temperature $T = 10^4$ K and electron density $n_e = 10^2$ cm⁻³ and abundance ratios of $y^+ \equiv \frac{n(He^+)}{n(H^+)} = 0.1$ and $y^{++} \equiv \frac{n(He^{++})}{n(H^+)} = 0$ (Krueger, Fritze-vAlvensleben & Loose, 1995; Ono *et al.*, 2010).

Although the exact ISM conditions and abundances of high-redshift HII regions is not well known, singly and doubly ionised helium abundances for nearby low-metallicity galaxies have been found to be $y^+ \approx 0.08$ and $y^{++} \approx 0.001$ (Dinerstein & Shields, 1986; Izotov, Thuan & Lipovetsky, 1994; Hagele *et al.*, 2006). We estimate that for the age, metallicity and dust values chosen for our fiducial model (see Table 3.1), variations of $\Delta y^+ = 0.05$ corresponds to $\Delta\beta = 0.004$, while values of y^{++} as large as 3% (Izotov, Stasińska & Guseva, 2013) would redden the observed UV slope by $\Delta\beta = +0.003$. In this case, because the nebular continuum emission is dominated by the stellar continuum at these wavelengths for our assumption, the effects of variation in the HII region properties is negligible and our interpretation of the observed UV slopes should not be affected by our assumed nebular emission properties.

3.3.1.6 Dust Extinction

In Bouwens *et al.* (2009), it is argued that the most likely physical explanation for variation in the observed β s between galaxies is through the variation in dust content. Large changes in metallicity and ages are required to produce significant variation in β (see later discussion in Section 3.3.2), however as previously discussed in this section, such large variations are not observed in the galaxy population in either age or metallicity at $z > 3$ based on current observations. For the fiducial model in our subsequent analysis, we allow the magnitude of dust extinction (A_V) to vary along

with f_{esc} , but we must also choose a dust attenuation law to apply.

Direct measurements of dust and gas at extreme redshifts are now possible thanks to the sub-mm facilities of ALMA. However, the current number of high redshift observations is still very small. Ouchi *et al.* (2013) and Ota *et al.* (2014) observe Lyman alpha emitters (LAEs) at $z \sim 7$, finding only modest dust extinction ($E(B - V) = 0.15$). Recent work by Schaefer *et al.* (2014) extends the analysis to a larger sample of five galaxies, finding a range in dust extinction of $0.1 < A_V < 0.8$. While the dust attenuation in these objects is consistent with normal extragalactic attenuation curves such as (Calzetti *et al.*, 2000) or the SMC extinction curve (e.g. Pei (1992)), the results are not strong enough to constrain or distinguish between these models. Similarly, for broadband SED fits of high-redshift objects, neither a starburst or SMC-like attenuation curve is strongly favoured (Salmon *et al.*, 2014). Based on these factors, we assume the starburst dust attenuation curve of Calzetti *et al.* (2000) in order to make consistent comparisons with the SED fitting of Duncan *et al.* (2014) and Meurer, Heckman & Calzetti (1999) dust corrections to UV star-formation rates (e.g. Bouwens *et al.* (2011a); Smit *et al.* (2012)).

In addition, due to the lack of constraints on the dust attenuation strengths at wavelengths less than 1200Å we must also assume a plausible extrapolation below these wavelengths. For our fiducial model, we simply extrapolate linearly based on the slope of the attenuation curve at 1200 – 1250Å, in line with similar works on the escape fraction of galaxies (Siana *et al.*, 2007). In addition, we also assume a second model in which the extreme-UV and Lyman continuum extinction follows the functional form of the component of the Pei (1992) SMC extinction model at $\lambda \leq 1000\text{Å}$, whereby the relative absorption begins to decrease below 800Å. The systematic effect of choosing this second assumption along with a third assumption of an SMC extinction curve are outlined in Table ??.

As shown in Fig. 3.1, we assume a simple foreground dust screen (Calzetti, Kinney & Storchi-Bergmann, 1994) and that dust destruction is minimal and/or balanced by grain production (Zafar & Watson, 2013; Rowlands *et al.*, 2014); effectively that dust for a given model is fixed with relation to the stellar population age. The assumption of a different dust geometry, such as one with clouds dispersed throughout the ISM,

would require a greater amount of dust to achieve the same optical depth and could also have a significant effect on the extinction of nebular emission relative to that of the stellar continuum (Zackrisson, Inoue & Jensen, 2013).

3.3.1.7 Differing SSP models: the effects of stellar rotation and binarity

The choice of Bruzual & Charlot (2003) stellar population synthesis (SPS) models in this work was motivated by the more direct comparison which can be made between this analysis and the stellar mass, luminosity and colour measurements based on the same models, e.g. Finkelstein *et al.* (2012b); Duncan *et al.* (2014). However, several other SPS models are available and in common usage, e.g. Starburst99 (Leitherer *et al.*, 1999), Maraston (2005) and FSPS (Conroy, Gunn & White, 2009; Conroy, White & Gunn, 2009).

Due to differences in assumptions/treatment of various ingredients such as horizontal branch morphology or thermally-pulsating asymptotic giant branch (TP-AGB) stars, the SEDs produced for the same input galaxy properties (such as age and metallicity) can vary significantly. The full systematic effects of the different assumptions and models for galaxies at high-redshift is not well quantified and adequately doing so is beyond the scope of this work. We do however caution that these systematics could significantly affect the inferred ionizing photons rates of galaxies during the EoR. In particular, it has been suggested that rotation of massive stars could have a significant effect on the UV spectra and production rate of ionizing photons (Vazquez *et al.*, 2007).

In Leitherer *et al.* (2014), the effects of the new stellar models including stellar rotation (Ekström *et al.*, 2012) are incorporated into the Starburst99 SPS model. The resulting SEDs are changed drastically with an increase in the ionizing photon rate of up to a factor of five for the most extreme model of rotation.

A second, equally significant effect comes from the inclusion of binary physics in stellar population synthesis models. It is now believed that the majority of massive stars exist in binaries (Sana *et al.*, 2012, 2013; Aldoretta *et al.*, 2014) while the majority of stellar population models (including all of the aforementioned SPS models) are for single stars. The BPASS code of Eldridge & Stanway (2009, 2011)) incorporates the

physics of binary rotation on massive stars to explore the effects on the predicted stellar population features, observing similar effects to the addition of rotation in single star models; an increased fraction of red supergiants which go on to form bluer UV bright Wolf-Rayet stars.

We note that for the same assumed stellar populations parameters (age, metallicity, SFH, dust), the use of either of these models would result in SEDs with bluer UV continuum slopes and an increased LyC production rate. However, the full ramifications of how these models may change the interpretation of SEDs, stellar masses and β s for the observations of high-redshift galaxies is beyond the scope of this work.

3.3.2 Observed UV slopes as a function of f_{esc} and dust extinction

The galaxy properties with the largest uncertainties and expected variation are the optical depth of the dust attenuation (or extinction magnitude A_V) and the property we wish to constrain photometrically, the escape fraction of ionizing photons f_{esc} . For the assumptions of our fiducial model (Table 3.1), we want to explore the possible range of these two properties which are consistent with the observed UV slopes (as calculated for each model following Eq. 3.7) and what constraints can then be placed on the ionizing emissivity coefficients $f_{esc}\xi_{ion}$ or $f_{esc}\kappa_{ion}$.

In the left panels of Fig. 3.5 and Fig. 3.6, we show how β varies as a function of the dust extinction magnitude and escape fraction for each of the continuum escape mechanisms respectively (Section 3.2/Fig. 3.1). For both models, β is relatively constant as a function of f_{esc} at low values of escape fraction ($f_{esc} < 0.1$). At larger escape fractions, the two mechanisms produce different UV slopes. For Model A, as f_{esc} increases to $\sim 10\%$ (covering fraction $\approx 90\%$) the unattenuated stellar continuum begins to dominate the overall colours as f_{esc} increases and by $f_{esc} \gtrsim 30\%$ the observed average β is determined only by the unattenuated light, irrespective of the magnitude of the dust extinction in the covered fraction. This effect is also illustrated in a different way in Figure 9 of Zackrisson, Inoue & Jensen (2013), whereby the same amount of dust extinction in the covered/high-density regions has a decreasing effect on the observed β as the escape fraction increases. This means that if Lyman continuum is escaping through holes in the ISM and is un-attenuated by dust, it is possible set constraints

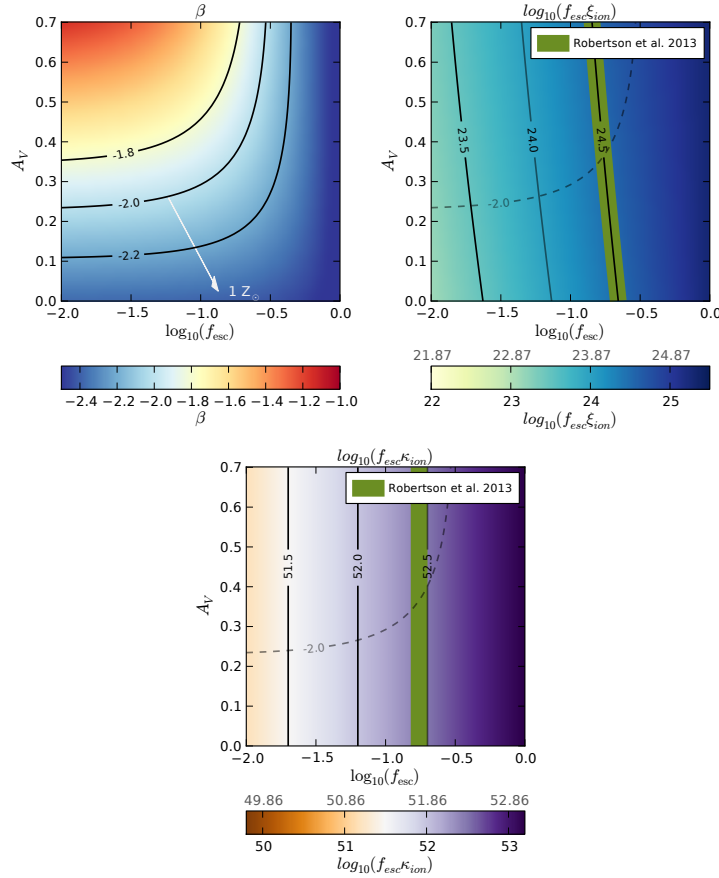


Figure 3.5: Left: UV continuum slope β as a function of total escape fraction, f_{esc} , and dust extinction, A_V , for the *ionization bounded nebula with holes* continuum escape model (Model A, Fig. 3.1 left) with stellar population properties as outlined in Section 3.3.1. The contours indicate lines of constant β around the observed average β , and the light grey arrow indicates how those contours move for a stellar population with solar metallicity. Middle and right: $\log_{10} f_{esc}\xi_{ion}$ and $\log_{10} f_{esc}\kappa_{ion}$ as a function of escape fraction and dust extinction respectively for the same continuum escape model. Solid contours represent lines of constant $f_{esc}\xi_{ion}$ and $f_{esc}\kappa_{ion}$ whilst the dashed contour shows where $\beta = -2$ is located for reference. The green labelled contour shows the assumed $f_{esc}\xi_{ion} = 24.5$ value of Robertson *et al.* (2013) and the equivalent in $f_{esc}\kappa_{ion}$ (see text for details). For the colour scales below the centre and right panels, the lower black tick labels correspond to the scale for the fiducial model ($Z = 0.2Z_\odot$) whilst the grey upper tick label indicate how $f_{esc}\xi_{ion}$ and $f_{esc}\kappa_{ion}$ change for stellar populations with solar metallicity.

on the maximum escape fraction possible which is still consistent with the UV slopes observed.

For Model B, β remains constant with $f_{esc,neb}$ at a fixed dust extinction until $f_{esc} \approx 30\%$. Beyond this, the reduction in nebular continuum emission from the high escape fraction begins to make the observed β s bluer for the same magnitude of dust extinction.

For both escape mechanisms, a UV slope of $\beta \approx -2$ is achievable with only moderate amounts of dust extinction required ($A_V \approx 0.4$ and 0.25 for models A and B respec-

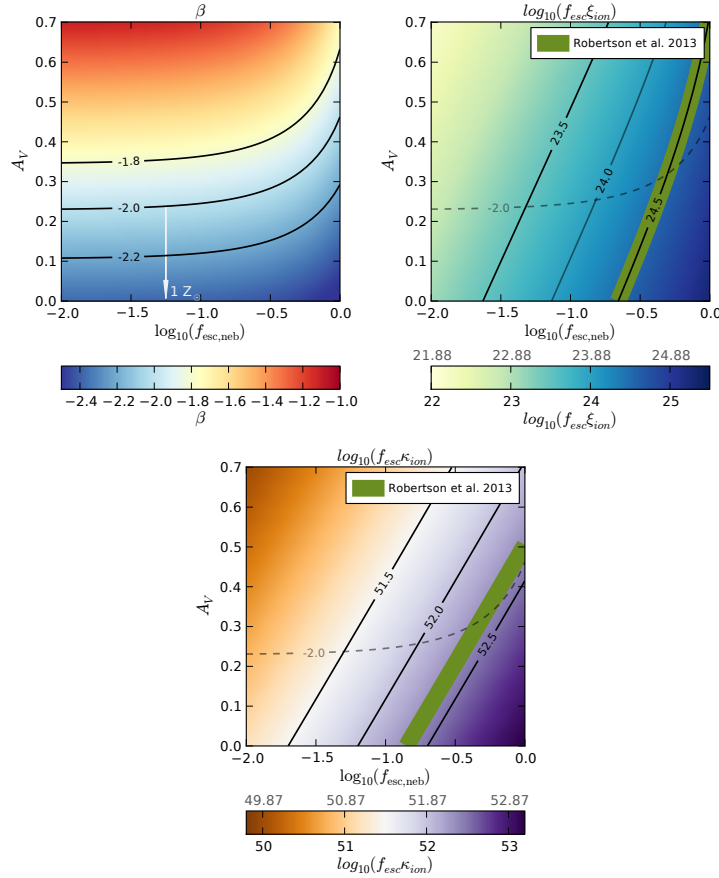


Figure 3.6: Left: UV continuum slope β as a function of HII region escape fraction, f_{esc} , and dust extinction, A_V , for the *density bounded nebula* continuum escape model (Model B, Fig. 3.1 right) with stellar population properties as outlined in Section 3.3.1. The contours indicate lines of constant β around the observed average β , and the light grey arrow indicates how those contours move for a stellar population with solar metallicity. Centre and right: $\log_{10} f_{\text{esc}}\xi_{\text{ion}}$ and $\log_{10} f_{\text{esc}}\kappa_{\text{ion}}$ (where f_{esc} is the total dust attenuated escape fraction) as a function of escape fraction and dust extinction respectively for the same continuum escape model. Solid contours represent lines of constant $f_{\text{esc}}\xi_{\text{ion}}$ and $f_{\text{esc}}\kappa_{\text{ion}}$ whilst the dashed contour shows where $\beta = -2$ is located for reference. The green labelled contour shows the assumed $f_{\text{esc}}\xi_{\text{ion}} = 24.5$ value of Robertson *et al.* (2013) and the equivalent in $f_{\text{esc}}\kappa_{\text{ion}}$ (see text for details). For the colour scales below the centre and right panels, the lower black tick labels correspond to the scale for the fiducial model ($Z = 0.2Z_\odot$) whilst the grey upper tick label indicate how $f_{\text{esc}}\xi_{\text{ion}}$ and $f_{\text{esc}}\kappa_{\text{ion}}$ change for stellar populations with solar metallicity.

tively at $f_{\text{esc}} \approx 0.2$). When metallicity is increased to $Z = Z_\odot$, the isochromes (of constant β) are shifted downwards such that $\beta \approx -2$ requires negligible dust attenuation (cf. Robertson *et al.* 2013). In Section 3.3.4 we further explore the effects of varying metallicity on the apparent β and corresponding emissivity coefficients. However, first we wish to examine the range of ξ_{ion} and κ_{ion} which correspond to the values of f_{esc} and A_V consistent with $\beta \approx -2$ found here.

3.3.3 ξ_{ion} and κ_{ion} as a function of f_{esc} and dust extinction

In the centre and right panels of Figures 3.5 and 3.6 we show $\log_{10} f_{esc}\xi_{ion}$ and $\log_{10} f_{esc}\kappa_{ion}$ as a function of f_{esc} and the extinction magnitude of dust in the covered regions (A_V).

For dust model A, the ionization bounded nebula with holes, there is very little dependence of the ionizing photon rate per unit UV luminosity on the magnitude of dust extinction in the covered fraction (centre panel). Because the increase dust extinction magnitude around the high column density areas only affects the UV/optical component, the increasing dust extinction results in higher values of $\log_{10} f_{esc}\xi_{ion}$ due to the increased absorption of the UV light in the dust covered regions. For this dust model, the corresponding ionizing photon rate per unit SFR ($f_{esc}\kappa_{ion}$) has zero evolution as a function of dust extinction in this geometry.

The assumed $\log_{10} f_{esc}\xi_{ion} = 24.5$ of Robertson *et al.* (2013) is consistent with $\beta = -2$ for this model, with an escape fraction of $f_{esc} = 0.22$ and moderate dust extinction ($A_V = 0.37$). Given the low escape fractions which are still consistent with blue β slopes, a value of $\log_{10} f_{esc}\xi_{ion} = 24.5$ does represent a relatively optimistic assumption on the ionizing efficiency of galaxies. However, it is still ≈ 0.2 dex lower than the largest f_{esc} still consistent with a UV slope of $\beta = -2$.

In contrast to model A, because the dust in the density bounded nebula (model B) is assumed to cover all angles, increases in the dust extinction magnitude results in significantly smaller $\log_{10} f_{esc}\xi_{ion}/\log_{10} f_{esc}\kappa_{ion}$ for the same fixed f_{esc} . This can be seen clearly in the centre and right panels of Fig. 3.6.

Despite this, an assumed value of $\log_{10} f_{esc}\xi_{ion} = 24.5$ is still consistent with $\beta = -2$ for this model. However, it requires a higher escape fraction ($f_{esc} = 0.6$) and lower dust extinction ($A_V = 0.3$) to achieve this for the same underlying stellar population. The maximum $f_{esc,neb} = 1$ is still consistent with the fiducial UV slope, but the increased dust required to match $\beta = -2$ means that the total LyC escape fraction is reduced and that the corresponding maximum $\log_{10} f_{esc}\xi_{ion}$ is only marginally higher than the assumptions of (Kuhlen & Faucher-Giguère, 2012) or (Robertson *et al.*, 2013).

For the assumed stellar population properties in our reference model, the UV continuum slope of the intrinsic dust-free stellar population is $\beta = -2.55$ excluding the

Star-formation history	$SFR \propto t^{1.4}$ ^a
Initial Mass Function	Chabrier (2003)
Dust attenuation curve	Calzetti <i>et al.</i> (2000)
Metallicity	$Z = 0.2Z_{\odot}$
Nebular Emission	Continuum included ^b
Age	200 Myr
	<i>Model A</i> <i>Model B</i>
Dust attenuation magnitude A_V	0.36 0.32
Escape fraction $f_{esc,neb}$	0.17 0.5
$\log_{10} f_{esc}\xi_{ion}$	24.5 ^c 24.5
$\log_{10} f_{esc}\kappa_{ion}$	52.44 52.35

Table 3.1: Summary of the stellar population model assumptions^aSalmon *et al.* (2014)^b $T = 10^4$ K, $n_e = 10^2$ cm $^{-3}$, $y^+ = 0.1$ and $y^{++} = 0$ ^cThe assumed $\log_{10} f_{esc}\xi_{ion}$ of Robertson *et al.* (2013)

contribution of nebular continuum emission. This value is significantly bluer than the dust-free β assumed by the Meurer, Heckman & Calzetti (1999) relation commonly used to correct UV star-formation rates for dust absorption. It is however in better agreement with the dust-free β 's estimated recently for observed galaxies at $z \geq 3$ (Castellano *et al.*, 2014; deBarros, Schaerer & Stark, 2014) and the theoretical predictions of Dayal & Ferrara (2012).

3.3.4 Effect of different stellar population properties on ξ_{ion} and κ_{ion} vs β

Given the strong evidence for both luminosity and redshift dependent β s, we wish to explore whether evolution in each of the stellar population parameters can account for the observed range of β s and estimate what effect such evolution would have on the inferred values of $f_{esc}\xi_{ion}$ and $f_{esc}\kappa_{ion}$. At $z > 6$, the the average β for the brightest and faintest galaxies by $\Delta\beta \approx 0.6$ (Fig. 3.2). As a function of redshift, the evolution in β is less dramatic, with average slopes (at a fixed luminosity) reddening by $\Delta\beta \approx 0.1$ in the ~ 400 million years between $z \sim 7$ and $z \sim 5$.

In the left panel of Fig. 3.7, we show how β and $f_{esc}\xi_{ion}$ or $f_{esc}\kappa_{ion}$ vary as a function of each model parameter for the ionization-bounded nebula model (Model A) with the remaining parameters kept fixed at our fiducial $\beta = -2$ model (Table 3.1). The

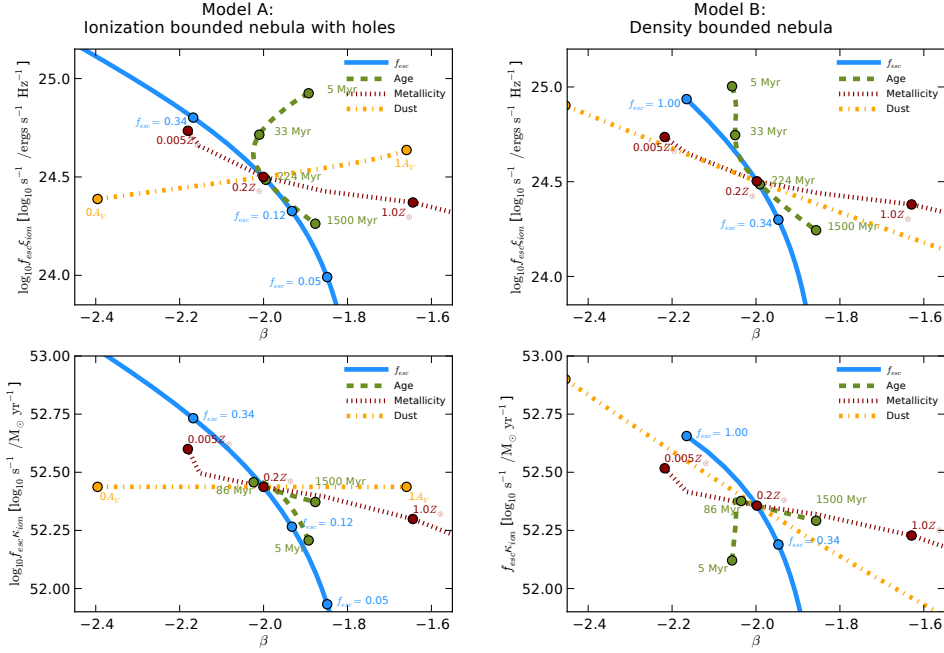


Figure 3.7: Evolution of $\log_{10} f_{esc} \xi_{ion}$ (top panels) and $\log_{10} f_{esc} \kappa_{ion}$ (bottom panels) vs β as a function of changes in the stellar population age (green dashed), metallicity (red dotted), dust extinction (yellow dot-dashed) and escape fraction (blue continuous) with the remaining parameters fixed to the fiducial values listed in Table 3.1. Values are plotted for both the ionization bounded nebula with holes (Model A; left panels) and density bounded nebula (Model B; right panels). Some individual points are labelled for both Lyman continuum escape models to illustrate the range and differences in evolution between each model. Note that the small difference in β between Model A and Model B for the case of zero-dust ($0A_V$) is due to the difference in nebular emission contribution for the two models; $f_{esc,neb} = 0.17$ and $f_{esc,neb} = 0.5$ for models A and B respectively.

corresponding values for the density bounded nebula model (Model B) are shown in the right-hand panel of Fig. 3.7. How $f_{esc}\xi_{ion}$ and $f_{esc}\kappa_{ion}$ vary with respect to β for changes in the different parameters differs significantly:

- **Dust:** As has already been seen in Fig. 3.5, β varies strongly as a function of dust attenuation strength for the ionization-bounded nebula model. There is however minimal variation in $f_{esc}\xi_{ion}$ or $f_{esc}\kappa_{ion}$ with respect to that large change in β . The inferred $f_{esc}\xi_{ion}$ or $f_{esc}\kappa_{ion}$ can justifiably be considered constant as a function of redshift for this escape model if it is assumed that evolution in the dust extinction is responsible for the observed evolution of β .

For model B, the density-bounded nebula, the large evolution in β is coupled to a significant evolution in the inferred emissivity coefficients. For a change in the UV slope of $\Delta\beta \approx 0.2$, there is a corresponding evolution in $f_{esc}\xi_{ion}$ and $f_{esc}\kappa_{ion}$ of ≈ 0.19 and 0.25 dex respectively.

- *Metallicity*: Between extremely sub-solar ($Z = 0.005 Z_{\odot}$) and super-solar ($Z > 1 Z_{\odot}$) metallicities, the variation in β is large enough to account for the wide range of observed average β 's for both Lyman escape mechanisms. In this regard, metallicity evolution is a plausible mechanism to explain the apparent variation in β . However, such a wide variation in metallicities is not supported by current observations (see Section 3.3.1.3) .

Both $f_{esc}\xi_{ion}$ and $f_{esc}\kappa_{ion}$ vary by a factor of ~ 2 across the full metallicity range modelled in this work, with bluer low-metallicity stellar populations producing more Lyman continuum photons per unit SFR/UV luminosity.

- *Age*: Due to the strong nebular continuum contribution to the overall spectra at young ages, evolution in the stellar population age results in a more complicated β -emissivity relation. When nebular emission is included the continuum emission reddens the slope at very young ages before turning over at $t \approx 100$ Myr and reddening with age towards ages of $t = 1$ Gyr and greater. For both LyC escape models, younger stellar populations results in a higher number of ionizing photons per unit UV luminosity.

For Model A, the effect of reddening by nebular emission at young ages is more pronounced due to the lower nebular region escape fraction ($f_{esc,neb} = 0.22$) in our fiducial model. The result of this reddening is that for the same $\beta = -2$, the corresponding $\log_{10} f_{esc}\xi_{ion}$ can be either ≈ 24.5 or ≈ 25.1 . This represents a potentially huge degeneracy if the ages of galaxy stellar populations are not well constrained.

- f_{esc} : For both models of LyC escape, variation in f_{esc} has a strong evolution in $f_{esc}\xi_{ion}$ or $f_{esc}\kappa_{ion}$ with respect to changes in β . However, for Model B (density bounded nebula) the range of β covered by the range of $f_{esc,neb}$ ($0 \leq f_{esc,neb} \leq 1$) is only ≈ 0.2 dex, significantly less than the range of colours reached by variation in the other stellar population parameters.

3.4 Estimated galaxy emissivity during reionization

Using our improved understanding of the ionizing efficiencies of galaxies during the EoR, we can now estimate the total ionizing emissivity \dot{N}_{ion} of the galaxy population at high redshift following the prescription outlined in Equations 3.2 and 3.3. We quantify ρ_{UV} and ρ_{SFR} using the latest available observations of the galaxy population extending deep in the epoch of reionization.

3.4.1 Observations

Thanks to the deep and wide near-infrared observations of the CANDELS survey (Grogin *et al.*, 2011; Koekemoer *et al.*, 2011) and the extremely deep but narrow UDF12 survey (Koekemoer *et al.*, 2013), there now exist direct constraints on the observed luminosity function deep into the epoch of reionization. In this paper, we will make use of the UV luminosity functions calculated by McLure *et al.* (2013) and Schenker *et al.* (2013b) at $z = 7 - 9$ as part of the UDF12 survey along with the recent results of Bouwens *et al.* (2014b) and (Finkelstein *et al.*, 2014) at $z \geq 4$ and the latest results from lensing clusters at $z > 8$ (Oesch *et al.*, 2014; McLeod *et al.*, 2014).

A second, complimentary constraint on the amount of star-formation at high redshift is the stellar mass function and the integrated stellar mass density observed in subsequent epochs. As the time integral of all past star-formation, the stellar mass density can in principal be used to constrain the past star-formation rate if the star-formation history is known (Stark *et al.*, 2007). A potential advantage of using the star-formation rate density in this manner is that by being able to probe further down the mass function, it may be possible to indirectly measure more star-formation than is directly observable at higher redshifts. Or to outline in other terms, if the total stellar mass density of all galaxies can be well known at $z \sim 4$ or $z \sim 5$, strict upper limits can be placed on the amount of unobserved (e.g. below the limiting depth of $z \sim 8$ observations) or obscured star-formation at $z > 6$.

At its simplest, the relation between a star-formation history, $S(t)$, and the resulting

stellar mass M_* (or stellar mass density ρ_*) is given by

$$M_*(t_z) = (1 - \epsilon_z) \times \int_{t_f}^{t_z} S(t) dt \quad (3.12)$$

where t_f and t_z are the age of the Universe at the onset of star-formation and observed redshift respectively and ϵ_z is the fraction of mass returned to the ISM at the observed redshift. For a parametrised star-formation history, $F(t)$, which is normalised such that $\int_{t_f}^{t_z} F(t) dt = 1 M_\odot (\text{Mpc}^{-3})$, we can substitute $S(t) = C_{obs,z} \times F(t)$. The normalisation, $C_{obs,z}$, accounts for the normalisation of the star-formation history required to match the observed stellar mass (or stellar mass density) at the redshift z .

From recent observations of the stellar-mass density at $z > 4$, such as those from the stellar mass functions presented in Duncan *et al.* (2014) and Grazian *et al.* (2014), it is then straight-forward to calculate the corresponding $C_{obs,z}$ and the inferred star-formation history ($C_{obs,z} \times F(t)$) for any assumed parametrisation. Motivated by the discussion of star-formation histories in Section 3.3.1, we assume a normalised star-formation history which is $F(t) \propto t^{1.4}$ (Salmon *et al.*, 2014), as is done for the modelled β values.

Using our stellar population models, we calculate ϵ for the star-formation history and metallicity used in this work at any desired redshift. We find that for a Chabrier (2003) IMF, ϵ_z varies from $\epsilon_z \approx 0.29$ at $z = 8$ to $\epsilon_z \approx 0.35$ at $z = 4$ (for a Salpeter IMF and constant SFH at ~ 10 Gyr old, we calculate $\epsilon = 0.279$ in agreement with the figure stated in Robertson *et al.* (2013)).

3.4.2 \dot{N}_{ion} for constant $f_{esc}\xi_{ion}$ and $f_{esc}\kappa_{ion}$

In Fig. 3.8, we show the estimated ionizing emissivity as a function of redshift for UV luminosity function observations of Bouwens *et al.* (2014b); Finkelstein *et al.* (2014); Oesch *et al.* (2014) and McLeod *et al.* (2014), assuming our fiducial constant $\log_{10} f_{esc}\xi_{ion} = 24.5$ (Table 3.1, as assumed in Robertson *et al.*, 2013). The integrated luminosity density and corresponding confidence intervals for each UV LF observation are estimated by drawing a set of LF parameters from the corresponding MCMC chain or likelihood distribution obtained in their fitting. This is repeated 10^4 times to give a distribution from which we plot the median and 68% confidence interval. The

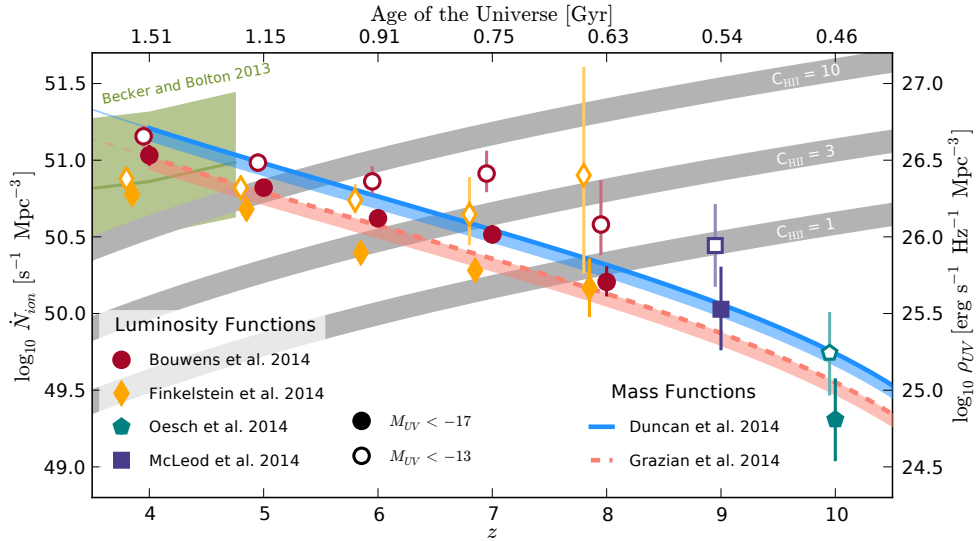


Figure 3.8: Ionizing emissivity \dot{N}_{ion} predicted for a fixed $f_{esc}\xi_{ion}$ for the UV luminosity function observations of Bouwens *et al.* (2014b), Oesch *et al.* (2014), Finkelstein *et al.* (2014) and McLeod *et al.* (2014). Filled symbols are for luminosity functions integrated down to $M_{UV} = -17$ (typical limiting depth of while open symbols correspond to a UV luminosity density integrated down to a constant $M_{UV} = -13$ for all redshifts. Also shown are the ionizing emissivities inferred by the $z \sim 4$ stellar mass density observations of Duncan *et al.* (2014) (solid blue line) and Grazian *et al.* (2014) (dashed pink line) for the power-law star-formation history outlined in Section 3.3.1. For the stellar mass function predictions, the thick solid and dashed line correspond to a constant $\log_{10} f_{esc}\kappa_{ion} = 54.44$ (Lyman escape model A) while the filled region shows the systematic offset when assuming $\log_{10} f_{esc}\kappa_{ion} = 54.35$ for Lyman escape model B, see the text for details. At lower redshifts, we show the IGM emissivity measurements and corresponding total errors of Becker & Bolton (2013) (green line and filled region respectively). The ionizing emissivity required to maintain reionization as a function of redshift and clumping factors (C_{HII}) of one, three and ten are shown by the wide grey regions (Madau, Haardt & Rees 1999, also see Equation 18 of Bolton & Haehnelt 2007).

luminosity functions of Bouwens *et al.* (2014b) and Finkelstein *et al.* (2014) span a large redshift range from $z \sim 4$ to $z \sim 8$ and predominantly make use of the same imaging data (including the ultra deep UDF12 observations Koekemoer *et al.* 2013) but use different reductions of said data and differing selection and detection criteria, we refer the reader to the respective papers for more details.

Also shown are the current constraints at $z \sim 10$ based on the luminosity function from Oesch *et al.* (2014). Due to the small number of sources available at $z \sim 10$ and the very large uncertainty in their redshift, the luminosity function is not well constrained at these redshifts. Fits using the Schechter (1976) parametrisation realistically allows only one free parameter to be varied while the remainder are fixed to their $z \sim 8$ values (we plot the \dot{N}_{ion} predicted for the luminosity function parameters where ϕ_* is allowed to vary). Despite the large uncertainty, we include these values to illustrate the early suggestions of Oesch *et al.* (2014) and other works (Zheng *et al.*, 2012; Coe *et al.*,

2012) that the luminosity function (and hence the inferred underlying star-formation rate density) begins to fall more rapidly at $z \geq 9$ than extrapolations from lower redshift naively suggest. However, more recent analysis by McLeod *et al.* (2014) of existing Frontier Fields data is in better agreement with the predicted luminosity density at $z \approx 9$. Completed observations of all six Frontier Fields clusters should provide significantly improved constraints at $z > 9$ (Coe, Bradley & Zitrin, 2014), although the large cosmic variance of samples due to the volume effects of strong lensing will limit the constraints that can be placed at the highest redshifts (Robertson *et al.*, 2014).

For all redshift samples plotted in Fig. 3.8, filled symbols correspond to the UV luminosity density integrated to $M_{UV} = -17$ and $M_{UV} = -13$ respectively. The predicted \dot{N}_{ion} for the UV luminosity functions of Schenker *et al.* (2013b) and McLure *et al.* (2013) (not shown in Fig. 3.8) effectively reproduce the UV luminosity density constraints outlined in Robertson *et al.* (2013) and lie between those predicted by Bouwens *et al.* (2014b) and Finkelstein *et al.* (2014). The more recent works of Bouwens *et al.* (2014b) and Finkelstein *et al.* (2014) show a greater disagreement between both themselves and previous works. This is a concern as it means that the choice of luminosity function (and hence the underlying selection/methodology) could have a significant effect on the conclusions drawn on galaxies' ability to complete or maintain reionization by the desired redshift.

At $z \sim 6$, the UV luminosity density from galaxies brighter than the limiting depth observed by Bouwens *et al.* (2014b) is large enough to maintain reionization for a clumping factor of three. This is in contrast to the previous LF of Bouwens *et al.* (2012b) and the results of Finkelstein *et al.* (2014) which require a contribution from galaxies fainter than $M_{UV} = -17$ (approximately the observational limits) to produce the \dot{N}_{ion} needed to maintain reionization. At $z \sim 8$, the large uncertainties (and fitting degeneracies) in both the faint-end slope and characteristic luminosity of the luminosity function means that both of the luminosity density (and hence \dot{N}_{ion}) assuming a constant $f_{esc}\xi_{ion}$ estimates included in this work agree within their 1σ errors.

To convert the star-formation rates inferred by the stellar mass densities observed by Duncan *et al.* (2014) and Grazian *et al.* (2014) to an \dot{N}_{ion} directly comparable with the LF estimates, we choose the $f_{esc}\kappa_{ion}$ at the $\log_{10}f_{esc} - A_V$ values where

$\beta = -2$ and $\log_{10} f_{esc}\xi_{ion} = 24.5$. For the ionization bounded nebula with holes model, the corresponding $\log_{10} f_{esc}\kappa_{ion} = 52.44$, whilst for the density bounded nebula $\log_{10} f_{esc}\kappa_{ion} = 52.35$.

The ionizing photon rate predicted by the $z \sim 4$ stellar mass functions of Duncan *et al.* (2014) and Grazian *et al.* (2014) for stellar masses greater than $10^{8.55} M_\odot$ (the estimated lower limit from (Duncan *et al.*, 2014) for which stellar masses can be reliably measured at $z \sim 4$) are shown as the blue and pink lines plotted in Fig. 3.8. Plotted as thick solid and dashed lines are the \dot{N}_{ion} assuming $\log_{10} f_{esc}\kappa_{ion} = 52.44$ with the corresponding shaded area illustrating the systematic offset for $\log_{10} f_{esc}\kappa_{ion} = 52.35$.

The UV luminosity density at $z > 4$ implied by the SMD observations of Grazian *et al.* (2014) (for $M > 10^{8.55} M_\odot$) are in excellent agreement with the UV LF estimates of Bouwens *et al.* (2014b) when integrated down to $M_{UV} = -17$ (\approx observation limits). However, when integrating the stellar mass function down to significantly lower masses such as $> 10^7 M_\odot$, the shallower low-mass slope of (Grazian *et al.*, 2014) results in a negligible increase in the total stellar mass density (≈ 0.07 dex). This is potentially inconsistent with the star-formation (and resulting stellar mass density) implied when galaxies from below the current observations limits of the luminosity functions are taken into account (open plotted symbols).

However, comparison of the star-formation history implied by the Grazian *et al.* (2014) total stellar mass density and that of the Finkelstein *et al.* (2014) luminosity functions are slightly more consistent. The higher stellar mass density observed by Duncan *et al.* (2014) results in \dot{N}_{ion} most consistent with those inferred by the Bouwens *et al.* (2014b) total luminosity density ($M_{UV} > -13$).

One conclusion we are able to draw is that the observational limits of the stellar mass function at $z < 6$ effectively allows us to probe star-formation rate density of fainter galaxies than those which can currently be observed in-situ SF at $z \sim 8$. Improved constraints on the stellar mass functions at $z \leq 6$ are therefore a viable way of improving the SFR density constraints at higher redshifts.

3.4.3 \dot{N}_{ion} for evolving $f_{esc}\xi_{ion}$ and $f_{esc}\kappa_{ion}$

To estimate what effect a β dependent $f_{esc}\xi_{ion}$ or $f_{esc}\kappa_{ion}$ would have on the predicted \dot{N}_{ion} , we assume two separate $f_{esc}\xi_{ion}(\beta)$ relations based on the predicted evolution of $f_{esc}\xi_{ion}$ and $f_{esc}\kappa_{ion}$ vs β shown in Fig. 3.7. The first relation, ‘*ModelB_dust*’, is based on the relatively shallow evolution of $f_{esc}\xi_{ion}$ and $f_{esc}\kappa_{ion}$ vs β as a function of dust extinction for the density-bounded nebula model (Model B). Over the dynamic range in β , the *ModelB_dust* model evolves $\approx 0.5\text{dex}$ from $\log_{10} f_{esc}\xi_{ion}(\beta = -2.3) \approx 24.75$ to $\log_{10} f_{esc}\xi_{ion}(\beta = -1.7) \approx 24.25$.

The second relation, *ModelA_fesc*, follows the $f_{esc}\xi_{ion}$ or $f_{esc}\kappa_{ion}$ vs β evolution as a function of f_{esc} for the ionization bounded nebula model (Model A). This model evolves from $\log_{10} f_{esc}\xi_{ion} \approx 25$ at $\beta = -2.3$ to effectively zero ionizing photons per unit luminosity/star-formation at $\beta = -1.7$. Due to the lack of constraints on β for galaxies all the way down to $M_{UV} = -13$, we set a lower limit on how steep the UV slope can become. This limit is chosen to match the UV slope for the dust-free, $f_{esc} = 1$ scenario for fiducial model and has a slope of $\beta = -2.55$. We choose these two relations (three including the constant assumption above) because they correspond to the most likely mechanisms through which β or the LyC escape fraction are expected to evolve.

Firstly, the constant (equivalent to ‘*ModelA_dust*’) and ‘*ModelB_dust*’ models cover the assumption that evolution in the dust content of galaxies is responsible for the observed evolution in β and any corresponding evolution in the ionizing efficiency of galaxies ($f_{esc}\xi_{ion}$ or $f_{esc}\kappa_{ion}$). Secondly, the ‘*ModelA_fesc*’ model corresponds to an evolution in f_{esc} alone and for the ionization-bounded nebula with holes model, represents the steepest evolution of $f_{esc}\xi_{ion}/\kappa_{ion}$ with respect to β of any of the parameters. While there is no obvious physical mechanism for such evolution at high-redshift, using this model we can at least link an inferred f_{esc} redshift evolution such as that from the Kuhlen & Faucher-Giguère (2012) and Robertson *et al.* (2013) to a corresponding evolution in β and vice-versa. In these works, the evolving escape fraction is parametrised as:

$$f_{esc}(z) = f_0 \times \left(\frac{1+z}{5} \right)^\gamma \quad (3.13)$$

where $f_0 = 0.054$ and $\gamma = 2.4$ (Robertson *et al.*, 2013) and are constrained by the

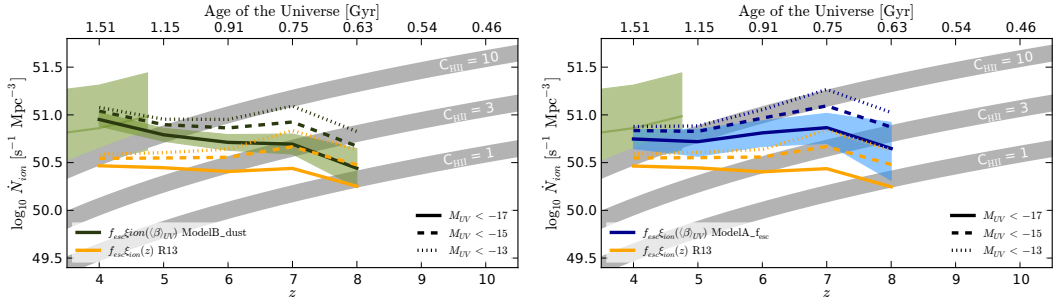


Figure 3.9: Ionizing emissivity, \dot{N}_{ion} , predicted by the luminosity functions measured by Bouwens *et al.* (2014b) for an evolving $f_{esc}\xi_{ion}$ as a function of redshift, based on the luminosity weighted average β . See text for details on the assumed $f_{esc}\xi_{ion}$ as a function of $\langle\beta\rangle_{UV}$ for the *ModelB_dust* (top) and *ModelA_fesc* (bottom) models. In both panels, the thick solid and dashed lines correspond to the UV luminosity density integrated down to the observational limit and a constant $M_{UV} = -13$ respectively.

observed IGM emissivity values of Faucher-Giguère *et al.* (2008) at $z \leq 4$ and the WMAP total integrated optical depth measurements of Hinshaw *et al.* (2013) at higher redshift. For the subsequent analysis we also show how the total ionizing emissivity would change following this evolution of f_{esc} (assuming a constant $\xi_{ion} = 25.2$ in line with Robertson *et al.* (2013)).

It is important to note here that the more recent measurements of the IGM emissivity at $z \sim 4$ by Becker & Bolton (2013) are a factor ~ 2 greater than those of Faucher-Giguère *et al.* (2008) at the same redshift. As such, the assumed values may under-estimate the zero-point f_0 and over-estimate the slope of the f_{esc} evolution compared to those fitted to the IGM emissivities of Becker & Bolton (2013). However, we include this to illustrate the effects that forcing consistency with IGM and optical depth measurements has on total ionizing emissivity for comparable underlying UV luminosity/star-formation rate density measurements relative to the assumption of a constant conversion.

3.4.3.1 Evolving constant with redshift

To explore how a β dependent coefficient would change the inferred emissivities, we first calculate a constant $f_{esc}\xi_{ion}/\kappa_{ion}$ for each redshift based on the luminosity weighted $\langle\beta\rangle_{UV}$. The $z \sim 4$ to $z \sim 7$ $\langle\beta\rangle_{UV}$ used are those from Bouwens *et al.* (2014a), with the $z \sim 8$ value based on the fit outlined in Equation 3.6.

For clarity, we plot the resulting predicted emissivities only for the UV luminosity

densities predicted by Bouwens *et al.* (2014b) luminosity function parametrisations, these are shown in Fig. 3.9 for both the *ModelB_dust* and *ModelA_fesc* (top and bottom panels respectively) $f_{esc\xi ion}(\beta)$ relations. In both plots, the thin maroon dotted and dot-dashed lines (for $M_{UV} < Obs.limit$ and $M_{UV} \leq -13$ respectively) illustrate the equivalent constant $f_{esc\xi ion} = 24.5$ assumption shown in Fig. 3.8 for comparison. The shaded regions around the solid green and blue lines (top and bottom panels respectively) represent the uncertainty on $f_{esc\xi ion}$ due to the statistical uncertainty in $\langle\beta\rangle_{UV}$. The full statistical uncertainties include the luminosity density errors illustrated in Fig. 3.8 and are included in the Appendix Table 3.1.

By assuming a β dependent coefficient, the estimated \dot{N}_{ion} evolution changes shape to a much shallower evolution with redshift. For our *ModelB_dust* β relation, the decline in \dot{N}_{ion} from $z = 4$ to $z = 8$ is reduced by ≈ 0.25 dex when the luminosity function is integrated down to the limit of $M_{UV} < -13$. The effect is even stronger for the *ModelA_fesc* β evolution, with the \dot{N}_{ion} actually increasing over this redshift. The larger $f_{esc\xi ion}$ inferred by the increasingly blue UV slopes at high redshift are able to balance the rapid decrease in UV luminosity density.

A key effect of the increasing ionizing efficiency with increasing redshifts is that for both $f_{esc\xi ion}(\beta)$ relations explored here, the observable galaxy population at $z \sim 7$ is now capable of maintaining reionization for a clumping factor of $C_{HII} = 3$. This is in contrast to the result inferred when assuming a constant $f_{esc\xi ion}$.

However, we know the brightest galaxies are in fact also the reddest and that any of our predicted $f_{esc\xi ion}(\beta)$ relations imply they are therefore the least efficient at producing ionizing photons. The application of an average $f_{esc\xi ion}$ (even one weighted by the relative contributions to the luminosity density) may give a misleading impression of the relative contribution the brightest galaxies make to the ionizing background during the EoR. A more accurate picture can be obtained by applying a luminosity dependent β relation (e.g. $f_{esc\xi ion}(M_{UV})$) to observed luminosity function and integrating the ionizing emissivity, \dot{N}_{ion} , from this.

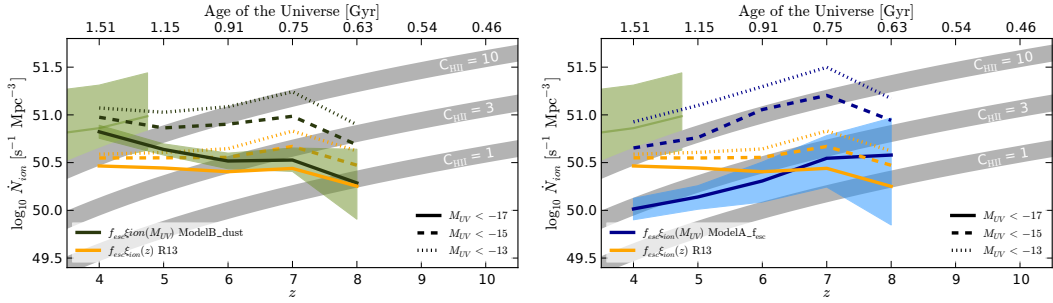


Figure 3.10: Ionizing emissivity, \dot{N}_{ion} , predicted by the luminosity functions measured by Bouwens *et al.* (2014b) for a luminosity dependent $f_{esc}\xi_{ion}$. See text for details on the assumed $f_{esc}\xi_{ion}$ as a function of $\beta(M_{UV})$ for the *ModelB_dust*(top) and *ModelA_fesc* (bottom) models. In both panels, the thick solid, dashed and dotted lines correspond to the UV luminosity density integrated down to $M_{UV} = -17, -15$ and -13 respectively.

3.4.3.2 Luminosity dependent $f_{esc}\xi_{ion}$

Using the observed $\beta(M_{UV})$ relations of Bouwens *et al.* (2014a) (Fig. 3.3) and our models for $f_{esc}\xi_{ion}(\beta)$, we next calculate \dot{N}_{ion} a function of both the changing luminosity function and the evolving colour magnitude relation.

Fig. 3.10 shows the evolution of \dot{N}_{ion} based on these assumptions, again for the Bouwens *et al.* (2014b) luminosity function parametrisations. For both the *ModelB_dust* and *ModelA_fesc* relations, the emissivity of galaxies above the limiting depths of the observations are reduced due to the fact that the brighter galaxies have significantly redder observed β s. In the case of the *ModelA_fesc* β evolution and the *ModelB_dust* relation at high redshift, the difference between the \dot{N}_{ion} for $M_{UV} < -17$ and $M_{UV} \leq -13$ is quite significant. This is due to the observed steepening of the colour-magnitude relation (Section 3.2.3) at higher redshifts results in a larger $f_{esc}\xi_{ion}$ evolution between the brightest and faintest galaxies in the luminosity function. When integrating the UV luminosity function from fainter magnitudes, the number of ionizing photons produced per unit UV luminosity density significantly increases.

The total galaxy ionizing emissivity ($M_{UV} < -13$) for both models of β evolution is high enough to maintain reionization (for a clumping factor of $C_{HII} \lesssim 3$) at all redshifts. In fact, only galaxies down to a rest-frame magnitude of $M_{UV} = -15$ are required to match these rates. Furthermore, despite the increased \dot{N}_{ion} predicted at $z > 5$ both models are in good agreement with the observed IGM emissivities of Becker & Bolton (2013) at lower redshifts when the luminosity functions are integrated down to a limit of $M_{UV} < -13$.

From these results we can see that changes in the ionizing efficiency of galaxies during EoR which are still consistent with the evolving UV continuum slopes have significantly less effect on the predicted total ionizing emissivity at $z \sim 4$ than at higher redshifts based on the current observations. This is a crucial outcome with regards to current numerical models for the epoch of reionization as it allows for a wider range of reionization histories which are still consistent with both the observed UV luminosity/SFR-density and IGM emissivity estimates.

3.5 Discussion and future prospects

In several previous studies of the reionization history of the Universe the conclusion has been drawn that at earlier times in the epoch of reionization, galaxies must have been more efficient at ionizing the surrounding IGM than similar galaxies at lower redshift (Becker & Bolton, 2013; Kuhlen & Faucher-Giguère, 2012; Robertson *et al.*, 2013). Based on the constraints on galaxy stellar populations and escape fractions explored in Section 3.3 and their application to the existing observations in Section 3.4, it is not yet possible to establish that one particular galaxy property is evolving to cause such an increase in ionizing efficiency.

However, what we find in this work is that evolution in galaxy properties, such as dust extinction and escape fraction (or some combination of these and others), which are consistent with the observed colour evolution of high-redshift galaxies can readily account for any increase in the ionizing efficiency required by other constraints such as the total optical depth. Ongoing and future observations of both local and distant galaxies will be able to provide much tighter constraints on the evolving galaxy properties.

If the observed β evolution is a result of dust alone, as is assumed by Bouwens *et al.* (2012a) and other works, the inferred evolution in $f_{esc}\xi_{ion}$ as a function of β is highly dependent on the assumed model of Lyman continuum escape and hence the underlying geometry of dust and gas. For example, if the channels through which LyC photons escape are dust-free (as in Model A), the effect of the dust evolution will have negligible effect on the emissivity of galaxies as a function of β (as discussed in Sec-

tion 3.3.4). Real galaxies will of course be significantly more complicated (and messy) than the simple toy models adopted in this work, as such the channels through which LyC escape may also contain significant quantities of dust. We find that if we modify Model A such that the dust screen is extended to include the low-density channels, the resulting model is indistinguishable from Model B (density bounded nebula) with regards to β as a function of f_{esc} or A_V . Such a model closely matches that observed by Borthakur *et al.* (2014) (see also (Heckman *et al.*, 2011)) for a local analog of galaxies during the EoR and represents our best model for LyC escape.

For any of the plausible causes for the luminosity and redshift evolution of β (dust, metallicity, escape fraction), the models explored in this work infer that fainter/low-mass galaxies are emitting more ionizing photons per unit star-formation into the IGM than their higher mass counterparts. Currently, simulations of galaxies at high redshift draw somewhat differing conclusions on the mass/luminosity dependence of the escape fraction. Based on a combination of theoretical models and the existing limited observations, Gnedin, Kravtsov & Chen (2008) find that angular averaged escape fraction increases with higher star-formation rates and galaxy masses, the inverse of what we predict based on β alone. However, in isolation from the model predictions, the observational data explored by Gnedin, Kravtsov & Chen (2008) does not place any strong constraints on the luminosity dependence of f_{esc} (Giallongo *et al.*, 2002; Fernández-Soto, Lanzetta & Chen, 2003; Shapley *et al.*, 2006).

Subsequent simulations predict the opposite luminosity dependence, in better agreement with the colour evolution predictions of this work (Razoumov & Sommer-Larsen, 2010; Yajima, Choi & Nagamine, 2010). Recent work exploring the escape fraction of both typical (Kimm & Cen, 2014) and dwarf (Wise *et al.*, 2014) galaxies at $z \geq 7$ find that the instantaneous escape fraction (measured at the virial radius in these simulations) is inversely proportional to the halo mass. However, as discussed by Kimm & Cen (2014), the average instantaneous escape fraction may be somewhat misleading due to the bursty nature of star-formation in their models and the delay between the peak SFR and maximum escape fraction for an episode of star-formation. They find that the time-averaged escape fraction weighted by the overall LyC photon production rate remains roughly constant for size haloes. Improved measurements on the stellar

or halo mass dependence of f_{esc} are therefore clearly crucial.

Although direct measurements of the LyC escape fraction for galaxies during EoR will never be possible due to the effects of IGM absorption along the line of sight, measurements of the escape fraction as a function of stellar mass and luminosity (/SFR) at $z \lesssim 3$ should soon be possible due to the deep UV imaging of new surveys such as the UVUDF (Teplitz *et al.*, 2013) and the forthcoming GOODS UV Legacy Survey (PI: Oesch, GO13872). The wealth of ancillary data available in these fields (both photometric and spectroscopic) should make it possible to tightly constrain f_{esc} , ξ_{ion} or κ_{ion} , and β for either individual galaxies or samples stacked by galaxy properties. Measuring β vs $f_{esc}\xi_{ion}$ at $2 \lesssim z \lesssim 3$ would significantly reduce systematic errors in the inferred \dot{N}_{ion} during the EoR from incorrect or poorly informed assumptions on $f_{esc}\xi_{ion}$.

Given the large degeneracies in β with respect to the various stellar population parameters, understanding β vs $f_{esc}\xi_{ion}$ both at $z \sim 3$ and during the EoR will require an improved understanding of what is responsible for the observed β evolution. With ALMA observations of statistically significant samples of galaxies at high-redshift, it should be possible to make strong constraints on not just the strength and attenuation curve of the dust extinction, but also the location and geometry of the dust relative to the gas and star-formation within galaxies (De Breuck *et al.*, 2014).

With the new generation of near-infrared sensitive spectrographs allowing precision spectroscopic measurement of metallicities and dust out to $z > 3$ (e.g. MOSFIRE: Kriek *et al.* (2014)), it will be possible to place much more accurate priors on the expected ages, metallicities and star-formation histories for galaxies during the EoR. Finally, as with many outstanding problems in astrophysics, the launch of the James Webb Space Telescope will address many of the systematic and statistical uncertainties which limit current observations. Crucially, JWST should be able to probe much fainter galaxy populations, potentially down to rest-frame magnitudes of $M_{UV} = -15$ and below. Based on the findings in this paper, such observations might even mean we are finally able to observe the full galaxy population responsible for powering reionization.

3.6 Summary

In this work, we explore in-depth the ionizing photon budget of galaxies during the epoch of reionization based solely on the observed galaxy properties. For the latest observational constraints on the star-formation rate and UV luminosity density at $z > 4$, we assess the ionizing emissivity consistent with new constraints on the rest-frame UV colours of galaxies at these redshifts.

Using a comprehensive set of SED models for two plausible Lyman continuum escape mechanisms – previously outlined in Zackrisson, Inoue & Jensen (2013) – we explore in detail the relationship between the UV continuum slope β and the number of ionizing photons produced per unit UV luminosity or star-formation (ξ_{ion} and κ_{ion} respectively). We find that the ionizing efficiencies assumed by several previous works ($\log_{10} f_{esc}\xi_{ion} = 24.5 - 24.6$: Robertson *et al.* (2013); Kuhlen & Faucher-Giguère (2012)) are still consistent with the current β observations during the EoR. However, for both of the LyC escape models explored here, this assumption is close to the maximum efficiency which is still consistent with the fiducial UV slope typically considered at these redshifts ($\beta = -2$). Based on our SED modelling, escape fractions or ionizing efficiency which are 1dex lower than typically assumed are still consistent with the observed galaxy colours.

Applying the fiducial $\log_{10} f_{esc}\xi_{ion} = 24.5$ to the the latest observations of the luminosity and mass functions at $z \geq 4$, we find that at $z \sim 6$, the observed population can produce enough ionizing photons to maintain reionization assuming a clumping factor $C_{\text{HII}} = 3$. At earlier times, we confirm earlier results which found that galaxies from below our current observation limits are required to produce enough ionizing photons to maintain reionization at $z \sim 7$ and beyond.

Motivated by a confirmed luminosity dependence of the the UV continuum slope and evidence for evolution in this relation with redshift (Bouwens *et al.*, 2014a; Rogers *et al.*, 2014), we explore the effects of assuming an ionizing efficiency which is not constant but varies with the observed β . The two galaxy properties that are able to plausibly account for the required range of observed β 's, dust extinction and f_{esc} , both predict an ionizing efficiency which increases for increasingly blue UV continuum

slopes. While the other galaxy properties such as age and metallicity predict similar trends, current observations do not support a large enough variation to account for the required range of observed UV slopes.

We find that when assuming an ionizing efficiency based on the luminosity-weighted average β , the currently observable galaxy population alone is now able to maintain reionization at $z \sim 7$ (assuming $C_{\text{HII}} = 3$). Despite this increase in efficiency at early times, the predicted \dot{N}_{ion} at $z < 5$ remain consistent with measurements based on the IGM.

Assuming instead that the ionizing efficiency of galaxies is dependent on their luminosity, the observed $M_{UV} - \beta$ relations and our SED models can result in significant changes in the inferred ionizing photon budget. Since our models suggest that redder (brighter) galaxies have lower $f_{esc}\xi_{ion}$ than their blue faint counterparts, the inferred ionizing photon budget for the currently observable galaxy population may be significantly reduced, especially at lower redshifts. However, because of the increasing importance of faint galaxies (which have higher inferred $f_{esc}\xi_{ion}$), only galaxies down to $M_{UV} \approx -15$ may be required to produce the required ionizing photons.

Our conclusion is that the inferred ability of galaxies to complete or maintain reionization is highly dependent on the stellar population assumptions used to predict their ionizing efficiencies. Crucially though, the models explored in this study can potentially allow for a wide range of reionization histories whilst remaining consistent with the observed colour evolution and luminosity (or star-formation rate) density during this epoch. Future work on constraining both the colour and luminosity dependence of f_{esc} at lower redshifts as well as measuring the ages and dust content of galaxies during the EoR will be vital in understanding the precise ionizing emissivity of galaxies throughout this epoch.

Acknowledgements

The authors thank James Bolton for considerable help and feedback throughout the writing process. We are very grateful to Rychard Bouwens and Steven Finkelstein for sharing the fitting data for their luminosity functions. We would also like to ac-

knowledge funding from the Science and Technology Facilities Council (STFC) and the Leverhulme Trust.

Appendices

Appendix A

Reionization Data Tables

In this appendix we present the estimated ρ_{UV} and \dot{N}_{ion} at $4 \leq z \leq 8$ for the range of assumptions outlined in Section 3.4. we list the calculated properties for integration limits $M_{UV} = -17, -15$ and -13 respectively. In Table ?? we list the values based on the luminosity function parametrisations of Bouwens *et al.* (2014b) and are plotted in Figures 3.8, 3.9 and 3.10. In Table ??, we list the corresponding values for the luminosity function parametrisations of (Finkelstein *et al.*, 2014). For both sets of values, we include errors based on the uncertainties in the luminosity function parameters and the random errors in the weighted average of β or the best-fit $\beta - M_{UV}$ slope parameters (Bouwens *et al.*, 2014a) as appropriate.

Table A.1: Calculated values of ρ_{UV} and \dot{N}_{ion} for the different integration limits and efficiency assumptions explored in the paper, based on the luminosity function parametrisations of Bouwens *et al.* (2014b). For each calculated value, we include statistical errors from the uncertainties in the Schechter (1976) parameters and β observations. Also shown are the effects of some of the assumptions made in Section 3.3.1 and their corresponding systematic changes to the estimated values.

Limit (M_{UV})		$z \sim 4$	$z \sim 5$	$z \sim 6$	$z \sim 7$
$\log_{10} \rho_{UV}$ (erg s ⁻¹ Hz ⁻¹ Mpc ⁻³)	-17	$26.53^{+0.07}_{-0.07}$	$26.32^{+0.05}_{-0.05}$	$26.12^{+0.06}_{-0.06}$	$26.02^{+0.06}_{-0.06}$
	-15	$26.62^{+0.07}_{-0.07}$	$26.43^{+0.06}_{-0.06}$	$26.27^{+0.07}_{-0.07}$	$26.25^{+0.10}_{-0.08}$
	-13	$26.66^{+0.07}_{-0.07}$	$26.48^{+0.06}_{-0.06}$	$26.36^{+0.10}_{-0.08}$	$26.41^{+0.15}_{-0.12}$
$\log_{10} f_{esc} \xi_{ion} = 24.5$					
$\log_{10} \dot{N}_{ion}$ (s ⁻¹ Mpc ⁻³)	-17	$51.03^{+0.07}_{-0.07}$	$50.82^{+0.05}_{-0.05}$	$50.62^{+0.06}_{-0.06}$	$50.52^{+0.06}_{-0.06}$
	-15	$51.12^{+0.07}_{-0.07}$	$50.93^{+0.06}_{-0.06}$	$50.77^{+0.07}_{-0.07}$	$50.75^{+0.10}_{-0.08}$
	-13	$51.16^{+0.07}_{-0.07}$	$50.98^{+0.06}_{-0.06}$	$50.86^{+0.10}_{-0.08}$	$50.91^{+0.15}_{-0.12}$
$\log_{10} f_{esc} \xi_{ion} \propto \langle \beta \rangle_{\rho_{UV}} (z)$					
$\log_{10} \dot{N}_{ion}$ (s ⁻¹ Mpc ⁻³)	-17	$50.95^{+0.07}_{-0.07}$	$50.79^{+0.07}_{-0.07}$	$50.71^{+0.08}_{-0.08}$	$50.69^{+0.11}_{-0.11}$
	-15	$51.04^{+0.07}_{-0.07}$	$50.90^{+0.07}_{-0.07}$	$50.86^{+0.09}_{-0.09}$	$50.93^{+0.13}_{-0.12}$
	-13	$51.08^{+0.07}_{-0.07}$	$50.96^{+0.07}_{-0.07}$	$50.96^{+0.11}_{-0.10}$	$51.10^{+0.17}_{-0.15}$
<i>ModelB_Dust</i>					
$\log_{10} \dot{N}_{ion}$ (s ⁻¹ Mpc ⁻³)	-17	$50.75^{+0.10}_{-0.10}$	$50.72^{+0.13}_{-0.15}$	$50.81^{+0.13}_{-0.14}$	$50.87^{+0.15}_{-0.16}$
	-15	$50.84^{+0.09}_{-0.10}$	$50.83^{+0.13}_{-0.15}$	$50.97^{+0.13}_{-0.15}$	$51.09^{+0.17}_{-0.18}$
	-13	$50.88^{+0.10}_{-0.10}$	$50.88^{+0.14}_{-0.16}$	$51.05^{+0.15}_{-0.16}$	$51.27^{+0.20}_{-0.20}$
<i>ModelA_f_{esc}</i>					
$\log_{10} \dot{N}_{ion}$ (s ⁻¹ Mpc ⁻³)	-17	$50.82^{+0.07}_{-0.07}$	$50.64^{+0.06}_{-0.06}$	$50.52^{+0.08}_{-0.08}$	$50.53^{+0.13}_{-0.12}$
	-15	$50.98^{+0.07}_{-0.07}$	$50.86^{+0.07}_{-0.06}$	$50.90^{+0.11}_{-0.10}$	$50.99^{+0.14}_{-0.15}$
	-13	$51.07^{+0.07}_{-0.07}$	$51.03^{+0.08}_{-0.08}$	$51.09^{+0.14}_{-0.13}$	$51.24^{+0.20}_{-0.17}$
<i>ModelB_Dust</i>					
$\log_{10} \dot{N}_{ion}$ (s ⁻¹ Mpc ⁻³)	-17	$50.01^{+0.11}_{-0.11}$	$50.14^{+0.12}_{-0.13}$	$50.31^{+0.20}_{-0.22}$	$50.55^{+0.24}_{-0.30}$
	-15	$50.65^{+0.09}_{-0.09}$	$50.76^{+0.12}_{-0.10}$	$51.06^{+0.15}_{-0.16}$	$51.20^{+0.17}_{-0.20}$
	-13	$50.93^{+0.10}_{-0.10}$	$51.10^{+0.12}_{-0.12}$	$51.30^{+0.17}_{-0.16}$	$51.50^{+0.21}_{-0.20}$
Systematic Uncertainties					
Salpeter IMF				$\Delta \log_{10} \kappa_{ion} = -0.19$	
Dust: Calzetti w/ SMC-like extrapolation		Model A: $\Delta \log_{10} \xi_{ion} = 0$		Model B: $\Delta \log_{10} \xi_{ion} = +0.12$	

Table A.2: Calculated values of ρ_{UV} and \dot{N}_{ion} for the different integration limits and efficiency assumptions explored in the paper, based on the luminosity function parametrisations of Finkelstein *et al.* (2014). For each calculated value, we include statistical errors from the uncertainties in the Schechter (1976) parameters and β observations. Also shown are the effects of some of the assumptions made in Section 3.3.1 and their corresponding systematic changes to the estimated values.

Limit (M_{UV})		$z \sim 4$	$z \sim 5$	$z \sim 6$	$z \sim 7$
$\log_{10} \rho_{UV}$ (erg s ⁻¹ Hz ⁻¹ Mpc ⁻³)	-17	$26.28^{+0.01}_{-0.01}$	$26.18^{+0.01}_{-0.01}$	$25.90^{+0.02}_{-0.02}$	$25.78^{+0.06}_{-0.06}$
	-15	$26.35^{+0.02}_{-0.02}$	$26.28^{+0.02}_{-0.02}$	$26.10^{+0.06}_{-0.05}$	$25.99^{+0.15}_{-0.13}$
	-13	$26.38^{+0.02}_{-0.02}$	$26.32^{+0.03}_{-0.02}$	$26.24^{+0.10}_{-0.09}$	$26.15^{+0.24}_{-0.20}$
$\log_{10} f_{esc} \xi_{ion} = 24.5$					
$\log_{10} \dot{N}_{ion}$ (s ⁻¹ Mpc ⁻³)	-17	$50.78^{+0.01}_{-0.01}$	$50.68^{+0.01}_{-0.01}$	$50.40^{+0.02}_{-0.02}$	$50.28^{+0.06}_{-0.06}$
	-15	$50.85^{+0.02}_{-0.02}$	$50.78^{+0.02}_{-0.02}$	$50.60^{+0.06}_{-0.05}$	$50.49^{+0.15}_{-0.13}$
	-13	$50.88^{+0.02}_{-0.02}$	$50.82^{+0.03}_{-0.02}$	$50.74^{+0.10}_{-0.09}$	$50.65^{+0.24}_{-0.20}$
$\log_{10} f_{esc} \xi_{ion} \propto \langle \beta \rangle_{\rho_{UV}} (z)$					
$\log_{10} \dot{N}_{ion}$ (s ⁻¹ Mpc ⁻³)	-17	$50.70^{+0.02}_{-0.02}$	$50.65^{+0.04}_{-0.04}$	$50.49^{+0.06}_{-0.06}$	$50.46^{+0.11}_{-0.10}$
	-15	$50.77^{+0.02}_{-0.02}$	$50.75^{+0.04}_{-0.05}$	$50.69^{+0.09}_{-0.08}$	$50.67^{+0.17}_{-0.15}$
	-13	$50.80^{+0.03}_{-0.03}$	$50.79^{+0.05}_{-0.05}$	$50.83^{+0.12}_{-0.11}$	$50.83^{+0.26}_{-0.22}$
<i>Model B</i> - <i>Dust</i>					
$\log_{10} \dot{N}_{ion}$ (s ⁻¹ Mpc ⁻³)	-17	$50.49^{+0.07}_{-0.08}$	$50.58^{+0.12}_{-0.14}$	$50.59^{+0.11}_{-0.13}$	$50.63^{+0.15}_{-0.16}$
	-15	$50.57^{+0.07}_{-0.08}$	$50.68^{+0.12}_{-0.15}$	$50.79^{+0.13}_{-0.14}$	$50.84^{+0.20}_{-0.20}$
	-13	$50.60^{+0.07}_{-0.08}$	$50.73^{+0.12}_{-0.15}$	$50.93^{+0.15}_{-0.16}$	$50.99^{+0.28}_{-0.25}$
<i>Model A</i> - <i>f_{esc}</i>					
$\log_{10} \dot{N}_{ion}$ (s ⁻¹ Mpc ⁻³)	-17	$49.71^{+0.10}_{-0.12}$	$50.00^{+0.11}_{-0.13}$	$50.16^{+0.18}_{-0.20}$	$50.27^{+0.26}_{-0.33}$
	-15	$50.33^{+0.07}_{-0.08}$	$50.58^{+0.10}_{-0.09}$	$50.98^{+0.14}_{-0.15}$	$50.92^{+0.27}_{-0.29}$
	-13	$50.57^{+0.10}_{-0.10}$	$50.88^{+0.11}_{-0.11}$	$51.28^{+0.16}_{-0.16}$	$51.21^{+0.34}_{-0.34}$
$\log_{10} f_{esc} \xi_{ion} (M_{UV})$					
$\log_{10} \dot{N}_{ion}$ (s ⁻¹ Mpc ⁻³)	-17	$50.56^{+0.02}_{-0.02}$	$50.51^{+0.03}_{-0.03}$	$50.31^{+0.07}_{-0.06}$	$50.28^{+0.14}_{-0.13}$
	-15	$50.70^{+0.03}_{-0.03}$	$50.70^{+0.04}_{-0.04}$	$50.79^{+0.11}_{-0.10}$	$50.71^{+0.22}_{-0.21}$
	-13	$50.77^{+0.04}_{-0.04}$	$50.84^{+0.06}_{-0.05}$	$51.04^{+0.15}_{-0.14}$	$50.96^{+0.32}_{-0.28}$
<i>Model A</i> - <i>f_{esc}</i>					
$\log_{10} \dot{N}_{ion}$ (s ⁻¹ Mpc ⁻³)	-17	$49.71^{+0.10}_{-0.12}$	$50.00^{+0.11}_{-0.13}$	$50.16^{+0.18}_{-0.20}$	$50.27^{+0.26}_{-0.33}$
	-15	$50.33^{+0.07}_{-0.08}$	$50.58^{+0.10}_{-0.09}$	$50.98^{+0.14}_{-0.15}$	$50.92^{+0.27}_{-0.29}$
	-13	$50.57^{+0.10}_{-0.10}$	$50.88^{+0.11}_{-0.11}$	$51.28^{+0.16}_{-0.16}$	$51.21^{+0.34}_{-0.34}$
Systematic Uncertainties					
Salpeter IMF				$\Delta \log_{10} \kappa_{ion} = -0.19$	
Dust: Calzetti w/ SMC-like extrapolation		Model A: $\Delta \log_{10} \xi_{ion} = 0$	Model B: $\Delta \log_{10} \xi_{ion} = +0.12$		

Appendix B

Long appendix heading

Text of appendix.

Bibliography

- Aldoretta E. J., Caballero-Nieves S. M., Gies D. R., Nelan E. P., Wallace D. J., Hartkopf W. I., Henry T. J., Jao W. C., Maíz Apellániz J., Mason B. D., Moffat A. F. J., Norris R. P., Richardson N. D., Williams S. J., 2014. *eprint arXiv:1410.0021. The Multiplicity of Massive Stars: A High Angular Resolution Survey with the HST Fine Guidance Sensor.*
- Anders P., Alvensleben U. F. v., 2003. *A&A*, **401**(3), 1063. *Spectral and photometric evolution of young stellar populations: The impact of gaseous emission at various metallicities.*
- Ashby M. L. N., Willner S. P., Fazio G. G., Huang J. S., Arendt R., Barmby P., Barro G., Bell E. F., Bouwens R., Cattaneo A., Croton D., Davé R., Dunlop J. S., Egami E., Faber S., Finlator K., Grogin N. A., Guhathakurta P., Hernquist L., Hora J. L., Illingworth G. D., Kashlinsky A., Koekemoer A. M., Koo D. C., Labbé I., Li Y., Lin L., Moseley H., Nandra K., Newman J., Noeske K., Ouchi M., Peth M., Rigopoulou D., Robertson B., Sarajedini V., Simard L., Smith H. A., Wang Z., Wechsler R., Weiner B., Wilson G., Wuyts S., Yamada T., Yan H.-J., 2013. *ApJ*, **769**(1), 80. *SEDS: THE SPITZER EXTENDED DEEP SURVEY. SURVEY DESIGN, PHOTOMETRY, AND DEEP IRAC SOURCE COUNTS.*
- Avni Y., Bahcall J. N., 1980. *ApJ*, **235**, 694. *On the simultaneous analysis of several complete samples - The V/Vmax and Ve/Va variables, with applications to quasars.*
- Balestra I., Mainieri V., Popesso P., Dickinson M., Nonino M., Rosati P., Teimoorinia H., Vanzella E., Cristiani S., Cesarsky C., Fosbury R. A. E., Kuntschner H., Rettura A., the GOODS team, 2010. *A&A*, **512**, A12. *The Great Observatories Origins Deep Survey.*
- Becker G. D., Bolton J. S., 2013. *MNRAS*, **436**, 1023. *New measurements of the ionizing ultraviolet background over 2 .*
- Beckwith S. V. W., Stiavelli M., Koekemoer A. M., Caldwell J. A. R., Ferguson H. C., Hook R., Lucas R. A., Bergeron L. E., Corbin M., Jogee S., Panagia N., Robberto M., Royle P., Somerville R. S., Sosey M., 2006. *The Astronomical Journal*, **132**(5), 1729. *The Hubble Ultra Deep Field.*
- Behroozi P. S., Wechsler R. H., Conroy C., 2013. *ApJ*, **770**(1), 57. *THE AVERAGE STAR FORMATION HISTORIES OF GALAXIES IN DARK MATTER HALOS FROM z= 0-8.*

- Bennett C. L., Larson D., Weiland J. L., Jarosik N., Hinshaw G., Odegard N., Smith K. M., Hill R. S., Gold B., Halpern M., Komatsu E., Nolta M. R., Page L., Spergel D. N., Wollack E., Dunkley J., Kogut A., Limon M., Meyer S. S., Tucker G. S., Wright E. L., 2013. *ApJS*, **208**(2), 20. *NINE-YEAR WILKINSON MICROWAVE ANISOTROPY PROBE(WMAP) OBSERVATIONS: FINAL MAPS AND RESULTS.*
- Bolton J. S., Haehnelt M. G., 2007. *MNRAS*, **382**(1), 325. *The observed ionization rate of the intergalactic medium and the ionizing emissivity at $z \approx 5$: evidence for a photon-starved and extended epoch of reionization.*
- Borthakur S., Heckman T. M., Leitherer C., Overzier R. A., 2014. *Science*, **346**(6206), 216. *A local clue to the reionization of the universe.*
- Bouwens R. J., Illingworth G. D., Franx M., Ford H., 2007. *ApJ*, **670**(2), 928. *UV Luminosity Functions at $z \approx 4, 5$, and 6 from the Hubble Ultra Deep Field and Other Deep Hubble Space Telescope ACS Fields: Evolution and Star Formation History.*
- Bouwens R. J., Illingworth G. D., Franx M., Chary R.-R., Meurer G. R., Conselice C. J., Ford H., Giavalisco M., van Dokkum P. G., 2009. *ApJ*, **705**(1), 936. *UV CONTINUUM SLOPE AND DUST OBSCURATION FROM $z \approx 6$ TO $z \approx 2$: THE STAR FORMATION RATE DENSITY AT HIGH REDSHIFT.*
- Bouwens R. J., Illingworth G. D., Oesch P. A., Stiavelli M., van Dokkum P. G., Trenti M., Magee D., Labb   I., Franx M., Carollo C. M., Gonz  lez V., 2010. *ApJ*, **709**(2), L133. *DISCOVERY OF $z \approx 8$ GALAXIES IN THE HUBBLE ULTRA DEEP FIELD FROM ULTRA-DEEP WFC3/IR OBSERVATIONS.*
- Bouwens R. J., Illingworth G. D., Oesch P., Franx M., et al., 2011a. *UV-CONTINUUM SLOPES AT $Z \approx 4-7$ FROM THE HUDF09+ERS+CANDELS OBSERVATIONS: DISCOVERY OF A WELL-DEFINED UV-COLOR MAGNITUDE RELATIONSHIP FOR $Z \approx 4$ STAR-FORMING GALAXIES.*
- Bouwens R. J., Illingworth G. D., Oesch P. A., Labb   I., Trenti M., van Dokkum P. G., Carollo C. M., lez V. G., Magee D., 2011b. *ApJ*, **737**(2), 90. *Ultraviolet Luminosity Functions from $132 < z < 7$ and $z > 8$ Lyman-break Galaxies in the Ultra-deep HUDF09 and Wide-area Early Release Science WFC3/IR Observations.*
- Bouwens R. J., Illingworth G. D., Oesch P. A., Franx M., Labb   I., Trenti M., van Dokkum P. G., Carollo C. M., Gonz  lez V., Smit R., Magee D., 2012a. *ApJ*, **754**(2), 83. *UV-continuum Slopes at $z \approx 4-7$ from the HUDF09+ERS+CANDELS Observations: Discovery of a Well-defined UV Color-Magnitude Relationship for $z \approx 4$ Star-forming Galaxies.*
- Bouwens R. J., Illingworth G. D., Oesch P. A., Trenti M., Labb   I., Franx M., Stiavelli M., Carollo C. M., van Dokkum P. G., Magee D., 2012b. *ApJ*, **752**(1), L5. *LOWER-LUMINOSITY GALAXIES COULD REIONIZE THE UNIVERSE: VERY STEEP FAINT-END SLOPES TO THE UVLUMINOSITY FUNCTIONS AT $z \approx 5-8$ FROM THE HUDF09 WFC3/IR OBSERVATIONS.*

- Bouwens R. J., Illingworth G. D., Oesch P. A., Labb   I., van Dokkum P. G., Trenti M., Franx M., Smit R., Gonz  lez V., Magee D., 2014a. *eprint arXiv:13062950*, **793(2)**, 115. *UV-CONTINUUM SLOPES OF $z > 4$ GALAXIES FROM THE HUDF/XDF, HUDF09, ERS, CANDELS-SOUTH, AND CANDELS-NORTH FIELDS.*
- Bouwens R. J., Illingworth G. D., Oesch P. A., Trenti M., Labb   I., Bradley L., Carollo M., van Dokkum P. G., Gonz  lez V., Holwerda B., Franx M., Spitler L., Smit R., Magee D., 2014b. *eprint arXiv:1403.4295*. *UV Luminosity Functions at redshifts $z \approx 4$ to $z \approx 10$: 11000 Galaxies from HST Legacy Fields.*
- Brammer G. B., van Dokkum P. G., Coppi P., 2008. *ApJ*, **686(2)**, 1503. *EAZY: A Fast, Public Photometric Redshift Code.*
- Bridge C. R., Teplitz H. I., Siana B., Scarlata C., Conselice C. J., Ferguson H. C., Brown T. M., Salvato M., Rudie G. C., de Mello D. F., Colbert J., Gardner J. P., Giavalisco M., Armus L., 2010. *ApJ*, **720(1)**, 465. *A SPECTROSCOPIC SEARCH FOR LEAKING LYMAN CONTINUUM AT $z \approx 0.7$.*
- Bruzual G., Charlot S., 2003. *MNRAS*, **344(4)**, 1000. *Stellar population synthesis at the resolution of 2003.*
- Calzetti D., Armus L., Bohlin R. C., Kinney A. L., Koornneef J., Storchi-Bergmann T., 2000. *ApJ*, **533(2)**, 682. *The Dust Content and Opacity of Actively Star-forming Galaxies.*
- Calzetti D., Kinney A. L., Storchi-Bergmann T., 1994. *ApJ*, **429**, 582. *Dust extinction of the stellar continua in starburst galaxies: The ultraviolet and optical extinction law.*
- Capak P., Cowie L. L., Hu E. M., Barger A. J., Dickinson M., Fernandez E., Giavalisco M., Komiyama Y., Kretchmer C., McNally C., Miyazaki S., Okamura S., Stern D., 2004. *The Astronomical Journal*, **127(1)**, 180. *A Deep Wide-Field, Optical, and Near-Infrared Catalog of a Large Area around the Hubble Deep Field North.*
- Cappellari M., McDermid R. M., Alatalo K., Blitz L., Bois M., Bournaud F., Bureau M., Crocker A. F., Davies R. L., Davis T. A., de Zeeuw P. T., Duc P.-A., Emsellem E., Khochfar S., Krajnovi   D., Kuntschner H., Lablanche P.-Y., Morganti R., Naab T., Oosterloo T., Sarzi M., Scott N., Serra P., Weijmans A.-M., Young L. M., 2012. *Nature*, **484(7395)**, 485. *Systematic variation of the stellar initial mass function in early-type galaxies.*
- Caputi K. I., Cirasuolo M., Dunlop J. S., McLure R. J., Farrah D., Almaini O., 2011. *MNRAS*, **413(1)**, 162. *The stellar mass function of the most-massive galaxies at $z > 3$.*
- Castellano M., Sommariva V., Fontana A., Pentericci L., Santini P., Grazian A., Amorin R., Donley J. L., Dunlop J. S., Ferguson H. C., Fiore F., Galametz A., Gilalongo E., Guo Y., Huang K. H., Koekemoer A., Maiolino R., McLure R. J., Paris D., Schaerer D., Troncoso P., Vanzella E., 2014. *A&A*, **566**, A19. *Constraints on the star-formation rate of $z > 3$ LBGs with measured metallicity in the CANDELS GOODS-South field.*

- Chabrier G., 2003. *PUBL ASTRON SOC PAC*, **115(809)**, 763. *Galactic Stellar and Substellar Initial Mass Function.*
- Ciardi B., Bolton J. S., Maselli A., Graziani L., 2012. *MNRAS*, **423(1)**, 558. *The effect of intergalactic helium on hydrogen reionization: implications for the sources of ionizing photons at $z > 6$.*
- Coe D., Bradley L., Zitrin A., 2014. *eprint arXiv:1405.0011. Frontier Fields: High-Redshift Predictions and Early Results.*
- Coe D., Zitrin A., Carrasco M., Shu X., Zheng W., Postman M., Bradley L., Koekeboer A., Bouwens R. J., Broadhurst T., Monna A., Host O., Moustakas L. A., Ford H., Moustakas J., van der Wel A., Donahue M., Rodney S. A., Benítez N., Jouvel S., Seitz S., Kelson D. D., Rosati P., 2012. *ApJ*, **762(1)**, 32. *CLASH: THREE STRONGLY LENSED IMAGES OF A CANDIDATE $z \approx 11$ GALAXY.*
- Conroy C., Kratter K. M., 2012. *ApJ*, **755(2)**, 123. *RUNAWAY STARS AND THE ESCAPE OF IONIZING RADIATION FROM HIGH-REDSHIFT GALAXIES.*
- Conroy C., van Dokkum P. G., 2012. *ApJ*, **760(1)**, 71. *THE STELLAR INITIAL MASS FUNCTION IN EARLY-TYPE GALAXIES FROM ABSORPTION LINE SPECTROSCOPY. II. RESULTS.*
- Conroy C., Gunn J. E., White M., 2009. *ApJ*, **699(1)**, 486. *THE PROPAGATION OF UNCERTAINTIES IN STELLAR POPULATION SYNTHESIS MODELING. I. THE RELEVANCE OF UNCERTAIN ASPECTS OF STELLAR EVOLUTION AND THE INITIAL MASS FUNCTION TO THE DERIVED PHYSICAL PROPERTIES OF GALAXIES.*
- Conroy C., White M., Gunn J. E., 2009. *ApJ*, **708(1)**, 58. *THE PROPAGATION OF UNCERTAINTIES IN STELLAR POPULATION SYNTHESIS MODELING. II. THE CHALLENGE OF COMPARING GALAXY EVOLUTION MODELS TO OBSERVATIONS.*
- Conroy C., 2013. *ANNU REV ASTRON ASTR*, **51(1)**, 393. *Modeling the Panchromatic Spectral Energy Distributions of Galaxies.*
- Cooke J., Ryan-Weber E. V., Garel T., Díaz C. G., 2014. *MNRAS*, **441**, 837. *Lyman-continuum galaxies and the escape fraction of Lyman-break galaxies.*
- Croton D. J., Springel V., White S. D. M., De Lucia G., Frenk C. S., Gao L., Jenkins A., Kauffmann G., Navarro J. F., Yoshida N., 2006. *MNRAS*, **365(1)**, 11. *The many lives of active galactic nuclei: cooling flows, black holes and the luminosities and colours of galaxies.*
- Curtis-Lake E., McLure R. J., Dunlop J. S., Schenker M., Rogers A. B., Targett T., Cirasuolo M., Almaini O., Ashby M. L. N., Bradshaw E. J., Finkelstein S. L., Dickinson M., Ellis R. S., Faber S. M., Fazio G. G., Ferguson H. C., Fontana A., Grogin N. A., Hartley W. G., Kocevski D. D., Koekemoer A. M., Lai K., Robertson B. E., Vanzella E., Willner S. P., 2013. *MNRAS*, **429(1)**, 302. *The ages, masses and star formation rates of spectroscopically confirmed $z > 6$ galaxies in CANDELS.*

- Daddi E., Dickinson M., Morrison G., Chary R., Cimatti A., Elbaz D., Frayer D., Renzini A., Pope A., Alexander D. M., Bauer F. E., Giavalisco M., Huynh M., Kurk J., Mignoli M., 2007. *ApJ*, **670**(1), 156. *Multiwavelength Study of Massive Galaxies at z 2. I. Star Formation and Galaxy Growth.*
- Dahlen T., Mobasher B., Somerville R. S., Moustakas L. A., Dickinson M., Ferguson H. C., Giavalisco M., 2005. *ApJ*, **631**(1), 126. *The Evolution of the Optical and Near-Infrared Galaxy Luminosity Functions and Luminosity Densities to z 2.*
- Dahlen T., Mobasher B., Dickinson M., Ferguson H. C., Giavalisco M., Grogin N. A., Guo Y., Koekemoer A., Lee K.-S., Lee S.-K., Nonino M., Riess A. G., Salimbeni S., 2010. *ApJ*, **724**(1), 425. *A Detailed Study of Photometric Redshifts for GOODS-South Galaxies.*
- Dahlen T., Mobasher B., Faber S. M., Ferguson H. C., Barro G., Finkelstein S. L., Finlator K., Fontana A., Gruetzbauch R., Johnson S., Pforr J., Salvato M., Wiklind T., Wuyts S., Acquaviva V., Dickinson M. E., Guo Y., Huang J., Huang K.-H., Newman J. A., Bell E. F., Conselice C. J., Galametz A., Gawiser E., Giavalisco M., Grogin N. A., Hathi N., Kocevski D., Koekemoer A. M., Koo D. C., Lee K.-S., McGrath E. J., Papovich C., Peth M., Ryan R., Somerville R., Weiner B., Wilson G., 2013. *ApJ*, **775**(2), 93. *A CRITICAL ASSESSMENT OF PHOTOMETRIC REDSHIFT METHODS: A CANDELS INVESTIGATION.*
- Davé R., Katz N., Oppenheimer B. D., Kollmeier J. A., Weinberg D. H., 2013. *MNRAS*, **434**(3), 2645. *The neutral hydrogen content of galaxies in cosmological hydrodynamic simulations.*
- Dayal P., Ferrara A., 2012. *MNRAS*, **421**(3), 2568. *$\text{Ly}\alpha$ emitters and Lyman-break galaxies: dichotomous twins.*
- Dayal P., Dunlop J. S., Maio U., Ciardi B., 2013. *MNRAS*, **434**(2), 1486. *Simulating the assembly of galaxies at redshifts $z = 6\text{--}12$.*
- De Breuck C., Williams R. J., Swinbank M., Caselli P., Coppin K., Davis T. A., Maiolino R., Nagao T., Smail I., Walter F., Weiβ A., Zwaan M. A., 2014. *A&A*, **565**, A59. *ALMA resolves turbulent, rotating [CII] emission in a young starburst galaxy at $z=4.8$.*
- de Barros S., Schaerer D., Stark D. P., 2012. *eprint arXiv:12073663. Properties of $z \sim 3$ to $z \sim 6$ Lyman Break Galaxies. I. Impact of nebular emission at high redshift.*
- de Barros S., Schaerer D., Stark D. P., 2014. *A&A*, **563**, A81. *Properties of $z \sim 3\text{--}6$ Lyman break galaxies.*
- Dekel A., Zolotov A., Tweed D., Cacciato M., Ceverino D., Primack J. R., 2013. *MNRAS*, **435**(2), 999. *Toy models for galaxy formation versus simulations.*
- Dickinson M., Stern D., Giavalisco M., Ferguson H. C., Tsvetanov Z., Chornock R., Cristiani S., Dawson S., Dey A., Filippenko A. V., Moustakas L. A., Nonino M., Papovich C., Ravindranath S., Riess A. G., Rosati P., Spinrad H., Vanzella E., 2004. *ApJ*, **600**(2), L99. *Color-selected Galaxies at $z \sim 6$ in the Great Observatories Origins Deep Survey.*

- Dinerstein H. L., Shields G. A., 1986. *ApJ*, **311**, 45. *Reassessing the primordial helium abundance - New observations of NGC 4861 and CG 1116 + 51.*
- Duncan K., Conselice C. J., Mortlock A., Hartley W. G., Guo Y., Ferguson H. C., Davé R., Lu Y., Ownsworth J., Ashby M. L. N., Dekel A., Dickinson M., Faber S., Giavalisco M., Grogin N. A., Kocevski D., Koekemoer A., Somerville R. S., White C. E., 2014. *MNRAS*, **444**(3), 2960. *The mass evolution of the first galaxies: stellar mass functions and star formation rates at 4*.
- Dunlop J. S., McLure R. J., Robertson B. E., Ellis R. S., Stark D. P., Cirasuolo M., de Ravel L., 2011. *MNRAS*, **420**(1), 901. *A critical analysis of the ultraviolet continuum slopes (β) of high-redshift galaxies: no evidence (yet) for extreme stellar populations at $z \gtrsim 6$.*
- Dunlop J. S., Rogers A. B., McLure R. J., Ellis R. S., Robertson B. E., Koekemoer A., Dayal P., Curtis-Lake E., Wild V., Charlot S., Bowler R. A. A., Schenker M. A., Ouchi M., Ono Y., Cirasuolo M., Furlanetto S. R., Stark D. P., Targett T. A., Schneider E., 2013. *MNRAS*, **432**(4), 3520. *The UV continua and inferred stellar populations of galaxies at $z = 7\text{--}9$ revealed by the Hubble Ultra-Deep Field 2012 campaign.*
- Dunlop J. S. In: *adsabs.harvard.edu*, p. 223, Springer Berlin Heidelberg, Berlin, Heidelberg, 2012.
- Eales S., 1993. *ApJ*, **404**, 51. *Direct construction of the galaxy luminosity function as a function of redshift.*
- Ekström S., Georgy C., Eggenberger P., Meynet G., Mowlavi N., Wyttenbach A., Granada A., Decressin T., Hirschi R., Frischknecht U., Charbonnel C., Maeder A., 2012. *A&A*, **537**, A146. *Grids of stellar models with rotation.*
- Eldridge J. J., Stanway E. R., 2009. *MNRAS*, **400**(2), 1019. *Spectral population synthesis including massive binaries.*
- Eldridge J. J., Stanway E. R., 2011. *MNRAS*, **419**(1), 479. *The effect of stellar evolution uncertainties on the rest-frame ultraviolet stellar lines of Civ and Heii in high-redshift Lyman-break galaxies.*
- Erb D. K., Steidel C. C., Shapley A. E., Pettini M., Reddy N. A., Adelberger K. L., 2006. *ApJ*, **647**(1), 128. *H α Observations of a Large Sample of Galaxies at $z > 2$: Implications for Star Formation in HighRedshift Galaxies.*
- Erb D. K., Pettini M., Shapley A. E., Steidel C. C., Law D. R., Reddy N. A., 2010. *ApJ*, **719**(2), 1168. *Physical Conditions in a Young, Unreddened, Low-metallicity Galaxy at High Redshift.*
- Fan X., Carilli C. L., Keating B., 2006. *ANNU REV ASTRON ASTR*, **44**(1), 415. *Observational Constraints on Cosmic Reionization.*
- Faucher-Giguère C.-A., Lidz A., Hernquist L., Zaldarriaga M., 2008. *ApJ*, **682**(1), L9. *A Flat Photoionization Rate at $2 < z < 4.2$: Evidence for a Stellar-Dominated UV Background and against a Decline of Cosmic Star Formation beyond $z > 3$.*

Fazio G. G., Hora J. L., Allen L. E., Ashby M. L. N., Barmby P., Deutsch L. K., Huang J. S., Kleiner S., Marengo M., Megeath S. T., Melnick G. J., Pahre M. A., Patten B. M., Polizotti J., Smith H. A., Taylor R. S., Wang Z., Willner S. P., Hoffmann W. F., Pipher J. L., Forrest W. J., McMurry C. W., McCreight C. R., McKelvey M. E., McMurray R. E., Koch D. G., Moseley S. H., Arendt R. G., Mentzell J. E., Marx C. T., Losch P., Mayman P., Eichhorn W., Krebs D., Jhabvala M., Gezari D. Y., Fixsen D. J., Flores J., Shakoorzadeh K., Jungo R., Hakun C., Workman L., Karpati G., Kichak R., Whitley R., Mann S., Tollestrup E. V., Eisenhardt P., Stern D., Gorjian V., Bhattacharya B., Carey S., Nelson B. O., Glaccum W. J., Lacy M., Lowrance P. J., Laine S., Reach W. T., Stauffer J. A., Surace J. A., Wilson G., Wright E. L., Hoffman A., Domingo G., Cohen M., 2004. *ApJS*, **154**(1), 10. *The Infrared Array Camera (IRAC) for the Spitzer Space Telescope.*

Ferguson H. C., Dickinson M., Giavalisco M., Kretchmer C., Ravindranath S., Idzi R., Taylor E., Conselice C. J., Fall S. M., Gardner J. P., Livio M., Madau P., Moustakas L. A., Papovich C. M., Somerville R. S., Spinrad H., Stern D., 2004. *ApJ*, **600**(2), L107. *The Size Evolution of High-Redshift Galaxies.*

Fernandez E., Shull J. M., 2011. *ApJ*, **731**(1), 20. *THE EFFECT OF GALACTIC PROPERTIES ON THE ESCAPE FRACTION OF IONIZING PHOTONS.*

Fernández-Soto A., Lanzetta K. M., Chen H. W., 2003. *MNRAS*, **342**(4), 1215. *Mission: impossible (escape from the Lyman limit).*

Ferreras I., Barbera F. L., Rosa I. G. d. l., Vazdekis A., Carvalho R. R. d., Falcon-Barroso J., Ricciardelli E., 2013. *MNRAS: Letters*, **429**(1), L15. *Systematic variation of the stellar initial mass function with velocity dispersion in early-type galaxies.*

Finkelstein S. L., Papovich C., Ryan R. E., Pawlik A. H., Dickinson M., Ferguson H. C., Finlator K., Koekemoer A. M., Giavalisco M., Cooray A. R., Dunlop J. S., Faber S. M., Grogin N. A., Kocevski D. D., Newman J. A., 2012a. *ApJ*, **758**(2), 93. *CANDELS: THE CONTRIBUTION OF THE OBSERVED GALAXY POPULATION TO COSMIC REIONIZATION.*

Finkelstein S. L., Papovich C., Salmon B., Finlator K., Dickinson M., Ferguson H. C., Giavalisco M., Koekemoer A. M., Reddy N. A., Bassett R., Conselice C. J., Dunlop J. S., Faber S. M., Grogin N. A., Hathi N. P., Kocevski D. D., Lai K., Lee K.-S., McLure R. J., Mobasher B., Newman J. A., 2012b. *ApJ*, **756**(2), 164. *Candels: The Evolution of Galaxy Rest-frame Ultraviolet Colors from $z = 8$ to 4.*

Finkelstein S. L., Ryan R. E. J., Papovich C., Dickinson M., Song M., Somerville R., Ferguson H. C., Salmon B., Giavalisco M., Koekemoer A. M., Ashby M. L. N., Behroozi P., Castellano M., Dunlop J. S., Faber S. M., Fazio G. G., Fontana A., Grogin N. A., Hathi N., Jaacks J., Kocevski D. D., Livermore R., McLure R. J., Merlin E., Mobasher B., Newman J. A., Rafelski M., Tilvi V., Willner S. P., 2014. *eprint arXiv:1410.5439. The Evolution of the Galaxy Rest-Frame Ultraviolet Luminosity Function Over the First Two Billion Years.*

Finlator K., Oppenheimer B. D., Davé R., 2011. *MNRAS*, **410**(3), 1703. *Smoothly rising star formation histories during the reionization epoch.*

- Fioc M., Rocca-Volmerange B., 1997. *A&A*, **326**, 950. *PEGASE: a UV to NIR spectral evolution model of galaxies. Application to the calibration of bright galaxy counts.*
- Fontana A., Poli F., Menci N., Nonino M., Giallongo E., Cristiani S., D’Odorico S., 2003. *ApJ*, **587(2)**, 544. *A European Southern Observatory Very Large Telescope Survey of NearInfrared (Z 25) Selected Galaxies at Redshifts 4.5 .*
- Fontanot F., Cristiani S., Vanzella E., 2012. *MNRAS*, **425(2)**, 1413. *On the relative contribution of high-redshift galaxies and active galactic nuclei to reionization.*
- Fontanot F., Cristiani S., Pfrommer C., Cupani G., Vanzella E., 2014. *MNRAS*, **438(3)**, 2097. *On the evolution of the cosmic ionizing background.*
- Förster Schreiber N. M., Genzel R., Bouché N., Cresci G., Davies R., Buschkamp P., Shapiro K., Tacconi L. J., Hicks E. K. S., Genel S., Shapley A. E., Erb D. K., Steidel C. C., Lutz D., Eisenhauer F., Gillessen S., Sternberg A., Renzini A., Cimatti A., Daddi E., Kurk J., Lilly S., Kong X., Lehnert M. D., Nesvadba N., Verma A., McCracken H., Arimoto N., Mignoli M., Onodera M., 2009. *ApJ*, **706(2)**, 1364. *THE SINS SURVEY: SINFONI INTEGRAL FIELD SPECTROSCOPY OF $z \geq 2$ STAR-FORMING GALAXIES.*
- Giallongo E., Cristiani S., D’Odorico S., Fontana A., 2002. *ApJ*, **568(1)**, L9. *A Low Upper Limit to the Lyman Continuum Emission of Two Galaxies at [CLC][ITAL] z [/ITAL][/CLC].*
- Giallongo E., Grazian A., Fiore F., Fontana A., Pentericci L., Vanzella E., Dickinson M., Kocevski D., Castellano M., Cristiani S., Ferguson H., Finkelstein S., Grogin N. A., Hathi N., Koekemoer A. M., Newman J. A., Salvato M., 2015. *eprint arXiv:1502.02562. Faint AGNs at $z \geq 4$ in the CANDELS GOODS-S field: looking for contributors to the reionization of the Universe.*
- Giavalisco M., Dickinson M., Ferguson H. C., Ravindranath S., Kretchmer C., Moustakas L. A., Madau P., Fall S. M., Gardner J. P., Livio M., Papovich C., Renzini A., Spinrad H., Stern D., Riess A. G., 2004a. *ApJ*, **600(2)**, L103. *The Rest-Frame Ultraviolet Luminosity Density of Star-forming Galaxies at Redshifts $z \geq 3.5$.*
- Giavalisco M., Ferguson H. C., Koekemoer A. M., Dickinson M., Alexander D. M., Bauer F. E., Bergeron J., Biagetti C., Brandt W. N., Casertano S., Cesarsky C., Chatzichristou E., Conselice C. J., Cristiani S., Da Costa L., Dahlen T., de Mello D., Eisenhardt P., Erben T., Fall S. M., Fassnacht C., Fosbury R., Fruchter A., Gardner J. P., Grogin N. A., Hook R. N., Hornschemeier A. E., Idzi R., Jogee S., Kretchmer C., Laidler V., Lee K. S., Livio M., Lucas R., Madau P., Mobasher B., Moustakas L. A., Nonino M., Padovani P., Papovich C., Park Y., Ravindranath S., Renzini A., Richardson M., Riess A. G., Rosati P., Schirmer M., Schreier E., Somerville R. S., Spinrad H., Stern D., Stiavelli M., Strolger L., Urry C. M., Vandame B., Williams R., Wolf C., 2004b. *ApJ*, **600(2)**, L93. *The Great Observatories Origins Deep Survey: Initial results from optical and near-infrared imaging.*
- Gnedin N. Y., Kravtsov A. V., Chen H. W., 2008. *ApJ*, **672(2)**, 765. *Escape of Ionizing Radiation from HighRedshift Galaxies.*

González V., Labbé I., Bouwens R. J., Illingworth G. D., Franx M., Kriek M., Brammer G. B., 2010. *ApJ*, **713**(1), 115. *THE STELLAR MASS DENSITY AND SPECIFIC STAR FORMATION RATE OF THE UNIVERSE AT $z > 7$* .

González V., Labbé I., Bouwens R. J., Illingworth G. D., Franx M., Kriek M., 2011. *ApJ*, **735**(2), L34. *EVOLUTION OF GALAXY STELLAR MASS FUNCTIONS, MASS DENSITIES, AND MASS-TO-LIGHT RATIOS FROM $z = 7$ TO $z = 4$* .

González V., Bouwens R. J., Labbé I., Illingworth G. D., Oesch P. A., Franx M., Magee D., 2012. *arXiv. The Rest-frame UV-to-optical Colors and Spectral Energy Distributions of $z = 4$ -7 Galaxies*.

González V., Bouwens R. J., Illingworth G. D., Labbé I., Oesch P. A., Franx M., Magee D., 2014. *ApJ*, **781**(1), 34. *SLOW EVOLUTION OF THE SPECIFIC STAR FORMATION RATE AT $z > 2$: THE IMPACT OF DUST, EMISSION LINES, AND A RISING STAR FORMATION HISTORY*.

Grazian A., Castellano M., Koekemoer A. M., Fontana A., Pentericci L., Testa V., Boutsia K., Giallongo E., Giavalisco M., Santini P., 2011. *A&A*, **532**, 33. *A critical analysis of the UV luminosity function at redshift 7 from deep WFC3 data*.

Grazian A., Fontana A., Santini P., Dunlop J. S., Ferguson H. C., Castellano M., Amorin R., Ashby M. L. N., Barro G., Behroozi P., Boutsia K., Caputi K. I., Chary R.-R., Dekel A., Dickinson M. A., Faber S. M., Fazio G. G., Finkelstein S. L., Galametz A., Giallongo E., Giavalisco M., Grogin N. A., Guo Y., Kocevski D., Koekemoer A. M., Koo D. C., Lee K. S., Lu Y., Merlin E., Mobasher B., Nonino M., Papovich C., Paris D., Pentericci L., Reddy N., Renzini A., Salmon B., Salvato M., Sommariva V., Song M., Vanzella E., 2014. *eprint arXiv:1412.0532. The galaxy stellar mass function at 3.5*.

Grogin N. A., Kocevski D. D., Faber S. M., Ferguson H. C., Koekemoer A. M., Riess A. G., Acquaviva V., Alexander D. M., Almaini O., Ashby M. L. N., Barden M., Bell E. F., Bournaud F., Brown T. M., Caputi K. I., Casertano S., Cassata P., Castellano M., Chary R.-R., Cheung E., Cirasuolo M., Conselice C. J., Roshan Cooray A., Croton D. J., Daddi E., Dahlen T., Davé R., de Mello D. F., Dekel A., Dickinson M., Dolch T., Donley J. L., Dunlop J. S., Dutton A. A., Elbaz D., Fazio G. G., Finkelstein S. L., Fontana A., Gardner J. P., Garnavich P. M., Gawiser E., Giavalisco M., Grazian A., Guo Y., Hathi N. P., Häussler B., Hopkins P. F., Huang J.-S., Huang K.-H., Kartaltepe J. S., Kirshner R. P., Koo D. C., Lai K., Lee K.-S., Li W., Lotz J. M., Lucas R. A., Madau P., McCarthy P. J., McGrath E. J., McIntosh D. H., McLure R. J., Mobasher B., Moustakas L. A., Mozena M., Nandra K., Newman J. A., Niemi S.-M., Noeske K. G., Papovich C., Pentericci L., Pope A., Primack J. R., Rajan A., Ravindranath S., Reddy N. A., Renzini A., Rix H.-W., Robaina A. R., Rosario D. J., Rosati P., Salimbeni S., Scarlata C., Siana B., Simard L., Smidt J., Somerville R. S., Spinrad H., Straughn A. N., Strolger L.-G., Telford O., Teplitz H. I., Trump J. R., van der Wel A., Villforth C., Wechsler R. H., Weiner B. J., Wiklind T., Wild V., Wilson G., Wuys S., Yan H.-J., Yun M. S., 2011. *ApJS*, **197**(2), 35. *CANDELS: The Cosmic Assembly Near-infrared Deep Extragalactic Legacy Survey*.

Guhathakurta P., Tyson J. A., Majewski S. R., 1990. *ApJ*, **357**, L9. *A redshift limit for the faint blue galaxy population from deep U band imaging*.

Guo Y., Ferguson H. C., Giavalisco M., Barro G., Willner S. P., Ashby M. L. N., Dahlen T., Donley J. L., Faber S. M., Fontana A., Galametz A., Grazian A., Huang K.-H., Kocevski D. D., Koekemoer A. M., Koo D. C., McGrath E. J., Peth M., Salvato M., Wuyts S., Castellano M., Cooray A. R., Dickinson M. E., Dunlop J. S., Fazio G. G., Gardner J. P., Gawiser E., Grogan N. A., Hathi N. P., Hsu L.-T., Lee K.-S., Lucas R. A., Mobasher B., Nandra K., Newman J. A., van der Wel A., 2013. *ApJS*, **207(2)**, 24. *CANDELS MULTI-WAVELENGTH CATALOGS: SOURCE DETECTION AND PHOTOMETRY IN THE GOODS-SOUTH FIELD.*

Hagele G. F., Perez-Montero E., Diaz A. I., Terlevich E., Terlevich R., 2006. *MNRAS*, **372(1)**, 293. *The temperature and ionization structure of the emitting gas in H II galaxies: implications for the accuracy of abundance determinations.*

Hathi N. P., Jansen R. A., Windhorst R. A., Cohen S. H., Keel W. C., Corbin M. R., Ryan, Jr R. E., 2007. *The Astronomical Journal*, **135(1)**, 156. *SURFACE BRIGHTNESS PROFILES OF COMPOSITE IMAGES OF COMPACT GALAXIES AT z 4-6 IN THE HUBBLE ULTRA DEEP FIELD.*

Hathi N. P., Malhotra S., Rhoads J. E., 2008. *ApJ*, **673(2)**, 686. *Starburst Intensity Limit of Galaxies at z5- 6.*

Heckman T. M., Borthakur S., Overzier R., Kauffmann G., Basu-Zych A., Leitherer C., Sembach K., Martin D. C., Rich R. M., Schiminovich D., Seibert M., 2011. *ApJ*, **730(1)**, 5. *EXTREME FEEDBACK AND THE EPOCH OF REIONIZATION: CLUES IN THE LOCAL UNIVERSE.*

Hinshaw G., Larson D., Komatsu E., Spergel D. N., Bennett C. L., Dunkley J., Nolta M. R., Halpern M., Hill R. S., Odegard N., Page L., Smith K. M., Weiland J. L., Gold B., Jarosik N., Kogut A., Limon M., Meyer S. S., Tucker G. S., Wollack E., Wright E. L., 2013. *ApJS*, **208(2)**, 19. *NINE-YEAR WILKINSON MICROWAVE ANISOTROPY PROBE(WMAP) OBSERVATIONS: COSMOLOGICAL PARAMETER RESULTS.*

Huang K.-H., Ferguson H. C., Ravindranath S., Su J., 2013. *ApJ*, **765(1)**, 68. *THE BIVARIATE SIZE-LUMINOSITY RELATIONS FOR LYMAN BREAK GALAXIES AT z 4-5.*

Ilbert O., Tresse L., Zucca E., Bardelli S., Arnouts S., Zamorani G., Pozzetti L., Bottini D., Garilli B., Le Brun V., Le Fèvre O., Maccagni D., Picat J. P., Scaramella R., Scoville M., Vettolani G., Zanichelli A., Adami C., Arnaboldi M., Bolzonella M., Cappi A., Charlot S., Contini T., Foucaud S., Franzetti P., Gavignaud I., Guzzo L., Iovino A., McCracken H. J., Marano B., Marinoni C., Mathez G., Mazure A., Meneux B., Merighi R., Paltani S., Pello R., Pollo A., Radovich M., Bondi M., Bongiorno A., Busarello G., Ciliegi P., Lamareille F., Mellier Y., Merluzzi P., Ripepi V., Rizzo D., 2005. *A&A*, **439(3)**, 863. *The VIMOS-VLT deep survey. Evolution of the galaxy luminosity function up to z = 2 in first epoch data.*

Iwata I., Inoue A. K., Matsuda Y., Furusawa H., Hayashino T., Kousai K., Akiyama M., Yamada T., Burgarella D., Deharveng J. M., 2009. *ApJ*, **692(2)**, 1287. *DETECTIONS OF LYMAN CONTINUUM FROM STAR-FORMING GALAXIES AT z 3 THROUGH SUBARU/SUPRIME-CAM NARROW-BAND IMAGING.*

Izotov Y. I., Stasińska G., Guseva N. G., 2013. *A&A*, **558**, A57. *Primordial 4He abundance: a determination based on the largest sample of H II regions with a methodology tested on model H II regions.*

Izotov Y. I., Thuan T. X., Lipovetsky V. A., 1994. *ApJ*, **435**, 647. *The primordial helium abundance from a new sample of metal-deficient blue compact galaxies.*

Jones T., Stark D. P., Ellis R. S., 2012. *ApJ*, **751(1)**, 51. *KECK SPECTROSCOPY OF FAINT 3.*

Kennicutt, Jr R. C., 1998. *ApJ*, **498(2)**, 541. *The Global Schmidt Law in Starforming Galaxies.*

Kimm T., Cen R., 2014. *ApJ*, **788(2)**, 121. *ESCAPE FRACTION OF IONIZING PHOTONS DURING REIONIZATION: EFFECTS DUE TO SUPERNOVA FEEDBACK AND RUNAWAY OB STARS.*

Koekemoer A. M., Faber S. M., Ferguson H. C., Grogin N. A., Kocevski D. D., Koo D. C., Lai K., Lotz J. M., Lucas R. A., McGrath E. J., Ogaz S., Rajan A., Riess A. G., Strolger L., Casertano S., Castellano M., Dahlen T., Dickinson M., Dolch T., Fontana A., Giavalisco M., Grazian A., Guo Y., Hathi N. P., Huang K.-H., van der Wel A., Yan H.-J., Acquaviva V., Alexander D. M., Almaini O., Ashby M. L. N., Barden M., Bell E. F., Bournaud F., Brown T. M., Caputi K. I., Cassata P., Chary R.-R., Cheung E., Cirasuolo M., Conselice C. J., Cooray A. R., Croton D. J., Daddi E., Davé R., de Mello D. F., de Ravel L., Dekel A., Donley J. L., Dunlop J. S., Dutton A. A., Elbaz D., Fazio G. G., Finkelstein S. L., Frazer C., Gardner J. P., Garnavich P. M., Gawiser E., Gruetzbauch R., Hartley W. G., Häussler B., Herrington J., Hopkins P. F., Huang J.-S., Johnson A., Kartaltepe J. S., Khostovan A. A., Kirshner R. P., Lani C., Lee K.-S., Li W., Madau P., McCarthy P. J., McIntosh D. H., McLure R. J., McPartland C., Mobasher B., Moreira H., Mortlock A., Moustakas L. A., Mozena M., Nandra K., Newman J. A., Nielsen J. L., Niemi S., Noeske K. G., Papovich C., Pentericci L., Pope A., Primack J. R., Ravindranath S., Reddy N. A., Renzini A., Rix H.-W., Robaina A. R., Rosario D. J., Rosati P., Salimbeni S., Scarlata C., Siana B., Simard L., Smidt J., Snyder D., Somerville R. S., Spinrad H., Straughn A. N., Telford O., Teplitz H. I., Trump J. R., Vargas C., Villforth C., Wagner C. R., Wandro P., Wechsler R. H., Weiner B. J., Wiklind T., Wild V., Wilson G., Wuyts S., Yun M. S., 2011. *ApJS*, **197(2)**, 36. *CANDELS: THE COSMIC ASSEMBLY NEAR-INFRARED DEEP EXTRAGALACTIC LEGACY SURVEY—THE HUBBLE SPACE TELESCOPE OBSERVATIONS, IMAGING DATA PRODUCTS, AND MOSAICS.*

Koekemoer A. M., Ellis R. S., McLure R. J., Dunlop J. S., Robertson B. E., Ono Y., Schenker M. A., Ouchi M., Bowler R. A. A., Rogers A. B., Curtis-Lake E., Schneider E., Charlot S., Stark D. P., Furlanetto S. R., Cirasuolo M., Wild V., Targett T., 2013. *ApJS*, **209(1)**, 3. *THE 2012 HUBBLE ULTRA DEEP FIELD (UDF12): OBSERVATIONAL OVERVIEW.*

Kriek M., Shapley A. E., Reddy N. A., Siana B., Coil A. L., Mobasher B., Freeman W. R., de Groot L., Price S. H., Sanders R., Shvarei I., Brammer G. B., Momcheva I. G., Skelton R. E., van Dokkum P. G., Whitaker K. E., Aird J., Azadi M., Kassis M., Bullock J. S., Conroy C., Davé R., Keres D., Krumholz M., 2014. *eprint*

- arXiv:1412.1835. The MOSFIRE Deep Evolution Field (MOSDEF) Survey: Rest-Frame Optical Spectroscopy For 1500 H-Selected Galaxies at 1.37 .*
- Kroupa P., 2001. *MNRAS*, **322**(2), 231. *On the variation of the initial mass function.*
- Krueger H., Fritze-v Alvensleben U., Loose H.-H., 1995. *A&A*, **303**, 41. *Optical and near infrared spectral energy distributions. of blue compact galaxies from evolutionary synthesis.*
- Kuhlen M., Faucher-Giguère C.-A., 2012. *MNRAS*, **423**(1), 862. *Concordance models of reionization: implications for faint galaxies and escape fraction evolution.*
- Kurk J., Cimatti A., Daddi E., Mignoli M., Pozzetti L., Dickinson M., Bolzonella M., Zamorani G., Cassata P., Rodighiero G., Franceschini A., Renzini A., Rosati P., Halliday C., Berta S., 2012. *A&A*, **549**, A63. *GMASS ultradeep spectroscopy of galaxies at $z \geq 2$.*
- Labbé I., González V., Bouwens R. J., Illingworth G. D., Franx M., Trenti M., Oesch P. A., van Dokkum P. G., Stiavelli M., Carollo C. M., Kriek M., Magee D., 2010. *ApJ*, **716**(2), L103. *STAR FORMATION RATES AND STELLAR MASSES OF $z=7-8$ GALAXIES FROM IRAC OBSERVATIONS OF THE WFC3/IR EARLY RELEASE SCIENCE AND THE HUDF FIELDS.*
- Laidler V. G., Papovich C., Grogin N. A., Idzi R., Dickinson M., Ferguson H. C., Hilbert B., Clubb K., Ravindranath S., 2007. *PUBL ASTRON SOC PAC*, **119**(861), 1325. *TFIT: A Photometry Package Using Prior Information for MixedResolution Data Sets.*
- Laskar T., Berger E., Chary R.-R., 2011. *ApJ*, **739**(1), 1. *EXPLORING THE GALAXY MASSMETALLICITY RELATION AT $z < 35$.*
- Le Fèvre O., Vettolani G., Paltani S., Tresse L., Zamorani G., Le Brun V., Moreau C., Bottini D., Maccagni D., Picat J. P., Scaramella R., Scoville N., Zanichelli A., Adami C., Arnouts S., Bardelli S., Bolzonella M., Cappi A., Charlot S., Contini T., Foucaud S., Franzetti P., Garilli B., Gavignaud I., Guzzo L., Ilbert O., Iovino A., McCracken H. J., Mancini D., Marano B., Marinoni C., Mathez G., Mazure A., Meneux B., Merighi R., Pell R., Pollo A., Pozzetti L., Radovich M., Zucca E., Arnaboldi M., Bondi M., Bongiorno A., Busarello G., Ciliegi P., Gregorini L., Mellier Y., Merluzzi P., Ripepi V., Rizzo D., 2004. *A&A*, **428**(3), 1043. *The VIMOS VLT Deep Survey.*
- Lee S.-K., Ferguson H. C., Somerville R. S., Wiklind T., Giavalisco M., 2010. *ApJ*, **725**(2), 1644. *The Estimation of Star Formation Rates and Stellar Population Ages of High-redshift Galaxies from Broadband Photometry.*
- Lee K.-S., Dey A., Reddy N., Brown M. J. I., Gonzalez A. H., Jannuzi B. T., Cooper M. C., Fan X., Bian F., Glikman E., Stern D., Brodwin M., Cooray A. R., 2011. *ApJ*, **733**(2), 99. *THE AVERAGE PHYSICAL PROPERTIES AND STAR FORMATION HISTORIES OF THE UV-BRIGHTTEST STAR-FORMING GALAXIES AT $z > 3.7$.*
- Lee K.-S., Ferguson H. C., Wiklind T., Dahmen T., Dickinson M. E., Giavalisco M., Grogin N., Papovich C., Messias H., Guo Y., Lin L., 2012. *ApJ*, **752**(1), 66. *How Do Star-forming Galaxies at $z > 3$ Assemble Their Masses?*

- Lee S.-K., Ferguson H. C., Somerville R. S., Giavalisco M., Wiklind T., Dahlen T., 2014. *ApJ*, **783(2)**, 81. *STEADILY INCREASING STAR FORMATION RATES IN GALAXIES OBSERVED AT $z > 5$ IN THE CANDELS/GOODS-S FIELD.*
- Leitherer C., Schaerer D., Goldader J. D., Delgado R. M. G., Robert C., Kune D. F., de Mello D. F., Devost D., Heckman T. M., 1999. *ApJS*, **123(1)**, 3. *Starburst99: Synthesis Models for Galaxies with Active Star Formation.*
- Leitherer C., Ekström S., Meynet G., Schaerer D., Agienko K. B., Levesque E. M., 2014. *ApJS*, **212(1)**, 14. *THE EFFECTS OF STELLAR ROTATION. II. A COMPREHENSIVE SET OF STARBURST99 MODELS.*
- Lorenzoni S., Bunker A. J., Wilkins S. M., Stanway E. R., Jarvis M. J., Caruana J., 2011. *MNRAS*, **414(2)**, 1455. *Star-forming galaxies at $z \approx 8$ -9 from Hubble Space Telescope/WFC3: implications for reionization.*
- Lu Y., Mo H. J., Weinberg M. D., Katz N., 2011. *MNRAS*, **416(3)**, 1949. *A Bayesian approach to the semi-analytic model of galaxy formation: methodology.*
- Lu Y., Wechsler R. H., Somerville R. S., Croton D., Porter L., Primack J., Behroozi P. S., Ferguson H. C., Koo D. C., Guo Y., Safarzadeh M., Finlator K., Castellano M., White C. E., Sommariva V., Moody C., 2013. *arXiv:1312.3233. A Comparison between Semi-Analytic Model Predictions for the CANDELS Survey.*
- Madau P., Ferguson H. C., Dickinson M. E., Giavalisco M., Steidel C. C., Fruchter A., 1996. *MNRAS*, **283(4)**, 1388. *High-redshift galaxies in the Hubble Deep Field: colour selection and star formation history to $z \approx 4$.*
- Madau P., Haardt F., Rees M. J., 1999. *ApJ*, **514(2)**, 648. *Radiative Transfer in a Clumpy Universe. III. The Nature of Cosmological Ionizing Sources.*
- Madau P., Pozzetti L., Dickinson M., 1998. *ApJ*, **498(1)**, 106. *The Star Formation History of Field Galaxies.*
- Maiolino R., Nagao T., Grazian A., Cocchia F., Marconi A., Mannucci F., Cimatti A., Pipino A., Fontana A., Granato G. L., Matteucci F., Pentericci L., Risaliti G., Salvati M., Silva L., 2008a. *Formation and Evolution of Galaxy Disks ASP Conference Series*, **396**, 409. *The Mass-Metallicity Relation at $z < 3$.*
- Maiolino R., Nagao T., Grazian A., Cocchia F., Marconi A., Mannucci F., Cimatti A., Pipino A., Ballero S., Calura F., Chiappini C., Fontana A., Granato G. L., Matteucci F., Pastorini G., Pentericci L., Risaliti G., Salvati M., Silva L., 2008b. *A&A*, **488(2)**, 463. *AMAZE.*
- Maraston C., Pforr J., Renzini A., Daddi E., Dickinson M., Cimatti A., Tonini C., 2010. *MNRAS*, **407(2)**, 830. *Star formation rates and masses of $z < 2$ galaxies from multicolour photometry.*
- Maraston C., 2005. *MNRAS*, **362(3)**, 799. *Evolutionary population synthesis: models, analysis of the ingredients and application to high- z galaxies.*

- Marchesini D., van Dokkum P. G., Förster Schreiber N. M., Franx M., Labbé I., Wuyts S., 2009. *ApJ*, **701(2)**, 1765. *THE EVOLUTION OF THE STELLAR MASS FUNCTION OF GALAXIES FROM $z=4.0$ AND THE FIRST COMPREHENSIVE ANALYSIS OF ITS UNCERTAINTIES: EVIDENCE FOR MASS-DEPENDENT EVOLUTION.*
- Martín-Navarro I., Pérez-González P. G., Trujillo I., Esquej P., Vazdekis A., Sánchez H. D., Barro G., Bruzual G., Charlot S., Cava A., Ferreras I., Espino N., La Barbera F., 2014. *The stellar initial mass function at $z < 1$.*
- McLeod D. J., McLure R. J., Dunlop J. S., Robertson B. E., Ellis R. S., Targett T. T., 2014. *eprint arXiv:1412.1472. New redshift $z > 9$ galaxies in the Hubble Frontier Fields: Implications for early evolution of the UV luminosity density.*
- McLure R. J., Cirasuolo M., Dunlop J. S., Foucaud S., Almaini O., 2009. *MNRAS*, **395(4)**, 2196. *The luminosity function, halo masses and stellar masses of luminous Lyman-break galaxies at redshifts $5 < z < 6$.*
- McLure R. J., Dunlop J. S., de Ravel L., Cirasuolo M., Ellis R. S., Schenker M., Robertson B. E., Koekemoer A. M., Stark D. P., Bowler R. A. A., 2011. *MNRAS*, **418(3)**, 2074. *A robust sample of galaxies at redshifts $6.0 < z < 7.0$.*
- McLure R. J., Dunlop J. S., Bowler R. A. A., Curtis-Lake E., Schenker M., Ellis R. S., Robertson B. E., Koekemoer A. M., Rogers A. B., Ono Y., Ouchi M., Charlot S., Wild V., Stark D. P., Furlanetto S. R., Cirasuolo M., Targett T. A., 2013. *MNRAS*, **432(4)**, 2696. *A new multifield determination of the galaxy luminosity function at $z = 7\text{--}9$ incorporating the 2012 Hubble Ultra-Deep Field imaging.*
- Meurer G. R., Heckman T. M., Calzetti D., 1999. *ApJ*, **521(1)**, 64. *Dust Absorption and the Ultraviolet Luminosity Density at $z > 3$ as Calibrated by Local Starburst Galaxies.*
- Moster B. P., Somerville R. S., Newman J. A., Rix H.-W., 2011. *ApJ*, **731(2)**, 113. *A COSMIC VARIANCE COOKBOOK.*
- Muzzin A., Marchesini D., Stefanon M., Franx M., McCracken H. J., Milvang-Jensen B., Dunlop J. S., Fynbo J. P. U., Brammer G., Labbé I., van Dokkum P. G., 2013. *ApJ*, **777(1)**, 18. *THE EVOLUTION OF THE STELLAR MASS FUNCTIONS OF STAR-FORMING AND QUIESCENT GALAXIES TO $z=4$ FROM THE COSMOS/UltraVISTA SURVEY.*
- Nayyeri H., Mobasher B., Hemmati S., de Barros S., Ferguson H. C., Wiklind T., Dahlen T., Dickinson M., Giavalisco M., Fontana A., Ashby M., Barro G., Guo Y., Hathi N. P., Kassin S., Koekemoer A., Willner S., Dunlop J. S., Paris D., Targett T. A., 2014. *ApJ*, **794(1)**, 68. *A STUDY OF MASSIVE AND EVOLVED GALAXIES AT HIGH REDSHIFT.*
- Neistein E., Dekel A., 2007. *MNRAS*, **383(2)**, 615. *Constructing merger trees that mimic N -body simulations.*

- Nestor D. B., Shapley A. E., Kornei K. A., Steidel C. C., Siana B., 2013. *ApJ*, **765**(1), 47. *A REFINED ESTIMATE OF THE IONIZING EMISSIVITY FROM GALAXIES AT $z \approx 3$: SPECTROSCOPIC FOLLOW-UP IN THE SSA22a FIELD.*
- Newman J. A., Davis M., 2002. *ApJ*, **564**(2), 567. *Measuring the Cosmic Equation of State with Counts of Galaxies. II. Error Budget for the DEEP2 Redshift Survey.*
- Nonino M., Dickinson M., Rosati P., Grazian A., Reddy N., Cristiani S., Giavalisco M., Kuntschner H., Vanzella E., Daddi E., Fosbury R. A. E., Cesarsky C., 2009. *ApJS*, **183**(2), 244. *DEEP UBAND AND RIMAGING OF GOODS-SOUTH: OBSERVATIONS, DATA REDUCTION AND FIRST RESULTS.*
- Oesch P. A., Bouwens R. J., Illingworth G. D., Carollo C. M., Franx M., Labb   I., Magee D., Stiavelli M., Trenti M., van Dokkum P. G., 2009. *ApJ*, **709**(1), L16. *$z \approx 7$ GALAXIES IN THE HUDF: FIRST EPOCH WFC3/IR RESULTS.*
- Oesch P. A., Bouwens R. J., Carollo C. M., Illingworth G. D., Trenti M., Stiavelli M., Magee D., Labb   I., Franx M., 2010. *The Astrophysical Journal Letters*, **709**(1), L21. *Structure and Morphologies of $z \approx 7$ -8 Galaxies from Ultra-deep WFC3/IR Imaging of the Hubble Ultra-deep Field.*
- Oesch P. A., Labb   I., Bouwens R. J., Illingworth G. D., Gonz  lez V., Franx M., Trenti M., Holden B. P., van Dokkum P. G., Magee D., 2013. *ApJ*, **772**(2), 136. *A REST-FRAME OPTICAL VIEW ON $z \approx 4$ GALAXIES. I. COLOR AND AGE DISTRIBUTIONS FROM DEEP IRAC PHOTOMETRY OF THE IUDF10 AND GOODS SURVEYS.*
- Oesch P. A., Bouwens R. J., Illingworth G. D., Labb   I., Smit R., Franx M., van Dokkum P. G., Momcheva I., Ashby M. L. N., Fazio G. G., Huang J. S., Willner S. P., Gonz  lez V., Magee D., Trenti M., Brammer G. B., Skelton R. E., Spitler L. R., 2014. *ApJ*, **786**(2), 108. *THE MOST LUMINOUS $z \approx 9$ -10 GALAXY CANDIDATES YET FOUND: THE LUMINOSITY FUNCTION, COSMIC STAR-FORMATION RATE, AND THE FIRST MASS DENSITY ESTIMATE AT 500 Myr.*
- Oke J. B., Gunn J. E., 1983. *ApJ*, **266**, 713. *Secondary standard stars for absolute spectrophotometry.*
- Ono Y., Shimasaku K., Dunlop J., Farrah D., McLure R., Okamura S., 2010. *ApJ*, **724**(2), 1524. *STELLAR POPULATIONS OF Ly   EMITTERS AT $z \approx 6$ -7: CONSTRAINTS ON THE ESCAPE FRACTION OF IONIZING PHOTONS FROM GALAXY BUILDING BLOCKS.*
- Ota K., Walter F., Ohta K., Hatsukade B., Carilli C. L., da Cunha E., Gonz  lez-L  pez J., Decarli R., Hodge J. A., Nagai H., Egami E., Jiang L., Iye M., Kashikawa N., Riechers D. A., Bertoldi F., Cox P., Neri R., Wei   A., 2014. *ApJ*, **792**(1), 34. *ALMA OBSERVATION OF 158 μ m [C II] LINE AND DUST CONTINUUM OF A $Z=7$ NORMALLY STAR-FORMING GALAXY IN THE EPOCH OF REIONIZATION.*
- Ouchi M., Mobasher B., Shimasaku K., Ferguson H. C., Fall S. M., Ono Y., Kashikawa N., Morokuma T., Nakajima K., Okamura S., Dickinson M., Giavalisco M., Ohta K., 2009. *ApJ*, **706**(2), 1136. *LARGE AREA SURVEY FOR $z=7$ GALAXIES IN SDF AND GOODS-N: IMPLICATIONS FOR GALAXY FORMATION AND COSMIC REIONIZATION.*

- Ouchi M., Ellis R., Ono Y., Nakanishi K., Kohno K., Momose R., Kurono Y., Ashby M. L. N., Shimasaku K., Willner S. P., Fazio G. G., Tamura Y., Iono D., 2013. *ApJ*, **778(2)**, 102. *An Intensely Star-forming Galaxy at z > 7 with Low Dust and Metal Content Revealed by Deep ALMA and HST Observations.*
- Papovich C., Finkelstein S. L., Ferguson H. C., Lotz J. M., Giavalisco M., 2011. *MNRAS*, **412(2)**, 1123. *The rising star formation histories of distant galaxies and implications for gas accretion with time.*
- Partridge R. B., Peebles P. J. E., 1967. *ApJ*, **147**, 868. *Are Young Galaxies Visible?*
- Pawlik A. H., Schaye J., van Scherpenzeel E., 2009. *MNRAS*, **394(4)**, 1812. *Keeping the Universe ionized: photoheating and the clumping factor of the high-redshift intergalactic medium.*
- Pei Y. C., 1992. *ApJ*, **395**, 130. *Interstellar dust from the Milky Way to the Magellanic Clouds.*
- Penzias A. A., Wilson R. W., 1965. *ApJ*, **142**, 419. *A Measurement of Excess Antenna Temperature at 4080 Mc/s.*
- Pérez González P. G., Rieke G. H., Villar V., Barro G., Blaylock M., Egami E., Gallego J., Gil de Paz A., Pascual S., Zamorano J., Donley J. L., 2008. *ApJ*, **675(1)**, 234. *The Stellar Mass Assembly of Galaxies from z= 0 to z= 4: Analysis of a Sample Selected in the RestFrame NearInfrared with Spitzer.*
- Pirzkal N., Rothberg B., Nilsson K. K., Finkelstein S., Koekemoer A., Malhotra S., Rhoads J., 2012. *ApJ*, **748(2)**, 122. *A Link to the Past: Using Markov Chain Monte Carlo Fitting to Constrain Fundamental Parameters of High-redshift Galaxies.*
- Pirzkal N., Rothberg B., Ryan R., Coe D., Malhotra S., Rhoads J., Noeske K., 2013. *Real or Interloper? The Redshift Likelihoods of z > 8 Galaxies in the HUDF12.*
- Planck Collaboration, Ade P. A. R., Aghanim N., Arnaud M., Ashdown M., Aumont J., Baccigalupi C., Banday A. J., Barreiro R. B., Bartlett J. G., Bartolo N., Battaner E., Battye R., Benabed K., Benoît A., Benoit-Levy A., Bernard J. P., Bersanelli M., Bielewicz P., Bonaldi A., Bonavera L., Bond J. R., Borrill J., Bouchet F. R., Boulanger F., Bucher M., Burigana C., Butler R. C., Calabrese E., Cardoso J. F., Catalano A., Challinor A., Chamballu A., Chary R.-R., Chiang H. C., Chluba J., Christensen P. R., Church S., Clements D. L., Colombi S., Colombo, L. P. L., Combet C., Coulais A., Crill B. P., Curto A., Cuttaia F., Danese L., Davies R. D., Davis R. J., de Bernardis P., de Rosa A., de Zotti G., Delabrouille J., Désert F. X., Di Valentino E., Dickinson C., Diego J. M., Dolag K., Dole H., Donzelli S., Dore O., Douspis M., Ducout A., Dunkley J., Dupac X., Efstathiou G., Elsner F., Enßlin T. A., Eriksen H. K., Farhang M., Fergusson J., Finelli F., Forni O., Frailis M., Fraisse A. A., Franceschi E., Frejsel A., Galeotta S., Galli S., Ganga K., Gauthier C., Gerbino M., Ghosh T., Giard M., Giraud-Héraud Y., Giusarma E., Gjerlow E., González-Nuevo J., Górski K. M., Gratton S., Gregorio A., Gruppuso A., Gudmundsson J. E., Hamann J., Hansen F. K., Hanson D., Harrison D. L., Helou G., Henrot-Versillé S., Hernández-Monteagudo C., 2015. *Planck 2015 results. XIII. Cosmological parameters.*

- Popesso P., Dickinson M., Nonino M., Vanzella E., Daddi E., Fosbury R. A. E., Kuntschner H., Mainieri V., Cristiani S., Cesarsky C., Giavalisco M., Renzini A., GOODS Team t., 2009. *A&A*, **494**(2), 443. *The great observatories origins deep survey.*
- Ravindranath S., Giavalisco M., Ferguson H. C., Conselice C., Katz N., Weinberg M., Lotz J., Dickinson M., Fall S. M., Mobasher B., Papovich C., 2006. *ApJ*, **652**(2), 963. *The Morphological Diversities among Starforming Galaxies at High Redshifts in the Great Observatories Origins Deep Survey.*
- Razoumov A. O., Sommer-Larsen J., 2010. *ApJ*, **710**(2), 1239. *IONIZING RADIATION FROM $z=4-10$ GALAXIES.*
- Reddy N. A., Steidel C. C., 2009. *ApJ*, **692**(1), 778. *A STEEP FAINT-END SLOPE OF THE UV LUMINOSITY FUNCTION AT $z \sim 2-3$: IMPLICATIONS FOR THE GLOBAL STELLAR MASS DENSITY AND STAR FORMATION IN LOW-MASS HALOS.*
- Reddy N. A., Pettini M., Steidel C. C., Shapley A. E., Erb D. K., Law D. R., 2012. *ApJ*, **754**(1), 25. *The Characteristic Star Formation Histories of Galaxies at Redshifts $z \sim 2-7$.*
- Reines A. E., Nidever D. L., Whelan D. G., Johnson K. E., 2009. *ApJ*, **708**(1), 26. *THE IMPORTANCE OF NEBULAR CONTINUUM AND LINE EMISSION IN OBSERVATIONS OF YOUNG MASSIVE STAR CLUSTERS.*
- Retzlaff J., Rosati P., Dickinson M., Vandame B., Rit   C., Nonino M., Cesarsky C., the GOODS team, 2010. *A&A*, **511**, A50. *The Great Observatories Origins Deep Survey.*
- Rhoads J. E., Malhotra S., Pirzkal N., Dickinson M., Cohen S., Grogin N., Hathi N., Xu C., Ferreras I., Gronwall C., Koekemoer A., K  mmel M., Meurer G., Panagia N., Pasquali A., Ryan R., Straughn A., Walsh J., Windhorst R. A., Yan H.-J., 2009. *ApJ*, **697**(1), 942. *SPECTROSCOPIC CONFIRMATION OF FAINT LYMAN BREAK GALAXIES NEAR REDSHIFT FIVE IN THE HUBBLE ULTRA DEEP FIELD.*
- Robertson B. E., Ellis R. S., Dunlop J. S., McLure R. J., Stark D. P., 2010. *Nature*, **468**(7), 49. *Early star-forming galaxies and the reionization of the Universe.*
- Robertson B. E., Furlanetto S. R., Schneider E., Charlot S., Ellis R. S., Stark D. P., McLure R. J., Dunlop J. S., Koekemoer A., Schenker M. A., Ouchi M., Ono Y., Curtis-Lake E., Rogers A. B., Bowler R. A. A., Cirasuolo M., 2013. *ApJ*, **768**(1), 71. *NEW CONSTRAINTS ON COSMIC REIONIZATION FROM THE 2012 HUBBLE ULTRA DEEP FIELD CAMPAIGN.*
- Robertson B. E., Ellis R. S., Dunlop J. S., McLure R. J., Stark D. P., McLeod D., 2014. *eprint arXiv:1410.0962*. *Accounting for Cosmic Variance in Studies of Gravitationally-Lensed High-Redshift Galaxies in the Hubble Frontier Field Clusters.*

- Robertson B. E., Ellis R. S., Furlanetto S. R., Dunlop J. S., 2015. *eprint arXiv:1502.02024. Cosmic Reionization and Early Star-Forming Galaxies: A Joint Analysis of New Constraints from Planck and Hubble Space Telescope.*
- Rodriguez Espinosa J. M., Gonzalez-Martin O., Castro Rodriguez N., Pérez-González P. G., Mas-Hesse J. M., Munoz-Tunon C., Cava A., Cardiel N., Cabrera Lavers A., Gallego J., Hernan Caballero A., Herrera Ruiz N., Ramirez Olivencia N., 2014. *MNRAS: Letters*, **444**(1), L68. *Episodic star formation in a group of LAEs at $z = 5.07$.*
- Rogers A. B., McLure R. J., Dunlop J. S., Bowler R. A. A., Curtis-Lake E. F., Dayal P., Faber S. M., Ferguson H. C., Finkelstein S. L., Grogin N. A., Hathi N. P., Kocevski D., Koekemoer A. M., Kurczynski P., 2014. *MNRAS*, **440**(4), 3714. *The colour distribution of galaxies at redshift five.*
- Rogers A. B., McLure R. J., Dunlop J. S., 2013. *MNRAS*, **429**(3), 2456. *The unbiased measurement of ultraviolet spectral slopes in low-luminosity galaxies at $z \approx 7$.*
- Rowlands K., Gomez H. L., Dunne L., Aragon-Salamanca A., Dye S., Maddox S., da Cunha E., Werf P. v. d., 2014. *MNRAS*, **441**(2), 1040. *The dust budget crisis in high-redshift submillimetre galaxies.*
- Salmon B., Papovich C., Finkelstein S. L., Tilvi V., Finlator K., Behroozi P., Dahlen T., Davé R., Dekel A., Dickinson M., Ferguson H. C., Giavalisco M., Long J., Lu Y., Reddy N., Somerville R. S., Wechsler R. H., 2014. *eprint arXiv:1407.6012. The Star-Formation Rate and Stellar Mass Relation of Galaxies at $3.5 \leq z \leq 6.5$ in CANDELS.*
- Salpeter E. E., 1955. *ApJ*, **121**, 161. *The Luminosity Function and Stellar Evolution.*
- Sana H., de Mink S. E., de Koter A., Langer N., Evans C. J., Gieles M., Gosset E., Izzard R. G., Le Bouquin J. B., Schneider F. R. N., 2012. *Science*, **337**(6093), 444. *Binary Interaction Dominates the Evolution of Massive Stars.*
- Sana H., de Koter A., de Mink S. E., Dunstall P. R., Evans C. J., Hénault-Brunet V., Maíz Apellániz J., Ramírez-Agudelo O. H., Taylor W. D., Walborn N. R., Clark J. S., Crowther P. A., Herrero A., Gieles M., Langer N., Lennon D. J., Vink J. S., 2013. *A&A*, **550**, A107. *The VLT-FLAMES Tarantula Survey.*
- Santini P., Fontana A., Grazian A., Salimbeni S., Fontanot F., Paris D., Boutsia K., Castellano M., Fiore F., Gallozzi S., Giallongo E., Koekemoer A. M., Menci N., Pentericci L., Somerville R. S., 2012. *A&A*, **538**, A33. *The evolving slope of the stellar mass function at $0.6 < z < 1$.*
- Schaerer D., de Barros S., 2009. *A&A*, **502**(2), 423. *The impact of nebular emission on the ages of $z \approx 6$ galaxies.*
- Schaerer D., de Barros S., 2010. *A&A*, **515**, 73. *On the physical properties of $z \approx 6-8$ galaxies.*
- Schaerer D., de Barros S., Sklias P., 2013. *A&A*, **549**, 4. *Properties of $z \approx 3-6$ Lyman break galaxies. I. Testing star formation histories and the SFR-mass relation with ALMA and near-IR spectroscopy.*

- Schaerer D., Boone F., Zamojski M., Staguhn J., Dessauges-Zavadsky M., Finkelstein S., Combes F., Richard J., 2014. *eprint arXiv:1407.5793. New constraints on dust emission and UV attenuation of z=6.5-7.5 galaxies from IRAM and ALMA observations.*
- Schechter P., 1976. *ApJ*, **203**, 297. *An analytic expression for the luminosity function for galaxies.*
- Schenker M. A., Ellis R. S., Konidaris N. P., Stark D. P., 2013a. *ApJ*, **777**(1), 67. *CONTAMINATION OF BROADBAND PHOTOMETRY BY NEBULAR EMISSION IN HIGH-REDSHIFT GALAXIES: INVESTIGATIONS WITH KECK'S MOSFIRE NEAR-INFRARED SPECTROGRAPH.*
- Schenker M. A., Robertson B. E., Ellis R. S., Ono Y., McLure R. J., Dunlop J. S., Koekemoer A., Bowler R. A. A., Ouchi M., Curtis-Lake E., Rogers A. B., Schneider E., Charlot S., Stark D. P., Furlanetto S. R., Cirasuolo M., 2013b. *ApJ*, **768**(2), 196. *THE UV LUMINOSITY FUNCTION OF STAR-FORMING GALAXIES VIA DROPOUT SELECTION AT REDSHIFTS $z \geq 7$ AND 8 FROM THE 2012 ULTRA DEEP FIELD CAMPAIGN.*
- Schmidt M., 1965. *ApJ*, **141**, 1295. *Large Redshifts of Five Quasi-Stellar Sources.*
- Schmidt M., 1968. *ApJ*, **151**, 394. *Space Distribution and Luminosity Functions of Quasi-Stellar Radio Sources.*
- Shapley A. E., Steidel C. C., Pettini M., Adelberger K. L., Erb D. K., 2006. *ApJ*, **651**(2), 688. *The Direct Detection of Lyman Continuum Emission from Starforming Galaxies at $z \geq 3$.*
- Shapley A. E., Steidel C., Pettini M., 2003. *ApJ. Rest-Frame Ultraviolet Spectra of $z \geq 3$ Lyman Break Galaxies.*
- Shim H., Chary R.-R., Dickinson M., Lin L., Spinrad H., Stern D., Yan C.-H., 2011. *ApJ*, **738**(1), 69. *$z \leq 4$ H α EMITTERS IN THE GREAT OBSERVATORIES ORIGINS DEEP SURVEY: TRACING THE DOMINANT MODE FOR GROWTH OF GALAXIES.*
- Siana B., Teplitz H. I., Colbert J., Ferguson H. C., Dickinson M., Brown T. M., Conselice C. J., de Mello D. F., Gardner J. P., Giavalisco M., Menanteau F., 2007. *ApJ*, **668**(1), 62. *New Constraints on the Lyman Continuum Escape Fraction at $z \geq 1.3$.*
- Siana B., Teplitz H. I., Ferguson H. C., Brown T. M., Giavalisco M., Dickinson M., Chary R.-R., de Mello D. F., Conselice C. J., Bridge C. R., Gardner J. P., Colbert J. W., Scarlata C., 2010. *ApJ*, **723**(1), 241. *A DEEP HUBBLE SPACE TELESCOPE-SEARCH FOR ESCAPING LYMAN CONTINUUM FLUX AT $z \geq 1.3$: EVIDENCE FOR AN EVOLVING IONIZING EMISSIVITY.*
- Smit R., Bouwens R. J., Franx M., Illingworth G. D., Labb   I., Oesch P. A., van Dokkum P. G., 2012. *ApJ*, **756**(1), 14. *THE STAR FORMATION RATE FUNCTION FOR REDSHIFT $z = 4-7$ GALAXIES: EVIDENCE FOR A UNIFORM BUILDUP OF STAR-FORMING GALAXIES DURING THE FIRST 3 Gyr OF COSMIC TIME.*

- Smit R., Bouwens R. J., Labb   I., Zheng W., Bradley L., Donahue M., Lemze D., Moustakas J., Umetsu K., Zitrin A., Coe D., Postman M., Gonz  lez V., Bartelmann M., Benitez N., Broadhurst T., Ford H., Grillo C., Infante L., Jimenez-Teja Y., Jouvel S., Kelson D. D., Lahav O., Maoz D., Medezinski E., Melchior P., Meneghetti M., Merten J., Molino A., Moustakas L. A., Nonino M., Rosati P., Seitz S., 2013. *Evidence for Ubiquitous, High-EW Nebular Emission in z 7 Galaxies: Towards a Clean Measurement of the Specific Star Formation Rate using a Sample of Bright, Magnified Galaxies.*
- Somerville R. S., Hopkins P. F., Cox T. J., Robertson B. E., Hernquist L., 2008. *MNRAS*, **391**(2), 481. *A semi-analytic model for the co-evolution of galaxies, black holes and active galactic nuclei.*
- Somerville R. S., Gilmore R. C., Primack J. R., Dom  nguez A., 2012. *MNRAS*, **423**(3), 1992. *Galaxy properties from the ultraviolet to the far-infrared: A cold dark matter models confront observations.*
- Sommariva V., Mannucci F., Cresci G., Maiolino R., Marconi A., Nagao T., Baroni A., Grazian A., 2012. *A&A*, **539**, 136. *Stellar metallicity of star-forming galaxies at z > 3.*
- Spitler L. R., Straatman C. M. S., Labb   I., Glazebrook K., Tran K.-V. H., Kacprzak G. G., Quadri R. F., Papovich C., Persson S. E., van Dokkum P. G., Allen R., Kawinwanichakij L., Kelson D. D., McCarthy P. J., Mehrtens N., Monson A., Nanayakkara T., Rees G., Tilvi V., Tomczak A. R., 2014. *ApJ*, **787**(2), L36. *EXPLORING THE z= 3-4 MASSIVE GALAXY POPULATION WITH ZFOURGE: THE PREVALENCE OF DUSTY AND QUIESCENT GALAXIES.*
- Stanway E. R., Bunker A. J., McMahon R. G., 2003. *MNRAS*, **342**(2), 439. *Lyman break galaxies and the star formation rate of the Universe at z 6.*
- Stanway E. R., Bunker A. J., McMahon R. G., Ellis R. S., Treu T., McCarthy P. J., 2004a. *ApJ*, **607**(2), 704. *Hubble Space Telescope Imaging and Keck Spectroscopy of z 6 iBand Dropout Galaxies in the Advanced Camera for Surveys GOODS Fields.*
- Stanway E. R., Glazebrook K., Bunker A. J., Abraham R. G., Hook I., Rhoads J., McCarthy P. J., Boyle B., Colless M., Crampton D., Couch W., Jrgensen I., Malhotra S., Murowinski R., Roth K., Savaglio S., Tsvetanov Z., 2004b. *ApJ*, **604**(1), L13. *Three Ly Emitters at z6: Early GMOS/Gemini Data from the GLARE Project.*
- Stark D. P., Bunker A. J., Ellis R. S., Eyles L. P., Lacy M., 2007. *ApJ*, **659**(1), 84. *A New Measurement of the Stellar Mass Density at z5: Implications for the Sources of Cosmic Reionization.*
- Stark D. P., Ellis R. S., Bunker A., Bundy K., Targett T., Benson A., Lacy M., 2009. *ApJ*, **697**(2), 1493. *The Evolutionary History of Lyman Break Galaxies Between Redshift 4 and 6: Observing Successive Generations of Massive Galaxies in Formation.*
- Stark D. P., Schenker M. A., Ellis R., Robertson B., McLure R., Dunlop J., 2013. *ApJ*, **763**(2), 129. *KECK SPECTROSCOPY OF 3 .*

- Stark D. P., Richard J., Siana B., Charlot S., Freeman W. R., Gutkin J., Wofford A., Robertson B., Amanullah R., Watson D., Milvang-Jensen B., 2014a. *MNRAS*, **445(3)**, 3200. *Ultraviolet emission lines in young low-mass galaxies at $z = 2$: physical properties and implications for studies at $z \gtrsim 7$* .
- Stark D. P., Richard J., Charlot S., Clement B., Ellis R., Siana B., Robertson B., Schenker M., Gutkin J., Wofford A., 2014b. *eprint arXiv:1408.3649. Spectroscopic detections of CIII]1909 at $z \approx 6.7$: A new probe of early star forming galaxies and cosmic reionisation.*
- Steidel C. C., Hamilton D., 1992. *Astronomical Journal (ISSN 0004-6256)*, **104**, 941. *Deep imaging of high redshift QSO fields below the Lyman limit. I - The field of Q0000-263 and galaxies at $Z = 3.4$* .
- Steidel C. C., Adelberger K. L., Giavalisco M., Dickinson M., Pettini M., 1999. *ApJ*, **519(1)**, 1. *Lyman-Break Galaxies at $z \approx 4$ and the Evolution of the Ultraviolet Luminosity Density at High Redshift*.
- Strukov I. A., Brukhanov A. A., Skulachev D. P., Sazhin M. V., 1992. *MNRAS*, **258**, 37P. *The Relikt-1 experiment - New results*.
- Teplitz H. I., Rafelski M., Kurczynski P., Bond N. A., Grogin N., Koekemoer A. M., Atek H., Brown T. M., Coe D., Colbert J. W., Ferguson H. C., Finkelstein S. L., Gardner J. P., Gawiser E., Giavalisco M., Gronwall C., Hanish D. J., Lee K.-S., de Mello D. F., Ravindranath S., Ryan R. E., Siana B. D., Scarlata C., Soto E., Voyer E. N., Wolfe A. M., 2013. *The Astronomical Journal*, **146(6)**, 159. *UVUDF: ULTRAVIOLET IMAGING OF THE HUBBLE ULTRA DEEP FIELD WITH WIDE-FIELD CAMERA 3*.
- Thompson R. I., Weymann R. J., Storrie Lombardi L. J., 2001. *ApJ*, **546(2)**, 694. *Star Formation History in the NICMOS Northern Hubble Deep Field*.
- Thompson R. I., 2003. *ApJ*, **596(2)**, 748. *Star Formation History and Other Properties of the Northern Hubble Deep Field*.
- Treu T., Auger M. W., Koopmans L. V. E., Gavazzi R., Marshall P. J., Bolton A. S., 2010. *ApJ*, **709(2)**, 1195. *THE INITIAL MASS FUNCTION OF EARLY-TYPE GALAXIES*.
- Troncoso P., Maiolino R., Sommariva V., Cresci G., Mannucci F., Marconi A., Meneghetti M., Grazian A., Cimatti A., Fontana A., Nagao T., Pentericci L., 2014. *A&A*, **563**, A58. *Metallicity evolution, metallicity gradients, and gas fractions at $z \approx 3.4$* .
- van Dokkum P. G., Conroy C., 2010. *Nature*, **468(7326)**, 940. *A substantial population of low-mass stars in luminous elliptical galaxies*.
- Vanzella E., Cristiani S., Dickinson M., Giavalisco M., Kuntschner H., Haase J., Nonino M., Rosati P., Cesarsky C., Ferguson H. C., Fosbury R. A. E., Grazian A., Moustakas L. A., Rettura A., Popesso P., Renzini A., Stern D., GOODS Team t., 2008. *A&A*, **478(1)**, 83. *The great observatories origins deep survey*.

- Vanzella E., Giavalisco M., Dickinson M., Cristiani S., Nonino M., Kuntschner H., Popesso P., Rosati P., Renzini A., Stern D., Cesarsky C., Ferguson H. C., Fosbury R. A. E., 2009. *ApJ*, **695**(2), 1163. *SPECTROSCOPIC OBSERVATIONS OF LYMAN BREAK GALAXIES AT REDSHIFTS 4, 5, AND 6 IN THE GOODS-SOUTH FIELD.*
- Vanzella E., Siana B., Cristiani S., Nonino M., 2010. *MNRAS*, **404**, 1672. *Contamination on Lyman continuum emission at : implication on the ionizing radiation evolution.*
- Vazquez G. A., Leitherer C., Schaerer D., Meynet G., Maeder A., 2007. *ApJ*, **663**(2), 995. *Models for Massive Stellar Populations with Rotation.*
- Weinmann S. M., Neistein E., Dekel A., 2011. *MNRAS*, **417**(4), 2737. *On the puzzling plateau in the specific star formation rate at $z=2-7$.*
- Wilkins S. M., Bunker A. J., Stanway E., Lorenzoni S., Caruana J., 2011. *MNRAS*, **417**(1), 717. *The ultraviolet properties of star-forming galaxies - I. HST WFC3 observations of very high redshift galaxies.*
- Wilkins S. M., Matteo T. D., Croft R., Khandai N., Feng Y., Bunker A., Coulton W., 2013. *MNRAS*, **429**(3), 2098. *Confronting predictions of the galaxy stellar mass function with observations at high redshift.*
- Willott C. J., Delorme P., Reylé C., Albert L., Bergeron J., Crampton D., Delfosse X., Forveille T., Hutchings J. B., McLure R. J., Omont A., Schade D., 2010. *The Astronomical Journal*, **139**(3), 906. *THE CANADA-FRANCE HIGH- z QUASAR SURVEY: NINE NEW QUASARS AND THE LUMINOSITY FUNCTION AT REDSHIFT 6.*
- Windhorst R. A., Cohen S. H., Hathi N. P., McCarthy P. J., Ryan R. E. J., Yan H., Baldry I. K., Driver S. P., Frogel J. A., Hill D. T., Kelvin L. S., Koekemoer A. M., Mechtley M., O'Connell R. W., Robotham A. S. G., Rutkowski M. J., Seibert M., Straughn A. N., Tuffs R. J., Balick B., Bond H. E., Bushouse H., Calzetti D., Crockett M., Disney M. J., Dopita M. A., Hall D. N. B., Holtzman J. A., Kaviraj S., Kimble R. A., MacKenty J. W., Mutchler M., Paresce F., Saha A., Silk J. I., Trauger J. T., Walker A. R., Whitmore B. C., Young E. T., 2011. *ApJS*, **193**(2), 27. *The Hubble Space Telescope Wide Field Camera 3 Early Release Science Data: Panchromatic Faint Object Counts for 0.2-2 μ m Wavelength.*
- Wise J. H., Cen R., 2009. *ApJ*, **693**(1), 984. *IONIZING PHOTON ESCAPE FRACTIONS FROM HIGH-REDSHIFT DWARF GALAXIES.*
- Wise J. H., Demchenko V. G., Halicek M. T., Norman M. L., Turk M. J., Abel T., Smith B. D., 2014. *MNRAS*, **442**(3), 2560. *The birth of a galaxy - III. Propelling reionization with the faintest galaxies.*
- Wuyts S., van Dokkum P. G., Franx M., Schreiber N. M. F., Illingworth G. D., Labbé I., Rudnick G., 2009. *ApJ*, **706**(1), 885. *OPTICAL SPECTROSCOPY OF DISTANT RED GALAXIES.*
- Yajima H., Choi J.-H., Nagamine K., 2010. *MNRAS*, **412**(1), 411. *Escape fraction of ionizing photons from high-redshift galaxies in cosmological SPH simulations.*

- Yan H., Finkelstein S. L., Huang K.-H., Ryan R. E., Ferguson H. C., Koekemoer A. M., Grogin N. A., Dickinson M., Newman J. A., Somerville R. S., Davé R., Faber S. M., Papovich C., Guo Y., Giavalisco M., Lee K.-S., Reddy N., Cooray A. R., Siana B. D., Hathi N. P., Fazio G. G., Ashby M., Weiner B. J., Lucas R. A., Dekel A., Pentericci L., Conselice C. J., Kocevski D. D., Lai K., 2012. *ApJ*, **761(2)**, 177. *LUMINOUS AND HIGH STELLAR MASS CANDIDATE GALAXIES AT $z \approx 8$ DISCOVERED IN THE COSMIC ASSEMBLY NEAR-INFRARED DEEP EXTRAGALACTIC LEGACY SURVEY.*
- Zackrisson E., Inoue A. K., Jensen H., 2013. *ApJ*, **777(1)**, 39. *THE SPECTRAL EVOLUTION OF THE FIRST GALAXIES. II. SPECTRAL SIGNATURES OF LYMAN CONTINUUM LEAKAGE FROM GALAXIES IN THE REIONIZATION EPOCH.*
- Zafar T., Watson D., 2013. *A&A*, **560**, A26. *The metals-to-dust ratio to very low metallicities using GRB and QSO absorbers; extremely rapid dust formation.*
- Zastrow J., Oey M. S., Veilleux S., McDonald M., 2013. *ApJ*, **779(1)**, 76. *NEW CONSTRAINTS ON THE ESCAPE OF IONIZING PHOTONS FROM STARBURST GALAXIES USING IONIZATION-PARAMETER MAPPING.*
- Zheng W., Postman M., Zitrin A., Moustakas J., Shu X., Jouvel S., Host O., Molino A., Bradley L., Coe D., Moustakas L. A., Carrasco M., Ford H., Benítez N., Lauer T. R., Seitz S., Bouwens R. J., Koekemoer A., Medezinski E., Bartelmann M., Broadhurst T., Donahue M., Grillo C., Infante L., Jha S. W., Kelson D. D., Lahav O., Lemze D., Melchior P., Meneghetti M., Merten J., Nonino M., Ogaz S., Rosati P., Umetsu K., van der Wel A., 2012. *Nature*, **489(7416)**, 406. *A magnified young galaxy from about 500 million years after the Big Bang.*